The Pennsylvania State University

The Graduate School

Department of Chemistry

# SURFACE FUNCTIONALIZATION OF OXIDES FOR BIOSENSING APPLICATIONS

A Dissertation in

Chemistry

by

Kristi Lynn Liddell



Submitted in Partial Fulfillment
of the Requirements
for the Degree of

Doctor of Philosophy

May 2014

The dissertation of Kristi L. Liddell was reviewed and approved* by the following:

Christine D. Keating
Professor of Chemistry
Dissertation Advisor
Chair of Committee

Thomas E. Mallouk
Evan Pugh Professor of Materials Chemistry and Physics
Associate Head of the Chemistry Department
Professor of Chemistry
Professor of Biochemistry and Molecular Biology

Mary Elizabeth Williams
Associate Dean for Undergraduate Education, Eberly College of Science
Professor of Chemistry

Jun Zhu
Associate Professor of Physics

Barbara J. Garrison
Head of the Department of Chemistry
Shapiro Professor of Chemistry

*Signatures are on file in the Graduate School

# ABSTRACT

Functionalization of oxide materials plays a critical role in the development of electronic-based biosensors, such as field effect transistors (FETs). A dielectric coating (insulator) on the electrically-active surfaces isolates electronic components from the sensing medium and serves as the immobilization surface for bioreceptors. This dissertation examined several strategies to functionalize the standard gate dielectric, $SiO_2$, and emerging high-*k* materials, $Al_2O_3$ and $HfO_2$. As such, understanding functionalization on alumina and hafnium oxide is of interest as this has been extensively studied on silica but is less understood with other materials.

In Chapter 2, current silane chemistries were verified on $SiO_2$ and compared with $Al_2O_3$ and $HfO_2$ surfaces using microarray technology. Spots of probe DNA were printed onto a planar surface with success seen by comparable mean spot fluorescence intensity between all surfaces. Furthermore, characterization of new surface chemistries involving phosphonic acids on $Al_2O_3$ was performed with contact angle, x-ray photoelectron spectroscopy, and infrared spectroscopy. A bioassay demonstrated excellent selectivity for complementary DNA target hybridization using a phosphonic acid linker (3-aminopropylphosphonic acid, APPA) on $Al_2O_3$ tiles.

In Chapters 3 and 4, demonstration of functionalized $SiO_2$ surfaces is shown with graphene and silicon nanowire FETs, respectively. A novel oxide-on-graphene biosensor was fabricated with a graphene channel passivated with a $SiO_2/HfO_2$ (25 nm/20 nm) double oxide layer, which used the top $SiO_2$ layer as the sensing/immobilization surface and the high-quality $HfO_2$ layer to protect the channel from solution. Demonstration of

pH sensitivity from 4-9 was shown with bare and 3-aminopropyltrimethoxysilane (APTMS)-functionalized devices. Device response is also shown upon functionalization with APTMS and biotin linker with solutions of protein analyte, avidin. Top-down Si NW FETs with $SiO_2$ gate dielectric were also fabricated and are discussed in Chapter 4. Bare and APTMS-functionalized device response to changes in solution pH is shown. A complex mechanism of detection was found for real-time, label-free measurements of analyte solutions containing protein and DNA.

Methods to regenerate biosensor (or oxide) surfaces are discussed in Chapter 5. Model $SiO_2$ surfaces were functionalized with APTMS and probe DNA, followed by DNA target hybridization. Mild reaction conditions, necessary to preserve biosensor performance, were explored to remove target from the surface, either by cleavage of the probe chemistry or using a chaotropic reagent, urea.

Biosensor technology has evolved tremendously in recent years to enable devices that are sensitive, selective, portable, and easy to use. The introduction of new materials and surface modifications into modern electronics will enable diversification in an already exciting field.

# TABLE OF CONTENTS

# LIST OF FIGURES

# LIST OF TABLES

# LIST OF ABBREVIATIONS

| | |
|---|---|
| Al | Aluminum |
| ALD | Atomic Layer Deposition |
| APTMS | 3-aminopropyltrimethoxysilane |
| Au | Gold |
| AuNP | Gold Nanoparticle |
| BioFET | Biological Field Effect Transistor |
| BSA | Bovine Serum Albumin |
| CHES | N-cyclohexyl-2-aminoethanesulfonic acid |
| CMOS | Complementary Metal Oxide Semiconductor |
| COMP | Complementary |
| DI $H_2O$ | 18.2 MΩ:cm Nanopure Water |
| DNA | Deoxyribonucleic Acid |
| DTT | Dithiothreitol |
| EtOH | Ethanol |
| FESEM | Field Emission Scanning Electron Microscopy |
| FET | Field Effect Transistor |
| FTIR | Fourier Transform Infrared Spectroscopy |
| GFET | Graphene Field Effect Transistor |
| GO | Graphene Oxide |
| GF | Graphene Fluoride |

| | |
|---|---|
| $H_2O_2$ | Hydrogen peroxide |
| HMDS | Hexamethyldisilazane |
| $I_{DS}$ | Drain-Source Current |
| ISFET | Ion Sensitive Field Effect Transistor |
| ITRS | International Technology Roadmap for Semiconductors |
| KCl | Potassium chloride |
| LOD | Limit of Detection |
| MIS | Metal-Insulator-Semiconductor |
| MOSFET | Metal-Oxide-Semiconductor Field Effect Transistor |
| $N_2$ | Nitrogen |
| NaCl | Sodium Chloride |
| NaOH | Sodium Hydroxide |
| NC | Non-Complementary |
| $NH_4OH$ | Ammonium Hydroxide |
| NHS-SS-Biotin | Succinimidyl 2-(biotinamido)-ethyl-1,3'dithiopropionate |
| NW | Nanowire |
| PBS | Phosphate Buffered Saline |
| PDMS | Polydimethylsiloxane |
| pI | Isoelectric Point |
| PNA | Peptide Nucleic Acid |
| Pt | Platinum |
| PTFE | Polytetrafluoroethylene |

| | |
|---|---|
| QRE | Quasi-Reference Electrode |
| SA | Streptavidin |
| SEM | Scanning Electron Microscopy |
| Si | Silicon |
| SOI | Silicon-On-Insulator |
| ss-DNA | Single Stranded DNA |
| Sulfo-LC-SPDP | Sulfosuccinimidyl 6-(3'-[2-pyridyldithio]-propionamido)-hexanoate |
| Sulfo-SMCC | Sulfosuccinimidyl-4-(*N*-maleimidomethyl)cyclohexane-1-carboxylate |
| TEM | Transmission Electron Microscopy |
| TEOS | Tetraethoxysilane |
| Ti | Titanium |
| $T_m$ | Melting Temperature |
| UV | Ultra Violet |
| UV-Vis | Ultra Violet-Visible |
| $V_{sg}$ | Solution Gate Potential |
| XPS | X-Ray Photoelectron Spectroscopy |

# ACKNOWLEDGEMENTS

I would like to extend my gratitude to my thesis advisor, Dr. Christine Keating, for her encouragement and guidance during my time at Penn State. She fostered professional growth without expense of work/life balance. I thank my thesis committee; Dr. Mary Beth Williams, Dr. Tom Mallouk, and Dr. Jun Zhu, for their support and help with this thesis.

Much of this work was done in collaboration with others on campus. I would like to thank Xiahua Zhong and Dr. Bei Wang and their respective advisors, Dr. Theresa Mayer and Dr. Jun Zhu, for their work and thoughtful contributions on device fabrication and characterization. Several user facilities on campus were vital to the collection of data for this thesis. I extend my appreciation to those involved with the maintenance and operation of deposition, lithography, etching, and characterization tools in the MSC Nanofabrication Laboratory. Dr. Joshua Stapleton and Dr. Vince Bojan from the Materials Characterization Laboratory were helpful in IR and XPS data collection and interpretation. Dr. Craig Praul in the Genomics Core Facility was helpful with microarray experiments and related discussions.

Many Keating group members have been of great help to me throughout my graduate career for professional guidance and friendship. A “crew” of my favorite people will always be appreciated for their friendship and support. We’ve listened and vented

our frustrations and accomplishments of science and life along this journey; something I hope will continue in the future.

My appreciation and love for my family runs deep. Their encouragement and support have motivated me to accomplish whatever I set in my mind. This thesis is a nod to the hard work and countless hours they have spent on me. Thank-you.

My husband Chris is my rock, best friend, and confidant. Words cannot express my gratitude for his unwavering support throughout my educational endeavors. I am lucky to have had him by my side for 12 years. Our next journey awaits us and we will explore it together, like always.

# Chapter 1

## Introduction

The semiconductor industry has traditionally placed a major emphasis on increasing the processing power of electronics by increasing the number of transistors on a chip while scaling down its size (a trend known as Moore's law[1]).[2] However, introducing new materials, such as biomolecules, has fueled a different focus for sensing applications. Combining field effect transistor (FET) biosensors with powerful microchip computing will produce a device that has the advantages of high sensitivity, multiplexing capability, small sample volume, ease of use, and portability. This thesis is focused on understanding the surface functionalization of high-*k* dielectrics for use with FETs, like $Al_2O_3$ and $HfO_2$, as this has been extensively studied on $SiO_2$ but limited information is available with other materials. In addition, the relationship between binding events at the semiconductor surface and a conductance change was explored.

The introduction provides background information on the use of oxides as insulators in modern electronics. The material properties of several oxides discussed in this dissertation are compared. Methods and instrumentation used to characterize oxide functionalization is presented. The design and operation of field effect transistors (FETs) will be discussed in addition to the mechanism of charged biomolecule detection. Furthermore, the implications of measurements in electrolyte on the Debye length will be covered.

## 1.1 Insulators in Modern Electronics

Transistors are ubiquitous in the modern era as they operate like a switch to control the flow of electrons, i.e. electrical power.[3] The most important design, from which many chemical sensors are based, is the metal-oxide-semiconductor field effect transistor (MOSFET). A representative device structure is shown in Figure 1-1, which includes a semiconductor channel between source and drain electrodes, gate dielectric, and metal gate. The metal gate functions as a switch by modulating the channel conductance based on an applied potential ($V_g$). The gate dielectric is a dielectric (insulator) material, typically an oxide, which prevents the flow of electrons between the channel and metal gate.[3]

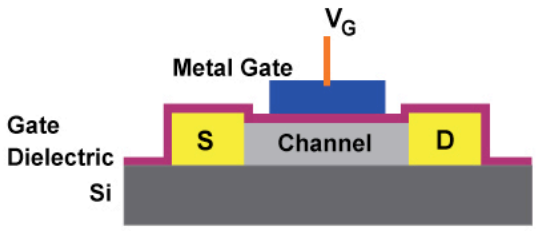


**Figure 1-1** Structure of metal oxide semiconductor field effect transistor (MOSFET).

Modification of this design, including the replacement of the metal gate with a solution and the attachment of molecular receptors to the gate dielectric, enabled new options for chemical and biological sensors. The popularity of such designs can seen by the explosive growth in the last decade due to their use in a wide variety of fields including medical diagnostics and environmental analysis.[4,5] As the focus of this dissertation is to explore methods to functionalize different oxides and demonstrate their use with FETs, it is helpful to first understand the fundamental properties of oxide materials.

### 1.2 Fundamental Material Properties of Oxides

Solid materials are classified into three main categories based on their electrical conductivity. From highest electrical conductivity to lowest, these categories are: metals, semiconductors, and insulators (Figure 1-2). An energy gap, called the band gap ($E_g$), is present between the valence (VB) and conduction (CB) bands in semiconductors and insulators. In semiconductors, this gap is relatively small, and excited electrons can move into the conduction band, albeit less easily than in metals. Insulators are distinguished by a larger band gap, typically > 3 eV, which prevents electrical conduction.[6] The oxides discussed in this dissertation have a large band gap that poorly conducts electricity and are thus used as insulators in electronic devices. Comparison of material properties is useful to understand the benefits and limitations of each oxide.

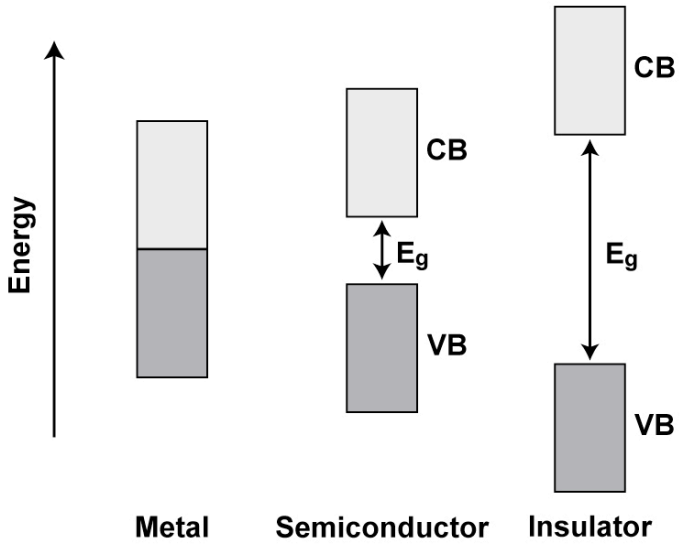


**Figure 1-2** Cartoon of energy band diagram for metals, semiconductors, and insulators where the filled bands shown by the dark grey region represent the valence band (VB) and empty bands in light grey represent the conduction band (CB). The space designated $E_g$ between the valence and conduction band in semiconductors and insulators is the band gap energy.

$SiO_2$ has been the most common oxide material used in the semiconductor industry. It has a tetrahedral geometry with four oxygen atoms singly bonded to Si. The strength of the Si-O covalent bond means double bonds between Si and O are rare; thus, oxygen atoms form bridges between two Si atoms to satisfy their valences.[7] A wide band gap of 9 eV indicates $SiO_2$ is a good insulator between the gate and semiconducting channel.[8,9] This property is important because it prevents current leakage between the gate and channel. A major drawback to this material is its relatively low dielectric constant ($k$) of 2.9. As modern electronics have scaled to smaller dimensions, the $SiO_2$ dielectric has been made thinner. There is a limit to scaling where a material no longer maintains its bulk properties. For $SiO_2$, thin films less than 10 nm begin to degrade in performance.[10,11]

Materials with a high dielectric constant and large band gap are desired for future electronics. Alumina ($Al_2O_3$) and hafnia ($HfO_2$) are such materials that are being explored. A high-$k$, 9 and 25, and large band gap, 8.8 eV and 5.8 eV for $Al_2O_3$ and $HfO_2$, respectively, make these materials good gate dielectric candidates.[8] However, both materials can exist in several different phases, crystalline or amorphous, which can greatly affect structural and electronic properties. Deposition processes used in electronic devices typically result in amorphous phases and for this reason have been investigated extensively.[12-14] Amorphous $Al_2O_3$ forms strong, ionic Al-O bonds with several different O-Al-O bond angles. Thus, central Al atoms in an oxidation state of +3 can form tetrahedral or octahedral networks with O atoms.[7,12] Hafnium exhibits a monoclinic phase structure at ambient pressure and temperatures.[15] It has a +4 oxidation state and forms strong, ionic bonds between Hf and O atoms.[7]

The properties of surfaces are modeled by discrete surface sites. In the case of $SiO_2$, $Al_2O_3$, and $HfO_2$, this is represented by M-OH where M represents Si, Al, or Hf. Given the amphoteric character of these oxides, three forms can exist on a surface: $M\text{-}O^-$, M-OH, and $M\text{-}OH_2^+$.[16] The pH at which the oxide exhibits a net neutral charge is called the point of zero charge, denoted by $pH_{pzc}$. Thus, when the pH of a solution is below the oxide $pH_{pzc}$, the surface has a net positive charge, and conversely, a net positive charge is observed in solutions with a pH above the $pH_{pzc}$. This parameter is important because it can impact the stability, adhesion, and adsorption properties of a surface. The $pH_{pzc}$ for $SiO_2$ and $Al_2O_3$ can vary based on different phases and preparations, but average values are ~ 2 and ~ 8, respectively[16-18], with $HfO_2$ exhibiting a $pH_{pzc}$ of ~ 7[19].

Due to fabrication and post-fabrication steps, the chemistry and crystal structure of gate dielectrics can differ greatly from the expected stoichiometry and structural properties.[14] Despite the associated significant impact on electronic properties, this was not a great concern from the standpoint of an immobilization surface for two reasons: First, atomic layer deposition (ALD) was used to fabricate the metal oxide films, which were not expected to differ between batches.[20] Second, oxide surfaces were usually treated with oxygen plasma prior to surface functionalization to populate the surface with terminal hydroxyl groups for subsequent biomolecule attachment.[21]

### 1.3 Preparation, Functionalization, and Characterization of Oxide Materials

For this thesis, surface chemistry was studied off-chip on substrates coated with the oxide of interest. During the development stages of Si NW FET design and fabrication, a very limited number of devices were available to study surface chemistry due to high

fabrication cost and time and low yield. Since the gate dielectric is the only material that comes in contact with the solution, it was beneficial to deposit that material on test substrates; thus, bare Si wafers without electronic devices were used to optimize reaction conditions. An additional benefit of off-chip optimization allowed smaller reaction volumes, which was cost effective and enabled higher throughput.

### 1.3.1 Fabrication of Oxide Materials

Metal oxide surfaces used in this thesis were prepared by atomic layer deposition (ALD). Atomic layer deposition (ALD) has become an important technique to fabricate high quality, thin film coatings of metal oxides. ALD offers the advantage of precise thickness control across the entire reaction surface, even in trenches or pores, due to the 2 step, self-limiting surface chemistry reaction as shown in Figure 1-3.[20] In the first step, precursor "A", typically an organometallic compound reacts with all available surface sites. The system is purged with a non-reactive gas, like nitrogen, then precursor "B" reacts with "A" to form an atomic layer of material. The system is purged and the process is repeated until the desired thickness is reached. This technique was used to fabricate thin films of $Al_2O_3$ and $HfO_2$ using trimethylaluminum and tetrakis(dimethylamido)hafnium, respectively, as the primary precursor and water as the second.

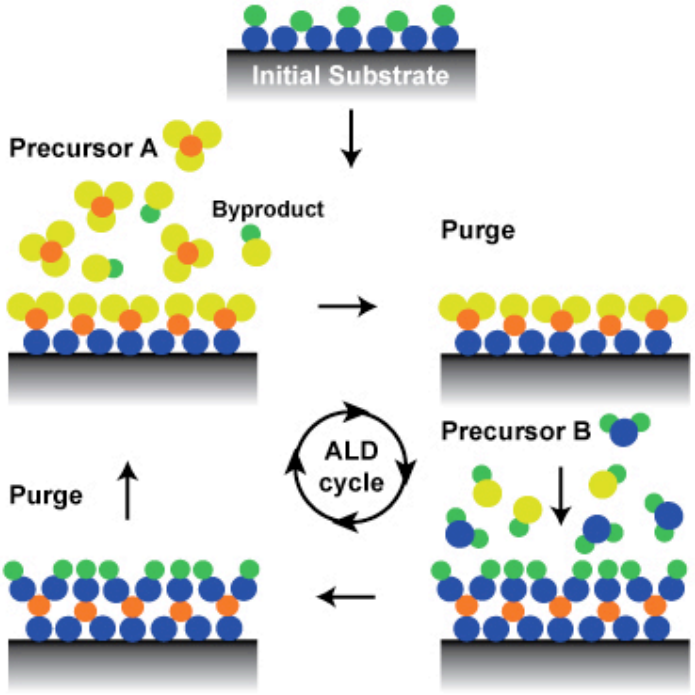


**Figure 1-3** Cartoon of reaction process with an atomic layer deposition (ALD) tool involving precursors "A" and "B" between chamber purge steps that allow the fabrication of thin film metal oxides. Adapted from Ref 20.

### 1.3.2 Functionalization of Oxide Materials

Functionalization of the gate dielectric with crosslinker chemistries enables a variety of probe molecules to be covalently attached to the oxide surface for detection of proteins[22-24], nucleic acids[25-27], or viruses[28,29] (Figure 1-4).

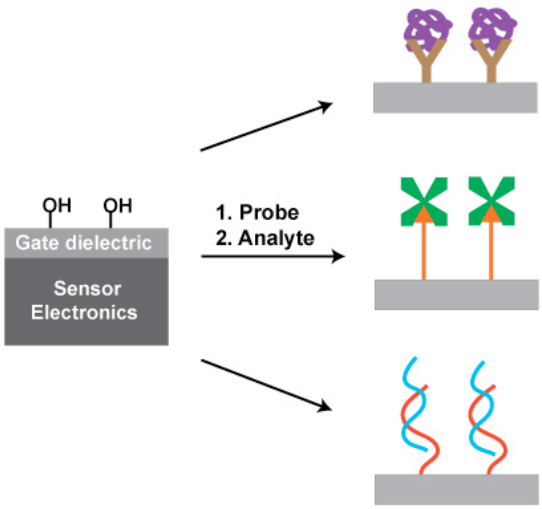


**Figure 1-4** Cartoon of gate dielectric (oxide) on sensor electronics that enables covalent functionalization of bioprobes to the surface and capture of target analyte such as viruses, proteins, or single-stranded DNA.

Much work has been done to optimize attachment strategies with silica ($SiO_2$), as it is the most common gate dielectric. Organosilanes with terminal amine or aldehyde groups are the most popular route to modify $SiO_2$ surfaces.[30,31] A wide selection of crosslinking chemistries is commercially available for subsequent reactions based on the chemical specificity of the desired probe, spacer arm length, water-solubility, or cleavability.[32,33] Less information is available about surface functionalization of alternative oxide materials such as $Al_2O_3$ or $HfO_2$.

### 1.3.3 Characterization of Oxide Materials

The initial reaction between oxide and linker was the primary focus due to its impact on the success of maintaining receptor molecules covalently attached to the surface. Several analytical techniques were used in this thesis to characterize the surface

functionalization of oxide materials. Upon verification of linker covalent attachment, optimal reaction conditions were developed, and additional linkers were adhered for biomolecule detection. An overview of the techniques used is described below.

Contact angle- Contact angle (CA) is perhaps the easiest method to characterize the wetting property of surfaces, which can report on surface functionalization if the bare surface has different wettability as compared to the chemically functionalized surface. Wetting describes the shape of a liquid droplet on a solid surface, which changes in response to the horizontal components of interfacial tension or surface tension, γ, acting on it.[34] At equilibrium the resulting angle, θ, formed between the solid/vapor, solid/liquid, and liquid/vapor interfaces, is referred to as the contact angle. Young's equation (Equation 1-1) describes the interfacial tension, γ, of each interface in relation to the contact angle, θ.

$$\gamma_{SV} = \gamma_{SL} + \gamma_{LV} \cos\theta \qquad \text{Equation 1-1}$$

A static CA measurement is obtained by producing a drop of water onto a solid surface and capturing a two-dimensional profile image. In general, surfaces are considered hydrophobic when the contact angle exceeds 90° and hydrophilic at angles less than 90° (Figure 1-5). Upon functionalization, the interfacial tension of the solid surface will change based on the polarity of the attached molecules. This technique provided a rapid, initial evaluation of surface functionalization success/failure and was useful to establish reaction conditions.

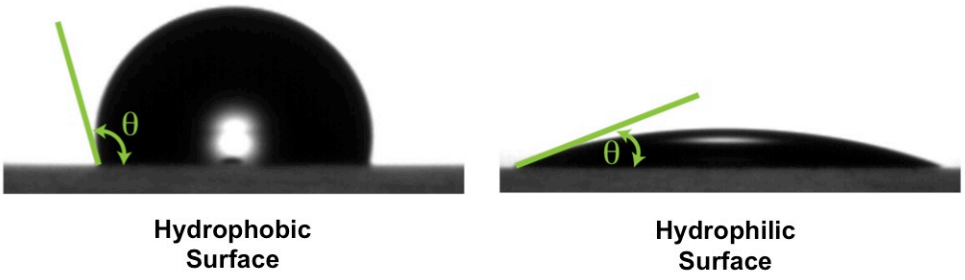


**Figure 1-5** Representative static contact angle measurements obtained from hydrophobic or hydrophilic surfaces.

X-ray photoelectron spectroscopy- X-ray photoelectron spectroscopy (XPS) can report on the chemical composition of a sample surface. It was used in this work to verify the presence of linker chemistries after each step of functionalization. When an X-ray beam of known energy, $h\nu$, ejects a core electron from a surface, that electron with kinetic energy ($E_K$) is collected and analyzed by a detector. Since all core level electrons have well-defined binding energies ($E_{BE}$), elemental identification can be accomplished given Equation 1-2 and work function ($\phi$) of the spectrometer.[35] A general schematic of operation is presented in Figure 1-6.[36]

$$E_{BE} = h\nu - (E_K + \phi) \qquad \text{Equation 1-2}$$

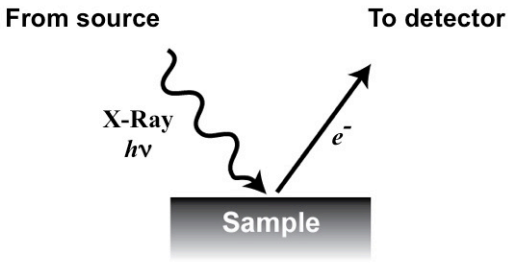


**Figure 1-6** General scheme of the XPS measurement. The incident beam is typically from Al Kα X-ray photons, core electrons ($e^-$) are ejected from the surface, and analyzed by a detector.

XPS is useful for studying surface functionalization because it clearly demonstrates changes in surface composition as different linkers and probe molecules are covalently attached. In some instances, it can also be used to determine chemical structure and oxidation states.[36]

Infrared spectroscopy- Most analytical techniques used to characterize the functionalized surfaces of oxides provide evidence that functional groups or atoms of interest are present, but the nature of attachment (covalent versus physisorption) is unclear. As infrared spectroscopy (IR) probes the vibrational transitions of molecular bonds in a sample, it is possible to gain information about how molecules attach to the surface. There are several bonding modes proposed for organophosphonates bound to metal oxide surfaces (Figure 1-7).[37]

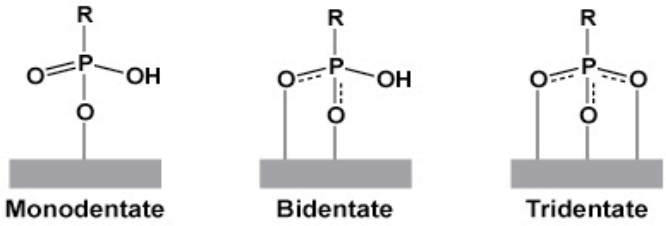


**Figure 1-7** Proposed bonding modes of organophosphonates on metal oxides.

Wood and coworkers used IR to study self-assembled monolayer formation of alkyl phosphonic acids with carbon chain lengths of 16 or 22 ($H_{16}PA$ or $H_{22}PA$, respectively) on aluminum metal.[38] In the C-H stretching region, ordering of the methylene chains was observed to an "all-trans" orientation normal to the aluminum surface and the low-frequency region had broad features characteristic of phosphonate binding to Al. In particular, symetric and assymetric R-$PO_3^{2-}$ stretches were identified. These observations along with a loss of OH from the Al native oxide surface support a condensation reaction to form bidentate and/or tridentate bonds between the phosphonate and metal surface.[38] IR measurements were used in Chapter 2 to verify covalent attachment of phosphonates on $Al_2O_3$-coated surfaces.

Optical microscopy- Optical microscopy is a powerful analytical tool traditionally used in bioassays. Incubation of fluorescent target with known probe receptors immobilized to a solid support enables highly sensitive and selective detection of analyte.[39] Validation of $SiO_2$ surface chemistry was performed using direct hybridization of fluorescently-labeled DNA target on glass-coated metal nanowires using reflectance

and fluorescence microscopy.[40] A schematic of the method and representative images obtained are shown in Figure 1-8.

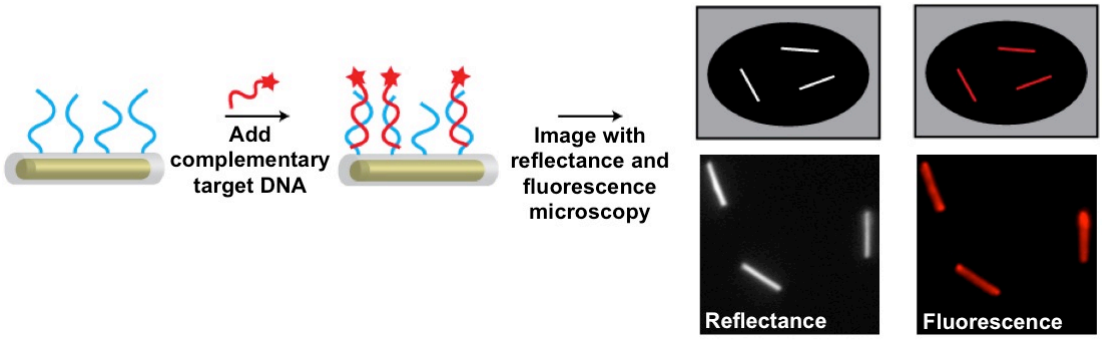


**Figure 1-8** Schematic of fluorescently-labeled DNA target binding to DNA probe immobilized on $SiO_2$-coated metal nanowires and subsequent images obtained using reflectance and fluorescence microscopy. The lower pictures are representative microscopy images.

For planar substrates, quantification of DNA hybridization was accomplished using a DNA microarray protocol. DNA microarrays became popular in the 1990's for the purpose of studying gene expression. A large (≥30,000) collection of probes can be immobilized on a solid support at specific locations. After incubation in fluorescent target, hybridized sequences can be detected with a fluorescence scanner (Figure 1-9).[41]

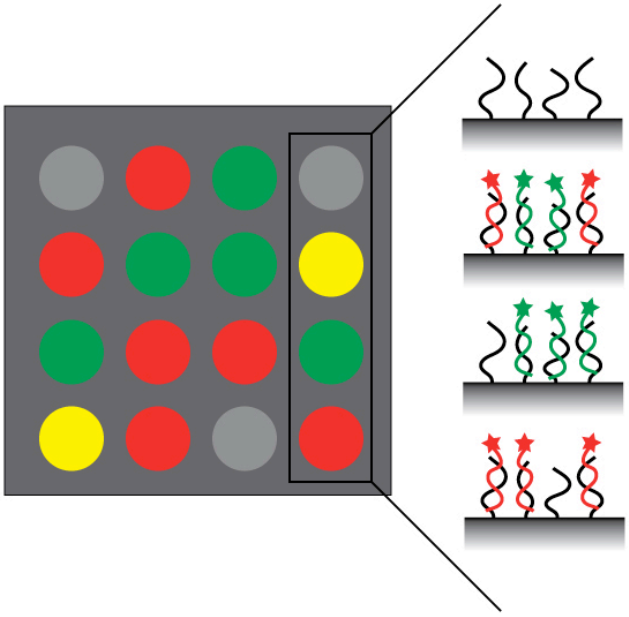

**Figure 1-9** Cartoon of DNA microarray demonstrates fluorescent target hybridizes to immobilized DNA to yield colored spots signifying no target (grey), two different targets (yellow), or a singular target (green, red) hybridized to the probe.

Due to the high throughput capability and automated fluorescence detection using slide scanners and software detection, this technique was utilized in Chapter 2 to study different linker chemistries on a several oxide materials ($SiO_2$, $Al_2O_3$, and $HfO_2$). This process complemented optical microscopy experiments with $SiO_2$-coated metal nanowires, by enabling comparison of data from $SiO_2$, $Al_2O_3$, and $HfO_2$ -coated planar surfaces.

### 1.4 FETs as Chemical and Biological Sensors

Traditional chemical and biological sensors have a similar design compared to planar MOSFETs, which was an attractive sensor platform, as the binding event of a charged analyte resulted in a change in channel conductance by a mechanism similar to applying a

potential to a metal gate (Figure 1-10). This potential resulted in accumulation (Figure 1-10, B) or depletion (Figure 1-10, C) of charge carriers in the semiconducting channel and a change in conductance (Figure 1-10; D, E).[3] As early as 1991, research was directed toward miniaturized configurations when greater sensitivity was observed with high aspect ratio structures.[42] This improved device sensitivity is achieved with nanoscale FETs due to a high ratio of surface to bulk atoms, which causes a larger change in channel conductance upon target binding.[43,44] Shrinking the sensor to nanoscale dimensions also enables dense device arrays and greater multiplex capabilities.[4]

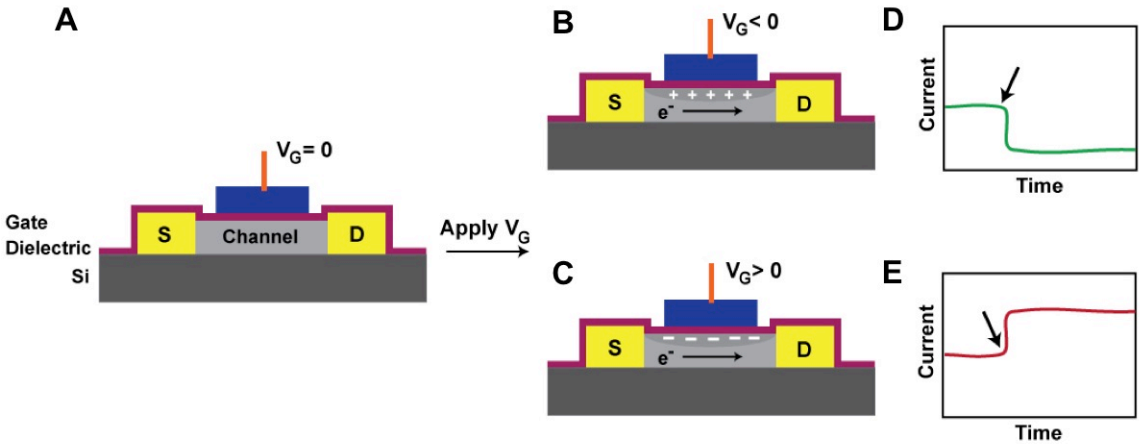


**Figure 1-10** (A) Cartoon of a MOSFET with a n-type semiconducting channel spanned between source (S) and drain (D) electrodes. A thin gate dielectric insulates the metal gate from the channel. Applying a gate potential ($V_G$) causes (B) accumulation or (C) depletion of charge carriers. Representative graph of current versus time shows change in conductance upon applying (arrow) a negative (D) or positive (E) $V_G$.

### 1.4.1 Graphene FETs

In recent years graphene-based materials have gained interest for use in FETs as they have very high carrier mobility and excellent electronic properties. Fabrication of

graphene films was first described in 2004 by mechanical exfoliation of highly oriented pyrolytic graphite.[45] Despite ease of production and low cost, this technique suffers from low yield; instead, chemical vapor deposition (CVD) has become a popular alternative due to its high quality and high yield preparation.[46]

Use of graphene, in its natural state, is unsuitable in FETs as it lacks an intrinsic band gap; thus, the channel conductance cannot be switched to an off state of minimum drain current.[46] Consequently, chemical derivatives of graphene, such as graphene oxide (GO) or graphene fluoride (GF) have been synthesized to open a band gap that enables modulation of channel conductance. In comparison to pristine graphene, which is composed of a honeycomb lattice of $sp^2$-bonded carbon atoms (Figure 1-11, A), GO has a network of $sp^2$ and $sp^3$-bonded carbon atoms where a high fraction of $sp^3$-carbon atoms are bonded to oxygen in the form of carboxyl, hydroxyl, or epoxy groups[47,48] (Figure 1-11, B), and GF contains stacked layers of fluorinated graphite that has $sp^3$-bonded carbon atoms covalently bonded to fluorine atoms[49] (Figure 1-11, C).

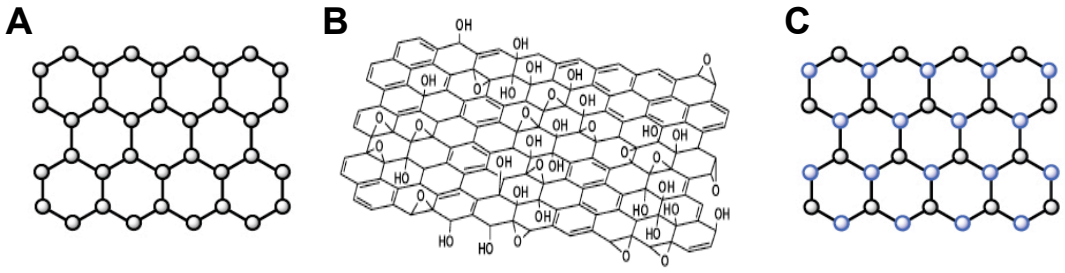


**Figure 1-11** Structure of (A) pristine graphene[46], (B) graphene oxide[48], (C) graphene fluoride[49]. Black and blue spheres represent carbon and fluorine atoms, respectively.

Fluorinated derivatives of graphene exhibit high stability, mechanical strength, and stiffness due to strong bonds between carbon and fluorine.[45] Partially and fully fluorinated graphene has been found to be excellent insulators with a large band gap of ~ 3 eV[46,49]. In Chapter 3, we took advantage of these properties to fabricate graphene FETs.

### 1.4.2 Si NW FETs

Silicon nanowires (NWs) are a popular channel material due to their electronic properties, high-yield preparation, and high carrier mobility.[50] Two types of impurities, called dopants, can be intentionally added to alter the conductivity of Si based on if they are electron donors (n-type) or electron acceptors (p-type). In the Si crystal lattice, Si atoms bind to four other Si atoms to satisfy four outer valence electrons. Replacement of a Si atom with phosphorus, which has five outer valence electrons, results in an unbound, extra electron (Figure 1-12, A). This electron can readily ionize and move to the conduction band easily. Conversely, substitution of a Si atom with boron, with only three outer valence electrons, results in a vacancy or hole due to an unfilled bond between nearest neighbor atoms (Figure 1-12, B). The vacancy left behind can propagate as electrons jump from one occupied state to another (Figure 1-12, B). A decrease in band gap is observed for either dopant, which leads to only a small energy required to promote conduction.[3]

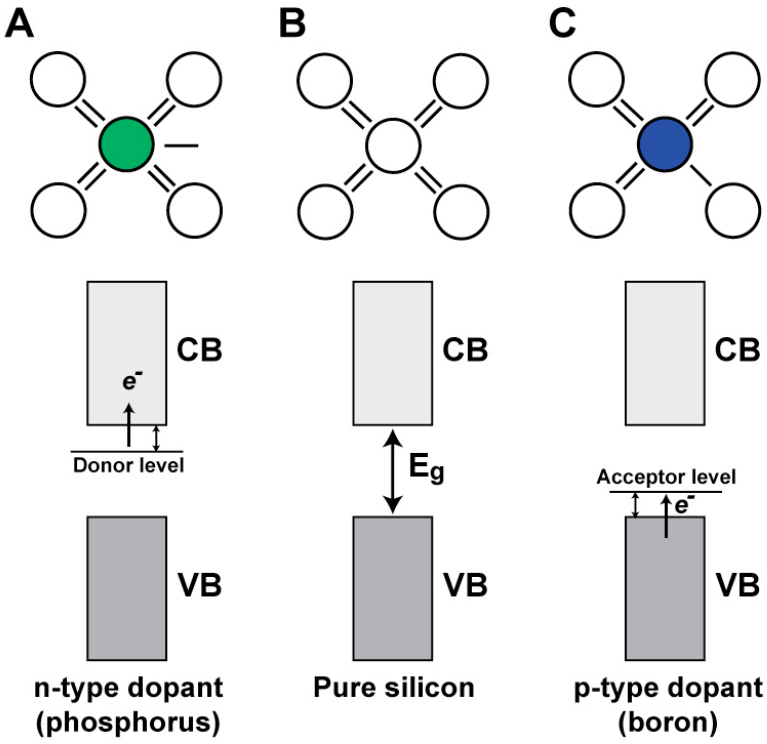


**Figure 1-12** Two-dimensional representation of the Si crystal lattice and respective energy band diagram for (A) phosphorus-doped Si, (B) pure Si, and (B) boron-doped Si. For the crystal lattice, empty circles represent Si atoms where green or blue filled circles represent donor atom phosphorus or acceptor atom boron, respectively. The conduction band and valance band are labeled CB and VB, respectively and the band gap, $E_g$, is designated by the double arrow. Adapted from Ref 3.

Two general schemes, bottom-up or top-down, have been employed to fabricate Si NW FET arrays based on the method of Si NW incorporation. As implied, bottom-up fabrication of devices involves placement of Si NW onto a substrate and electronic components built up around them. Top-down strategies use photolithography and etching steps to shape desired features out of the substrate.

Currently, top-down fabrication has shown the most promise, as it results in large arrays of nearly identical Si NWs aligned at predetermined locations.[44] This method simplifies device integration, although it is associated with longer and higher costs of

production. However, a great concern that has been largely unaddressed[51,52] is the variability in device performance despite large arrays of "uniform" wires. Haick and co-workers suggest current methods to evaluate device properties (e.g. nanowire size, shape, doping) do not guarantee uniform or adequate electrical performance.[53]

### 1.5 Implications of Solution-Based FET Measurements

Detection of target using FETs is dependent upon changes in channel current induced by the capture of charged target molecules near the semiconductor surface. For solution-based measurements, a solution potential is applied through an electrode ($V_{app}$) to control the flow of electrons through a semiconducting channel. Figure 1-13 depicts a solution-based measurement using peptide nucleic acid (PNA) probe molecules as receptors for single-stranded DNA.

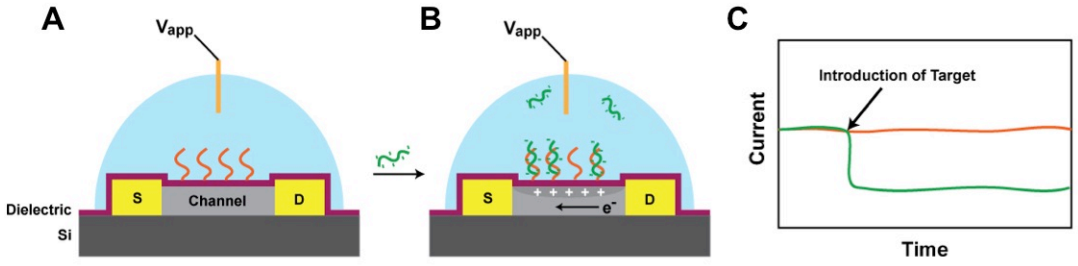


**Figure 1-13** (A) Field-effect transistor has an n-type semiconducting channel spanned between source (S) and drain (D) electrodes. For solution-based measurements, the gate potential is controlled by an electrode placed in the solution ($V_{app}$). A thin dielectric protects the device electronics from the aqueous medium above and is used to immobilize probe PNA molecules. (B) Representative graph of current versus time begins with measurement in buffer and upon capture of negatively charged DNA near the semiconductor surface a decrease in current is observed (green). An additional trace for a device measuring a solution of buffer only is also displayed (orange) for comparison purposes.

The solution ionic strength or the presence of counterions in solution plays a vital role in detection sensitivity. Given that the ionic strength is determined by the molar concentration of ions present ($C_i$), and their charges ($Z_i$), counterions can screen the charge of analytes of interest, preventing analyte detection (Equation 1-3).

$$I = \frac{1}{2}\sum_{i=1}^{n} C_i Z_i^2 \qquad \text{Equation 1-3}$$

This phenomenon is well known and has been modeled by several groups[54,55] and demonstrated experimentally as well[23,26]. For example, Reed and coworkers have shown that a decrease in ionic strength by dilution of measurement buffer (standard phosphate buffered saline, 1 X PBS) affected detection sensitivity of a negatively-charged protein, streptavidin.[23] A Si NW FET was biotinylated, and then incubated with streptavidin (Figure 1-14, A). A graph of device current with time showed the effect of changing the ionic strength of buffer used during measurements (Figure 1-14, B). At a buffer concentration of 0.01 X, very little screening of negative charges from streptavidin resulted in a large signal change with respect to a buffer concentration of 1 X, where little to no charge from streptavidin was observed.

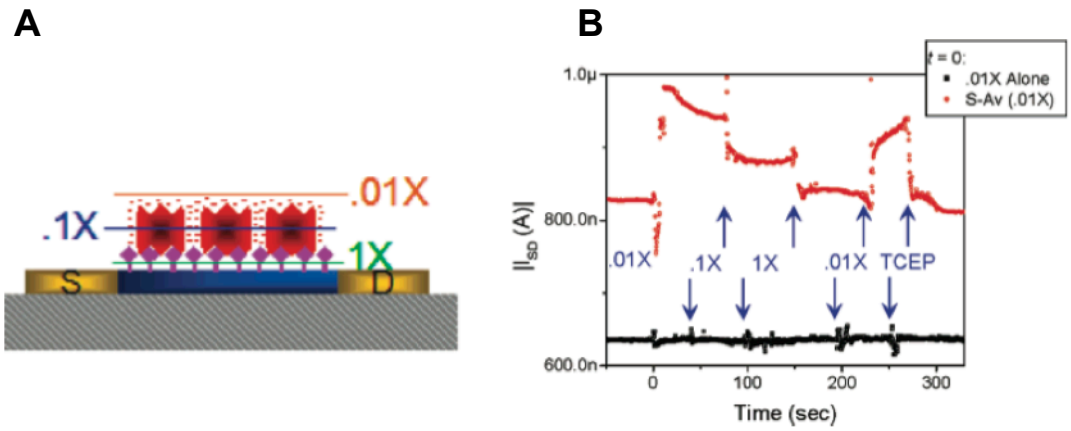


**Figure 1-14** (A) Cartoon of Si NW FET functionalized with biotin (purple) and streptavidin (red). Lines indicate approximate screening length with respect to the device surface in 1 X (green), 0.1 X (blue), or 0.01 X (orange) buffer. (B) Graph of current versus time shows response after solution changes in different ionic strength buffer from a device with (red) or without (black) streptavidin. Arrows indicate onset of solution exchange. Adapted with permission from Ref 23. Copyright 2014 American Chemical Society.

This experiment exemplified the importance of charge-screening in FET sensors. The degree of screening, known as Debye length ($\kappa^{-1}$), is based on the solution ionic strength (I), permittivity of free space ($\varepsilon_o$), dielectric constant ($\varepsilon_r$), Boltzmann constant ($k_B$), temperature (T), Avogadro's number ($N_A$), and elementary charge ($e$) (Equation 1-4).

$$\kappa^{-1} = \sqrt{\frac{\varepsilon_0 \varepsilon_r k_B T}{2 N_A e^2 I}} \qquad \text{Equation 1-4}$$

Careful consideration of the Debye length and thus ionic strength is necessary to ensure optimal detection given measurement conditions. Given the graph of Debye length versus KCl concentration in Figure 1-15, it may seem reasonable to always err on the side of caution and use low-buffered solutions or water.

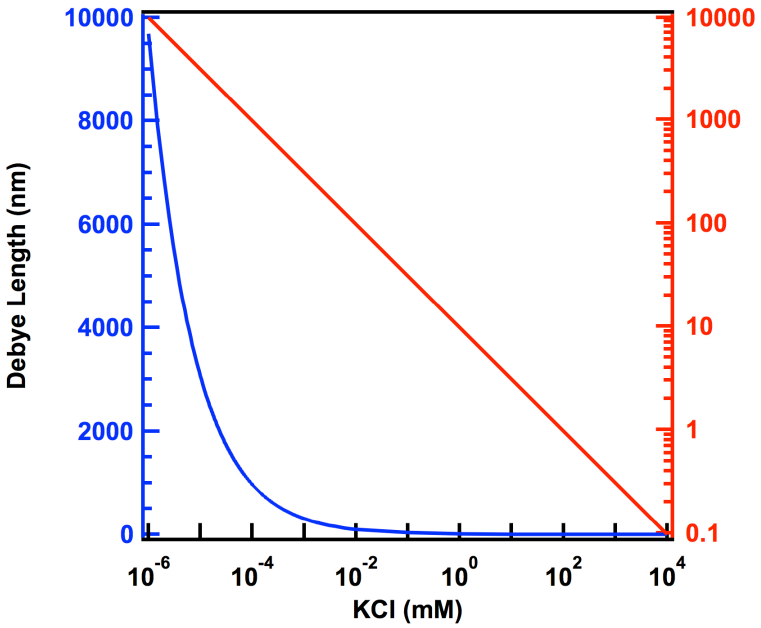


**Figure 1-15** Graph of Debye length versus concentration of KCl.

However, under these conditions many biomolecules, such as DNA or some proteins, do not retain their structure or lose their ability to selectively bind target analyte.[56,57] For example, a comparison of duplex stability, as demonstrated by melting temperatures ($T_m$) for 10 base oligos of DNA and PNA (peptide nucleic acid), shows under low salt conditions, DNA-DNA duplexes are not readily stable at room temperature, whereas PNA-PNA duplex stability is unaffected (Table 1-1). At 0 M and 0.05 M NaCl, DNA-PNA duplex formation exhibits high stability, but with high salt a small decrease is observed.[58]

**Table 1-1:** Comparison of $T_m$ (°C) resulting from duplex formation of 10 base DNA and PNA sequences[a,b] in buffer[c] with different concentrations of added NaCl.[58]

| | Duplex $T_m$ (°C) with added NaCl (M) | | |
|---|---|---|---|
| | 0.00 | 0.05 | 0.5 |
| DNA−DNA | 19.5 | 31.0 | 43.0 |
| PNA−PNA | 66.1 | 65.4 | 64.3 |
| DNA−PNA | 52.1 | 51.0 | 44.7 |

[a] DNA sequence: 5'-AGTGATCTAC-3'
[b] PNA sequence: N-GTAGATCACT-C
[c] Buffer: 10 mM sodium phosphate at pH 7.0

For biosensing experiments in this thesis, a moderate buffer ionic strength of ~0.1 mM, which corresponded to a Debye length of ~30 nm, was typically used. This concentration was chosen based on the maximum length of biomolecules if stretched in a straight line from the surface and the effect of ionic strength on DNA duplex formation. To minimize electrostatic repulsion between probe and target duplexes, a neutral DNA analog, peptide nucleic acid (PNA), was often used as the immobilized probe. In comparison to DNA which has one negative charge along the phosphate backbone for every nucleotide, PNA is composed of uncharged repeating N-(2-aminoethyl)-glycine units linked by peptide bonds (Figure 1-16).[59] Furthermore, it has been reported that incoming DNA strands are easier to detect with PNA probe functionalized Si NW FETs due to its neutral background.[60]

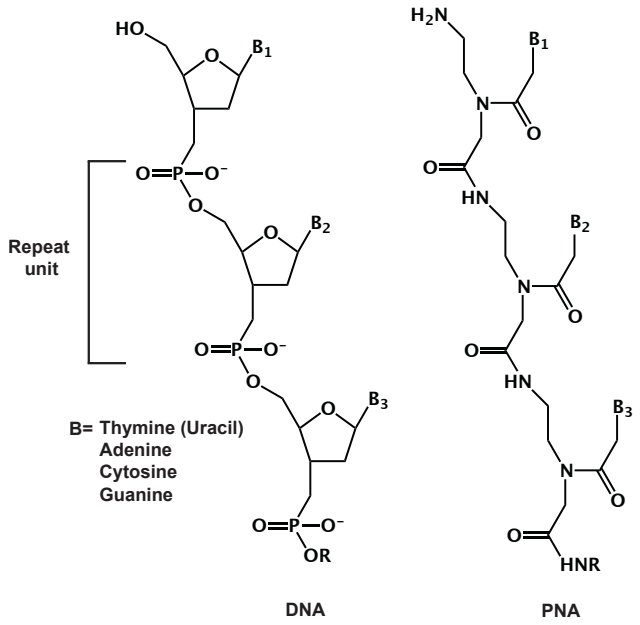


**Figure 1-16** Backbone structure of deoxyribonucleic acid (DNA) and peptide nucleic acid (PNA).

Selection of optimal solution composition is crucial for sensitive and specific detection of analyte, but is useless if analyte never reaches the sensor surface. Therefore, the method of analyte solution delivery must be considered. One of two routes is typically employed for solution-based FET detection of biomolecules: macro mixing cell or microfluidic channel. The goal of either strategy is to introduce convection and minimize efforts from analyte diffusion alone.[61] The macro mixing cell is a simpler approach, where a sample holder typically made of silicone or acrylic is adhered to the surface of the chip. Static or continuous flow can be delivered to the chip through an opening at the top.[23,62] This method is amenable to most device configurations and is fast and easy to fabricate. Alternatively, microfluidic channels are popular to deliver analyte solutions to the biosensor and are amenable to lab-on-a-chip applications.[26,28] Typically fabricated

from PDMS (polydimethylsiloxane), these channels enable lower sample volumes and reduce environmental complications like airflow and temperature compared to a mixing cell. However, obstacles remain such as a need for specialized skill and equipment to fabricate and surface modifications are often necessary to reduce non-specific adsorption of analyte.[63] Solution flow, whether static or continuous, is required for either delivery method during measurements to provide changes in buffer or addition of analyte. A linear change in conductance has been observed with flow velocity of electrolytic solutions[64]; thus, solution delivery remains another contribution to analysis and optimization of FET sensing.

A reference electrode is useful in electrical measurements to maintain a constant gate potential; however, most designs are too large for microscale biosensors. Miniaturized versions have been developed, such as solid-state Ag/AgCl, by eliminating their liquid junction component.[65] These have been called "quasi" reference electrodes (QRE) because they are in direct contact with measurement solution instead of an internal filling solution, but this can lead to undesired effects such as unstable potential and short lifetimes.[65,66] For these reasons, inclusion of miniaturized reference electrodes in biosensor measurements has been avoided (with unexplored consequences) in several biosensing publications.[27,60,67]

### 1.6 Thesis Objectives

This dissertation examines functionalization of oxide surfaces and their use in electrical-based biosensors. Biosensor technology has evolved tremendously in recent years to enable devices that are now highly sensitive, selective, portable, and easy to use.

To demonstrate their commercial capabilities, new materials and surface chemistries are needed to optimize device performance. Chapter 2 describes methods for oxide surface functionalization that were validated without electrical devices using optical/fluorescence microscopy, contact angle measurements (CA), X-ray photoelectron spectroscopy (XPS), infrared spectroscopy (IR), and planar microarrays. Chapters 3 and 4 describe field-effect transistor (FET) biosensors using graphene or silicon nanowires (NWs) that were fabricated and characterized for their electronic and biosensing properties in collaboration with Dr. Jun Zhu's group in Physics or Dr. Theresa Mayer's group in Electrical Engineering, respectively, from Pennsylvania State University. Chapter 5 examines the removal of biomolecules from oxide surfaces as a method to regenerate devices for repeated measurements. Finally, a general chemistry laboratory experiment where students synthesized silver nanoparticles and examined size-dependent properties is shown.

## 1.7 References

1. Moore, G. E. Cramming More Components onto Integrated Circuits. *Electronics* **1965,** *38*, 114-117.

2. International Technology Roadmap for Semiconductors 2010 Update. *Internal Technology Roadmap for Semiconductors*, **2010.**3. Brennan, K. F. *Introduction to Semiconductor Devices for Computing and Telecommunications Applications*, Cambridge University Press: Cambridge, 2005.

3. Brennan, K. F. *Introduction to Semiconductor Devices for Computing and Telecommunications Applications*, Cambridge University Press: Cambridge, 2005.

4. Patolsky, F.; Zheng, G.; Lieber, C. M. Nanowire Sensors for Medicine and the Life Sciences. *Nanomedicine* **2006**, *1*, 51-65.

5. Rodgers, K. R. Recent Advances in Biosensor Techniques for Environmental Monitoring. *Anal. Chim. Acta*. **2006**, *568*, 222-231.

6. *Chemistry The Central Science*; Brown T. L.; LeMay, H. E.; Bursten, B. E.; Murphy, C. J.; Woodward, P., Eds.; Pearson Education: Upper Saddle River, NJ, 2009, p 481-488.

7. House, J. E.; House, K. A. *Descriptive Inorganic Chemistry*, 2nd Edition; Elsevier: New York, 2010.

8. Robertson, J. High Dielectric Constant Gate Oxides for Metal Oxide Si. *Rep. Prog. Phys.* **2006**, *69*, 327-396.

9. Houssa, M. *High-K Gate Dielectrics*; IOP Publishing: Philadelphia, PA, 2004.

10. *Materials Fundamentals of Gate Dielectrics*; Demkov, A. A., Navrotsky, A., Eds.; Springer: Netherlands, 2005.

11. Nikolaides, M. G.; Rauschenbach, S.; Luber, S.; Buchholtz, K.; Tornow, M.; Abstreiter, C.; Bausch, A. R. Silicon-On-Insulator Based Thin-Film Resistor for Chemical and Biological Sensor Applications. *Chemphyschem* **2003**, *4*, 1104-1106.

12. Manaila, R.; Dévényi, A.; Candet, E. Structural Order in Amorphous Aluminas. *Thin Solid Films* **1984**, *116*, 289-299.

13. Chang, H.; Choi, H.; Kong, K.; R, B.-H. Atomic and Electronic Structures of Amorphous $Al_2O_3$. *Chem. Phys. Lett.* **2004**, *391*, 293-296.

14. Cheynet, M. C.; Pokrant, S.; Tichelaar, F. D.; Rouvière, J.-L. Crystal Structure and Band Gap Determination of $HfO_2$ Thin Films. *J. Appl. Phys.* **2007**, *101*, 054101.

15. Zhao, X.; Vanderbuilt, D. First-Principles Study of Structural, Vibrational, and Lattice Dielectric Properties of Hafnium Oxide. *Phys. Rev. B.* **2002**, *65*, 233106.

16. Bousse, L.; De Rooij, N. F.; Bergveld, P. Operation of Chemically Sensitive Field-Effect Sensors As a Function of the Insulator-Electrolyte Interface, *IEEE Trans. Electron. Dev.* **1983**, *30*, 1263-1270.

17. Kosmulski, M. The pH-Dependent Surface Charging and Points of Zero Charge V. Update, *J. Coll. Interf. Sci.* **2011**, *353*, 1-15.

18. Chen, S.; Bomer, J. G.; Carlen, E. T.; Berg, A. V. D. Al2O3/Silicon NanoISFET with Near Ideal Nernstian Response. *Nano Lett.* **2011**, *11*, 2334-2341.

19. Kosmulski, M. Attempt To Determine Pristine Points of Zero Charge of $Nb_2O_5$, $Ta_2O_5$, and $HfO_2$. *Langmuir* **1997**, *13*, 6315-6320.

20. George, S. M. Atomic Layer Deposition: An Overview, *Chem. Rev.* **2010**, *110*, 111-131.

21. Siow, K. S.; Britcher, L.; Kumar, S.; Griesser, H. J. Plasma Methods for the Generation of Chemically Reactive Surfaces for Biomolecule Immobilization and Cell Colonization-A Review, *Plasma Process. Polym.* **2006**, *3*, 392-418.

22. Zheng, G.; Patolksky, F.; Cui, Y.; Wang, W.; Lieber, C. Multiplexed Electrical Detection of Cancer Markers with Nanowire Sensor Arrays. *Nat. Biotech.* **2005**, *23*, 1294-1301.

23. Stern, E.; Wagner, R.; Sigworth, F.; Breaker, R.; Fahmy, T.; Reed, M. Importance of the Debye Screening Length on Nanowire Field Effect Transistor Sensors. *Nano Lett.* **2007**, *7*, 3405-3409.

24. Tian, R.; Regonda, S.; Gao, J.; Liu, Y.; Hu, W. Ultrasensitive Protein Detection using Lithographically Defined Si Multi-Nanowire Field Effect Transistors. *Lab on a Chip* **2011,** *11*, 1952-1961.

25. Li, Z.; Chen, Y.; Li, X.; Kamins, T.; Nauka, K.; Williams, R. Sequence-Specific Label-Free DNA Sensors Based on Silicon Nanowires. *Nano Lett.* **2004,** *4,* 245-247.

26. Bunimovich, Y.; Shin, Y.; Yeo, W.-S.; Amori, M.; Kwong, G.; Heath, J. Quantitative Real-Time Measurements of DNA Hybridization with Alkylated Nonoxidized Silicon Nanowires in Electrolyte Solution. *J. Am. Chem. Soc.* **2006,** *128*, 16323-16331.

27. Gao, A.; Lu, N.; Dai, P.; Li, T.; Pei, H.; Gao, X.; Gong, Y.; Wang, Y.; Fan, C. Silicon-Nanowire-Based CMOS-Compatible Field-Effect Transistor Nanosensors for Ultrasensitive Electrical Detection of Nucleic Acids. *Nano Lett.* **2011,** *11*, 3974-3978.

28. Patolsky, F.; Zheng, G.; Hayden, O.; Lakadamyali, M.; Zhuang, X.; Lieber, C. Electrical Detection of Single Viruses. *Proc. Nat. Acad. Sci.* **2004,** *101,* 14017-14022.

29. Bhattacharya, M.; Hong, S.; Lee, D.; Cui, T.; Goyal, S. Carbon Nanotube Based Sensors for the Detection of Viruses. *Sens. Actu. B: Chem.* **2011,** *155*, 67-74.

30. Hofer, R.; Textor, M.; Spencer, N. D. "Alkyl phosphate monolayers, self-assembled from aqueous solution on metal oxide surfaces," *Langmuir*, **2001**, *17*, 4014-4020.

31. Pellerite, M. J.; Wood, E. J.; Jones, V. W. Dynamic Contact Angle Studies of Self-Assembled Thin Films from Fluorinated Alkyltrichlorosilanes. *J. Phys. Chem. B.* **2002**, *106*, 4746-4754.

32. *Bioconjugate Techniques*; Hermanson, G. T. 2nd Ed. Elsevier: London, 2008; pp 506-515.

33. Crosslinking Reagents. http://www.piercenet.com/cat/crosslinking-reagents (accessed Feb 2, 2014).

34. Barnes, G.; Gentle, I. *Interfacial Science an Introduction*, Oxford University Press: New York, 2005.

35. Chung, Y.-W. *Practical Guide to Surface Science and Spectoscopy.* Academic Press: New York, 2001.

36. *Principles of Instrumental Analysis*; Skoog, D. A.; Holler, F. J.; Nieman, T. A., Eds.; Thomson: USA, 1998.

37. Mutin, P.; Guerrero, G.; Vioux, A. Hybrid Materials from Organophosphorus Coupling Molecules. *J. Mater. Chem.* **2005,** *15*, 3761-3768.

38. Pellerite, M. J.; Dunbar, T. D.; Boardman, L. D.; Wood, E. J. Effects of Fluorination on Self-Assembled Monolayer Formation from Alkanephosphonic Acids on Aluminum: Kinetics and Structure. *J. Phys. Chem. B.* **2003**, *107*, 11726-11736.

39. Lazcka, O.; Campo, F. J. D.; Muñoz, F. X. Pathogen Detection: A Perspective of Traditional Methods and Biosensors. *Biosens. Bioelec.* **2007**, *22*, 1205-1217.

40. Sioss, J. A.; Stoermer, R. L.; Sha, M. Y.; Keating, C. D. Silica-Coated, Au/Ag Striped Nanowires for Bioanalysis. *Langmuir* **2007**, *23*, 11334-11341.

41. Schena, M.; Shalon, D.; Davis, R. W.; Brown, P. O. Quantitative Monitoring of Gene Expression Patterns with a Complementary DNA Microarray. *Science* **1995**, *270*, 467-470.

42. Yamazoe, N. New Approaches for Improving Semiconductor Gas Sensors. *Sens. Actu. B.* **1991**, *5*, 7-19.

43. Cui, Y.; Wei, Q.; Park, H.; Lieber, C. M. Nanowire Nanosensors for Highly Sensitive and Selective Detection of Biological and Chemical Species. *Science* **2001**, *293*, 1289-1292.

44. Curreli, M.; Zhang, R.; Ishikawa, F. N.; Chang, H.-K.; Cote, R. J.; Zhou, C.; Thompson, M. E. Real-Time, Label-Free Detection of Biological Entities Using Nanowire-Based FETs. *IEEE Trans. Nanotech.* **2008**, *7*, 651-666.

45. Novoselov, K. S.; Geim, A. K.; Morozov, S. V.; Zhang, Y.; Dubonos, S. V.; Grigorieva, I. V.; Firsov, A. A. Electric Field Effect in Atomically Thin Carbon Films. *Science* **2004**, *306*, 666-669.

46. Warner, J. H.; Schaffel, F.; Bachmatiuk, A.; Rummeli, M. H. *Graphene: Fundamentals and Emergent Applications*; Elsevier: Waltham, MA, 2013.

47. Mkhoyan, K. A.; Contryman, A. W.; Silcox, J.; Stewart, D. A.; Eda, G.; Mattevi, C.; Miller, S.; Chhowalla, M. Atomic and Electronic Structure of Graphene-Oxide. *Nano Lett.* **2009**, *9*, 1058-1063.

48. Dreyer, D. R.; Park, S.; Bielawski, C. W.; Ruoff, R. S. The Chemistry of Graphene Oxide. *Chem. Soc. Rev.* **2010**, *39*, 228.

49. Robinson, J. T.; Burgess, J. S.; Junkermeier, C. E.; Badescu, S. C.; Reinecke, T. L.; Perkins, F. K.; Zalautdniov, M. K.; Baldwin, J. W.; Culbertson, J. C.; Sheehan, P. E.; Snow, E. S. Properties of Fluorinated Graphene Films. *Nano Lett.* **2010**, *10*, 3001-3005.

50. Lu, W.; Xie, P.; Lieber, C. Nanowire Transistor Performance Limits and Applications. *IEEE Trans. Electron. Dev.* **2008**, *55*, 2859-2876.

51. Makowski, M. S.; Ivanisevic, A. Molecular Analysis of Blood with Micro-/Nanoscale Field-Effect-Transistor Biosensors. *Small* **2011**, *7*, 1863-1875.

52. Vacic, A.; Reed, M. A. Quantitative Nanoscale Field Effect Sensors. *J. Exp. Nanosci.* **2014**, *9*, 41-50.

53. Wang, B.; Stelzner, T.; Dirawi, R.; Assad, O.; Shehada, N.; Christiansen, S.; Haick. H. Field-Effect Transistors Based on Silicon Nanowire Arrays: Effect of the Good and the Bad Silicon Nanowires. *ACS Appl. Mater. Interf.* **2012**, *4*, 4251-4258.

54. Landheer, D.; Aers, G.; McKinnon, W. R.; Deen, M. J.; Ranuarez, J. C. Model for the Field Effect from Layers of Biological Macromolecules on the Gates of Metal-Oxide-Semiconductor Transistors. *J. Appl. Phys.* **2005**, *98*, 044701.

55. Shinwari, M. W.; Deen, M. J. Important Physical Processes to Consider when Modeling the Response of DNA Biotransistors. *Sens. Actu. B.* **2012**, *171-172*, 463-468.

56. Nair, P. R.; Alam, M. A.; Design Considerations of Silicon Nanowire Biosensors. *IEEE Trans. Electron. Dev.* **2007**, *54*, 3400-3408.

57. Lloret, N.; Frederiksen, R. S.; Møller, T. C.; Rieben, N. I.; Upadhyay, S.; Vico, L. D.; Jensen, J. H.; Nygård, J.; Martinez, K. L. Effects of Buffer Composition and Dilution on Nanowire Field-Effect Biosensors. *Nanotechnology* **2013**, *24*, 035501.

58. Tomac, S.; Sarkar, M.; Ratilainen, T.; Wittung, P.; Nielsen, P. E.; Nordén, B.; Gräslund, S. Ionic Effects on the Stability and Conformation of Peptide Nucleic Acid Complexes. *J. Amer. Chem. Soc.* **1996**, *118*, 5544-5552.

59. Wang, J.; Palecek, E.; Nielsen, P. E.; Rivas, G.; Cai, X.; Shiraishi, H.; Dontha, N.; Luo, D.; Farias, P. A. M. Peptide Nucleic Acid Probes for Sequence-Specific DNA Biosensors. *J. Amer. Chem. Soc.* **1996**, *188*, 7667-7670.

60. Gao, Z.; Agarwal, A.; Trigg, A. D.; Singh, N.; Fang, C.; Tung, C. H.; Fan, Y.; Buddharaju, K. D.; Kong, J. Silicon Nanowire Arrays for Label-Free Detection of DNA. *Anal. Chem*. **2007**, *79*, 3291–3297.

61. Squires, T. M.; Messinger, R. J.; Manalis, S. R. Making it Stick: Convection, Reaction, and Diffusion in Surface-Based Biosensors. *Nat. Biotech.* **2008**, *26*, 417-426.

62. Zhang, G-J.; Chua, J. H.; Chee, R-E.; Agarway, A.; Wong, S. M.; Buddharaju, K. D.; Balasubramanian, N. Highly Sensitive Measurements of PNA-DNA Hybridization Using Oxide-Etched Silicon Nanowire Biosensors. *Biosens. Bioelectron.* **2008**, *23*, 1701-1707.

63. Zhou, J.; Khodakov, D. A.; Ellis, A. V.; Voelcker, N. H. Surface Modifications for PDMS-Based Microfluidic Devices. *Electrophoresis* **2012**, *33*, 89-104.

64. Kim, D. R.; Lee, C. H.; Zheng, X. Probing Flow Velocity with Silicon Nanowire Sensors. *Nano Lett*. **2009**, *9*, 1984-1988.

65. Shinwari, M. W.; Zhitomirsky, D.; Deen, I. A.; Selvaganapathy, P. R.; Deen, M. J.; Landheer, D. Microfabricated Reference Electrodes and their Biosensing Applications. *Sensors* **2010**, *10*, 1679-1715.

66. Rim, T.; Kim, K.; Hong, M.; Ko, W.; Baek, C-K.; Jeon, S.; Deen, M. J.; Meyyappan, M.; Jeong, Y-H.; Lee, J-S. Investigation of the Electrical Stability of Si-Nanowire Biologically Sensitive Field-Effect Transistors with Embedded Ag/AgCl Pseudo Reference Electrode. *RSC Adv.* **2013**, *3*, 7963-7969.

67. Kim, D.-S.; Jeong, Y.-T.; Lyu, H.-K.; Park, H.-J.; Kim, H. S.; Shin, J.-K.; Choi, P.; Lee, J.-H.; Lim, G.; Ishida, M. Fabrication and Characteristics of a Field Effect Transistor-Type Charge Sensor for Detecting Deoxyribonucleic Acid Sequence. *Jpn. J. Appl. Phys.* **2003**, *42*, 4111-4115.

# Chapter 2

## Surface Functionalization Investigations of $SiO_2$ and $Al_2O_3$ with Amino-Terminal Silanes and Phosphonic Acids

The author of this dissertation was responsible for all the work presented within this chapter. Dr. Stacey Dean preformed seminal experiments on AuNP adsorption studies with $SiO_2$, $Al_2O_3$, and $HfO_2$ surfaces functionalized with APTMS. Summer undergraduate student, Pedro Rivera Pomales, examined applicable solvents to dissolve phosphonic acid molecules and demonstrated surface functionalization on $SiO_2$ and $Al_2O_3$ surfaces using static constant angle measurements.

### 2.1 Introduction

Surface modification with self-assembled monolayers (SAMs) onto $SiO_2$, $Al_2O_3$, $HfO_2$, and other metal oxides is critical for a wide variety of applications including biosensors, molecular electronics, and separations.[1-3] SAMs with terminal-group functionality are used with field effect transistor (FET) biosensors to covalently attach receptors to the gate oxide, which also serves an insulative barrier between the semiconducting channel and the measurement solution.[4] This attachment chemistry is critical because binding of a charged analyte (as the case with DNA, proteins, or viruses) near the semiconducting surface modulates the channel conductance. Thus, FETs provide a method for direct and label-free electrical readout for the detection analyte in solution.[5,6]

For successful detection of biomolecules, the dual role of the gate dielectric as an electronic insulator and immobilization surface, must be considered. Traditionally, $SiO_2$ has been employed as the gate dielectric due to excellent insulator qualities, ease of fabrication, and well-established siloxane chemistry.[7,8] Specifically, $SiO_2$ has a large

band gap of 9 eV, can withstand high temperature processes, forms an excellent interface with Si (the most common FET channel material), can be conveniently deposited or thermally grown on the surface, and reaction with organosilanes enables stable covalent attachment of receptor molecules.[4,7-9] However, upon device miniaturization and scaling efforts brought on by the semiconductor industry[10], sub-10 nm thin films of $SiO_2$ have shown severe drift in measurement or unstable performance.[8,11,12] Drift in a biosensor is highly problematic because it prevents comparison of the signal before and after the addition of analyte as the background is always changing.

Oxide materials with high dielectric constant, κ, are of interest for use in biosensing as a route to improve device stability and facilitate device scaling. High-κ materials afford the ability to have a physically thicker gate dielectric than is possible with $SiO_2$ while maintaining device capacitance ($C$) as shown in Equation 1 where $\varepsilon_0$ is equal to the permittivity of free space, A is the area, and t is the oxide thickness.[8]

$$C = \frac{\varepsilon_o \kappa A}{t}$$

Equation 2-1

Despite numerous oxide materials, few possess the electronic properties, stability, compatibility with Si, and ease of fabrication required for incorporation into electronic devices. A list of dielectric constants of selected high-κ materials is presented in Table 1.[8]

**Table 2-1.** Comparison of dielectric constants (κ) of different gate dielectric materials.[8]

| Oxide | Dielectric constant (κ) | Band gap (eV) |
|---|---|---|
| $SiO_2$ | 3.9 | 9 |
| $Al_2O_3$ | 9 | 8.8 |
| $Ta_2O_5$ | 22 | 4.4 |
| $HfO_2$ | 25 | 5.8 |
| $ZrO_2$ | 25 | 5.8 |

$Al_2O_3$ is one material that has been used for the gate dielectric in recent biosensor designs.[13-15] In addition to a higher-κ value of 9 and a large band gap of 8.8 eV, high quality thin films of $Al_2O_3$ can be readily achieved by atomic layer deposition (ALD); a tool that is amenable to fast, surface limited thin film control.[16]

Altering the gate dielectric has presented new challenges for the immobilization of receptor molecules. SAMs of organosilanes with terminal amine or aldehyde functionality are the most common route of probe molecule attachment to oxide surfaces.[4,17] Despite excellent aqueous stability on $SiO_2$[18,19], reduced stability has been reported for silane-modified $Al_2O_3$ surfaces.[19-21] This observation has been attributed to the difference in bond polarity between Si-O bonds and Al-O bonds, which result in a polarized Si-O-Al linker that is vulnerable to cleavage.[21] In the case of APTMS, the vulnerability of the polarized bond is worsened by the localized pH increase from the amine groups. For biosensor applications, solution stability of the receptor attachment chemistry is critical therefore a different strategy to modify oxides was explored.

Phosphonic acids have been shown to exhibit stable, self-assembled monolayers (SAMs) on a variety of non-silica metal oxides.[17,22-24] Most work thus far has focused on molecular packing density and structure of alkyl phosphonic acid SAMs.[15,25] Less

information is available on short chains or those with terminal functional groups.[26-28] Since alkane phosphonic acids are not useful for covalent immobilization of receptor molecules, we focused on learning more about the chemistry of bifunctional phosphonic acids.

The first step of surface functionalization between the oxide and linker chemistry is critical for future attachment of probe molecules. The initial linker chemistry was examined by changes in the surface chemistry (surface wettability, atomic composition, or chemical bonds) or by chemical reactivity of the newly amminated surface provided by the linker compared to terminal hydroxyl groups present on a bare oxide.

## 2.2 Experimental Materials and Methods

### 2.2.1 Materials

Gold (III) chloride hydrate, 3-aminopropylphosphonic acid, 97% (APPA), bovine serum albumin (BSA), sodium dodecyl sulfate (SDS), N-cyclohexyl-2-aminoethanesulfonic acid (CHES), buffers, salts, and general chemicals were purchased from Sigma-Aldrich. 3-aminopropyltrimethoxysilane (APTMS) was obtained from TCI America. 2-carboxyethylphosphonic acid, 98% (CEPA) was acquired from Alfa Aesar. Dodecylphosphonic acid (DPA) and 12-mercaptophosphonic acid (MPA) was obtained from SiKÉMIA. Fisherfinest® premium microscope slides (3 in x 1 in x 1 mm) were purchased from Fisher Scientific. Sulfo-SMCC and EZ-Link® NHS-PEG4-Biotin was purchased from Pierce Protein Research Products, Thermo Scientific. Alexa Fluor® 488 streptavidin was obtained from Molecular Probes®, Life Technologies. DNA oligonucleotides were purchased from Integrated DNA Technologies Inc. Ethanol (EtOH,

200 proof) was supplied by Koptec. All water used unless noted was from a 18.2 MΩ:cm Nanopure water from a Barnstead system. All reagents were purchased without further purification. Buffer used for surface functionalization, reaction PBS, was prepared with EMD Chemicals HPLC grade water and contained 10 mM sodium phosphate and 300 mM sodium chloride at pH 7.4.

**Table 2-2**: DNA probe and target sequences

| Name | Sequence 5′→ 3′<br>For PNA N-Terminus → C-Terminus | Description |
|---|---|---|
| Thiol-Flu A DNA probe | Thiol-<br>TTTTTTTTTTGACCAATCCTGTCAC | Influenza A DNA probe |
| Thiol-Flu B DNA probe | Thiol-<br>TTTTTTTTTTTTCTTTTTTGTTGCT | Influenza B DNA probe |
| Amine-Flu A PNA probe | Amine-<br>TTTTTTTTTTGACCAATCCTGTCAC | Influenza A DNA probe |
| Amine-Flu B PNA probe | Amine-<br>TTTTTTTTTTTTCTTTTTTGTTGCT | Influenza B DNA probe |
| A647 Flu A DNA target | Alexa Fluor 647-GTGACAGGATT | Alexa647 Influenza A DNA target |

### 2.2.2 Synthesis of Au Nanoparticles

Colloidal Au nanoparticles were prepared, as described previously[29,30] by citrate reduction of $HAuCl_4$. Nanoparticle images were collected using a JEOL 1200 EX II transmission electron microscope. Average nanoparticle diameter of 11.6 ± 1.3 nm was calculated using Image J software (661 particles counted). The colloidal suspension absorbance was determined by visible spectroscopy with a Hewlett-Packard 8453 diode-

array spectrometer and Agilent ChemStation software and used to calculated a nanoparticle concentration of 17.9 nM ($\varepsilon_{520}$=3.64x$10^8$/(M·cm).

### 2.2.3 Functionalization of $SiO_2$ and $Al_2O_3$ with APTMS/Au NPs

Thin film deposition of $Al_2O_3$ (10 nm) on both sides of a glass microscope slide was carried out using a Cambridge Savannah™ 200 atomic layer deposition (ALD) tool with trimethylaluminum and water precursors at 200ºC. Glass slides, as purchased or $Al_2O_3$-coated were cut to 1 x 3 mm pieces, rinsed with EtOH, and dried with $N_2$. Solutions of 3% APTMS were prepared in 1.5 mL microcentrifuge tubes with 200 proof EtOH. Glass slides were added to the solutions and allowed to react at room temperature for up to 8 hours, or 90ºC for up to 5 hours. Slides were briefly rinsed with EtOH and those reacted at room temperature were cured at 120ºC for 1 hour while standing in glass vials. After a thorough rinse with water, slides were placed in 11.6 ± 1.3 nm gold nanoparticles for 30 minutes. The samples were rinsed and stored in water until analyzed by visible spectroscopy.

### 2.2.4 Functionalization of $Al_2O_3$ with APPA/Au NPs

Thin film deposition of $Al_2O_3$ (10 nm) on both sides of a glass microscope slide was carried out as described above. Cut, $Al_2O_3$-coated samples were rinsed with EtOH, and dried with $N_2$. Samples were added to aqueous solutions of 1 mM or 5 mM APPA, prepared in 1.5 mL microcentrifuge tubes, at room temperature for up to 6 days, or 50ºC or 70ºC up to 2 days. Slides were briefly rinsed with EtOH and those reacted at room temperature were cured at 120ºC for 1 hour while standing in glass vials. After a

thorough rinse with water, samples were placed in 11.6 ± 1.3 nm gold nanoparticles for 30 minutes. The samples were rinsed and stored in water until analyzed by visible spectroscopy.

### 2.2.5 Characterization of Phosphonic Acids on $Al_2O_3$

Contact angle (CA) was collected with a Ramé-hart Model 295 Automated Goniometer/Tensiometer using DROPimage Advanced software. X-ray photoelectron spectra were acquired with a Kratos Analytical Axis Ultra x-ray photoelectron spectrometer. Samples were prepared on 2 x 2 cm pieces Si wafer coated with 10 nm $Al_2O_3$ by ALD. Aqueous solutions of APPA or CEPA, and EtOH solutions OPDA were prepared at 1 mM or 5 mM concentration in 15 mL polytetrafluoroethylene (PTFE) jars for up to 6 days at room temperature or up to 2 days 90ºC. Sodium hydroxide (100 mM) was used to adjust two samples for XPS to pH 7.

Infrared (IR) samples were prepared two ways: 1. Microscope slides were coated with 10 nm Ti followed by 100 nm Al using Kurt Lesker Lab-18 e-beam evaporation. Deposition of $Al_2O_3$ (10 nm) on the Al-coated slide was carried out as described above. Slides were reacted in aqueous solutions of 5 mM APPA or CEPA in plastic microscope slide mailers for 1 day. 2. A 3-inch Si wafer was cut into quarters. Each piece was thoroughly rinsed with water and EtOH then dried with $N_2$. A piranha solution was prepared with 3:1 sulfuric acid and 30% $H_2O_2$. Wafers were placed in the piranha for 30 minutes, rinsed thoroughly with water, and dried with $N_2$. A thin film (10 nm) of $Al_2O_3$ was deposited by ALD as described previously. Aqueous solutions of 1 mM or 5 mM APPA were prepared in 30 mL polytetrafluoroethylene (PTFE) jars. Samples were

placed in the jars for 1 or 3 days. All samples were rinsed with water, dried with $N_2$, and analyzed with a Bruker IFS 66/S FT-IR Spectrometer equipped with a Harrick VariGATR grazing angle ATR. OPUS spectroscopy software was used to collect and analyze IR data.

### 5.2.4 DNA Preparation

DNA arrived as a lyophilized pellet from Integrated DNA Technologies, Inc. Prior to use, thiol-terminated DNA was rehydrated in a 100 mM solution of DL-dithiothreitol in 10 mM sodium phosphate buffer at pH 8.3 to cleave any disulfide bridges present. After 1 hour, the solution was desalted with a Princeton Separations (Adelphia, NJ) Centrispin 10 column, resulting in a solution of individual thiol-terminated DNA oligonucleotides.[31] Amine-terminated DNA and fluorescently-labeled DNA were rehydrated in 18.2 MΩ:cm Nanopure water. The sequence concentration of DNA was determined by measuring the solution absorbance at 260 nm using a Hewlett-Packard 8453 diode-array UV/visible spectrometer with Agilent ChemStation software. Sequences were diluted to either 100 μM or 20 μM and stored at -80°C.

### 2.2.6 Fabrication and Functionalization of Al Tiles with Biotin/Streptavidin

Germanium-coated Si wafer was obtained from Xiahua Zhong from Dr. Theresa Mayer's group. The wafer was rinsed with acetone, isopropyl alcohol, and dried on a hot plate. Hexamethyldisilazane (HMDS) was spun onto the wafer surface and baked for 1 min at 115ºC. BPRS-100, a negative photoresist, was spun onto the wafer surface and baked at 115ºC for 90 seconds. The tiles were patterned onto the wafer using a GCA

8000 i-line stepper and developed in 3:1 solution PLSI:water for 1 minute. The wafer was rinsed with water, dried with $N_2$, and descummed in $O_2$ plasma using a Metroline M4L Plasma Etcher. A Kurt Lesker Lab-18 evaporator was used to deposit 150 nm Al by electron beam evaporation onto the wafer surface. Liftoff was achieved in a room temperature acetone soak for 2-3 hours. The wafer was cut into smaller pieces, placed into a 1.5 mL centrifuge tube in 30% $H_2O_2$ heated to 50ºC until tiles were visually released from the silicon substrate (1-2 hours).

Released Al tiles were rinsed with water and combined into one centrifuge tube, supernatant removed. A 5 mM aqueous solution of APPA was added to the tube, which was vortexed for 3 days. Half of the tiles were subsequently reacted with 2 mg NHS-PEO-Biotin in 1 mL water for 2 hours. Al tiles were rinsed with water, and reacted in 5 $\mu$g Alexa Fluor® 488 streptavidin in 1 mL water for 2 hours. Reflectance and fluorescence images of tiles were obtained using Image-Pro Plus software with a Nikon TE-300 inverted microscope equipped with a Xe arc lamp and Photometrics Coolsnap HQ camera. A Plan Apo 60x or Nikon Plan Fluor 100x oil objective was used. Samples were prepared by placing a 10 µL DI suspension of tiles onto a glass slide with a coverslip.

### 2.2.7 Microarray Printing of DNA Probe onto Oxide Functionalized Surfaces

A general microarray protocol printed by the PSU DNA Microarray Facility was followed to prepare microarray samples.[32] Preprocessing/slide clean- Prior to use, microscope slides were labeled (which was considered the “front” surface) with a diamond scribe, then boiled in DI water for 3 minutes and sonicated in EtOH for 1 min.

Last, slides were dried by $N_2$. Functionalization-Solutions of 3% APTMS in EtOH (2 mL) were delivered to the front of the slides and allowed to react in a sealed petri dish (to prevent evaporation) for 1 hour. Alternatively, slides were reacted in solutions of 5 mM APPA in water or 5 mM MPA in EtOH at 60°C for 2 days. For APTMS and APPA functionalized surfaces, 2 mL solution of secondary linker, Sulfo-SMCC, at 1 mg/mL in 10 mM CHES buffer, pH 9.5, was delivered to the front of each slide and allowed to react for 1 hour. Slides were rinsed with water, and dried by $N_2$. A secondary linker on MPA functionalized slides was not attached because the crosslinking chemistry was performed on the $NH_2$-terminated DNA instead. In either case, the remaining stable, maleimide reacts with sulfhydryl groups (from thiolated DNA for APTMS and APPA samples or terminal thiol on MPA) to covalently attach DNA to the surface. Slide printing- Slides were printed at the Genomics Core Facility at the University Park Campus at Pennsylvania State University by Dr. Craig Praul using a GeneMachines OmniGrid Arrayer. Complementary and Non-complementary DNA probe (40 μM in 2X spotting buffer) was spotted on the surface. Prehybridization/blocker-After spotting, slides were soaked in a prehybridization/ blocking buffer for 45 minutes. The buffer contained 12.5 mL 20X SSC buffer (3 M NaCl + 300 mM sodium citrate), 500 uL 10% SDS, 0.5 mg BSA, and DI to fill 50 mL. Slides were rinsed with DI water followed by isopropyl alcohol and allowed to air dry. Hybridization- Slides were arranged in a petri dish, fluorescent target DNA (Flu A, 2 mL) was delivered to the slide, and samples were sealed, then covered with aluminum foil to protect from light for 24 hours. Post-hybridization wash- After hybridization slides were immersed in buffer/rinse solutions as follows: 2X SSC + 0.1% SDS- 3 minutes, 1X SSC-2 minutes, 0.2X SSC-1 minute, and

0.05X SSC-10 seconds. Lastly, slides were dried with $N_2$ and stored in the dark until imaging. Images were collected by GenePix 4000B scanner and GenePix Pro Software.

## 2.3 Results and Discussion

Surface modification of dielectric materials plays a critical role in the development of biomolecule-based sensors. The first step, functionalization of the gate dielectric, is most important, as remaining coupling chemistries are dependent upon the initial covalent attachment to the surface. The work in this chapter began with a comparison of 3-aminopropyltrimethoxysilane (APTMS) modified $SiO_2$ and $Al_2O_3$ surfaces. Functionalization of $Al_2O_3$ with a related phosphonate, 3-aminopropylphosphonic acid (APPA) is shown. Several reaction conditions for APPA with $Al_2O_3$ were examined to optimize surface coverage and minimize reaction time. Characterization of the functionalized surfaces with contact angle, x-ray photoelectron spectroscopy, and infrared spectroscopy was performed. Detection of target DNA was demonstrated on lithographically prepared aluminum tiles with APPA after attachment of probe chemistries. Lastly, microarray printing of DNA probe to oxide functionalized surfaces is shown as a method to quantify DNA hybridization on a planar surface.

### 2.3.1 Surface Functionalization of $SiO_2$ and $Al_2O_3$ with APTMS

First, to enable rapid comparison of APTMS on $SiO_2$ and $Al_2O_3$, electrostatic AuNP self-assembly based on literature precedent for the APTMS/silica system was used.[29,30] An advantage of this technique when studying surface chemistry is its simplicity and low cost.[33] At neutral pH, self-assembly of 3-aminopropyltrimethoxysilane (APTMS) results

in positively charged surface due to protonated terminal amine groups. Subsequent reaction of the surface with negatively-charged Au nanoparticles (AuNP) results in a film of AuNPs that can be monitored and quantified by the expected absorption band near 528 nm using visible spectroscopy (Figure 2-1).[29,30]

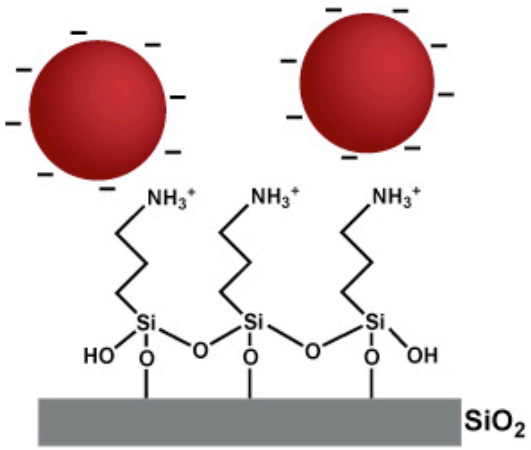


**Figure 2-1.** Schematic of APTMS-functionalized $SiO_2$ after adsorption of citrate-reduced AuNP. Not drawn to scale.

Transmission electron microscopy (TEM) and visible spectroscopy were used to characterize AuNPs synthesized for this work (Figure 2-2). AuNP were determined to have an average diameter of 11 nm by measuring the diameter of 661 particle using Image J software and a solution concentration, determined by maximum solution absorbance of ~18 nM.

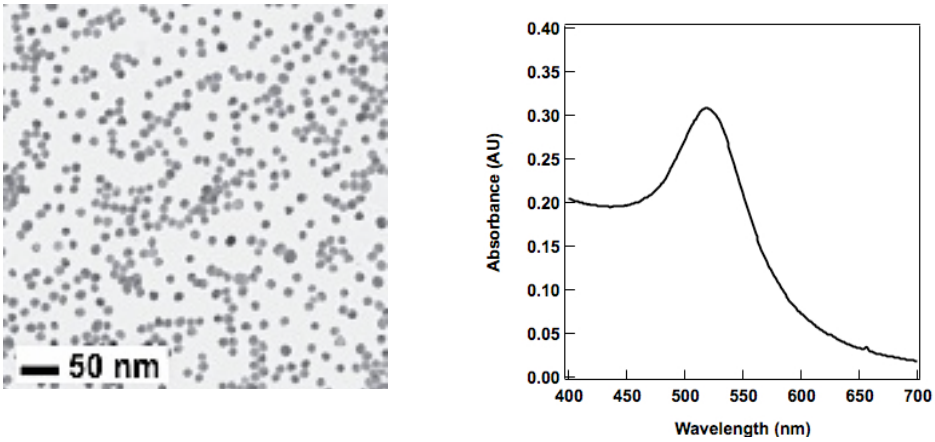


**Figure 2-2.** TEM image (A) and absorbance spectrum (B) of synthesized AuNP with an average diameter of 11 nm and particle concentration of ~ 18 nM.

Comparison of visible spectra from APTMS-modified $SiO_2$ or $Al_2O_3$ samples after incubation in solutions of AuNP demonstrates higher surface coverage of AuNP was obtained for $SiO_2$ surfaces (Figure 2-3). The maximum absorbance at 528 nm was 0.154 and 0.050, for $SiO_2$ or $Al_2O_3$, respectively. The resulting NP surface coverage (in particles/cm$^2$) can then be calculated[34,35] given the maximum absorbance of the surface ($A_{surf}$ -divided by two to account for the front and back surface) and surface extinction coefficient ($\varepsilon_{surf}$) at 524 nm as shown in Equation 2-1. This results in 1.7 x $10^{11}$ and 5.4 x $10^{10}$ particles/cm$^2$ for $SiO_2$ or $Al_2O_3$, respectively.

$$A_{surf} = \frac{\Gamma \cdot \varepsilon_{surf}}{6.02x10^{20}} \qquad \text{Equation 2-2}$$

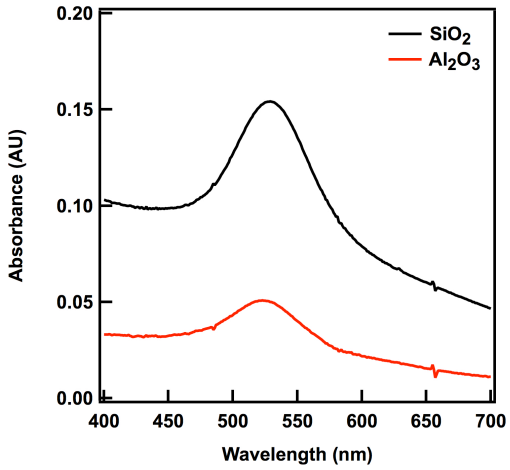


**Figure 2-3** The absorbance spectrum of AuNPs adsorbed to APTMS on $SiO_2$ (black) or $Al_2O_3$ has a maximum absorbance peak near 528 nm with an average absorbance intensity of 0.155 and 0.050, respectively.

Reaction of APTMS with $Al_2O_3$ was expected to be straightforward based on literature reports of similar silane chemistries being used on $Al_2O_3$.[13,14] However, AuNP experiments with APTMS and $Al_2O_3$ revealed samples with much lower maximum absorbance values between samples compared to those of APTMS and $SiO_2$. It had been reported that APTMS physisorbs to the surface of $SiO_2$, $TiO_2$, and $ZrO_2$ at room temperature and a cure step at elevated temperature could promote covalent attachment.[19] This process was applied to $Al_2O_3$ samples. After reaction in APTMS, samples were rinsed with EtOH to remove excess molecules then cured in an oven at 120°C for 1 hour, followed by incubation in AuNP. The additional curing step improved AuNP maximum absorbance intensity slightly, however significant variability between samples, shown as replicate spectra, remained problematic and was attributed to the rinsing steps before and after curing (Figure 2-4, A). Alternatively, Chabal and coworkers found elevated reaction temperatures instead of a post-deposition cure is optimal to promote covalent

attachment of APTMS to $SiO_2$.[18] This approach was used for the reaction of $Al_2O_3$ samples for 2 hours at 90°C in a 3% APTMS followed by incubation in AuNP. An improvement in the reproducibility of samples was observed, but at the expense of high surface coverage (Figure 2-4, B). New samples were prepared at 90°C and reacted in APTMS for 5 hours instead. In Figure 2-4, C; it is clear the reproducibility was greatly improved compared to the room temperature sample and the 90°C sample for 2 hours. This appeared to be one route to modify $Al_2O_3$ with APTMS but a comparison of the best example of APTMS modified $Al_2O_3$ (Figure 2-4, C) with a $SiO_2$ functionalized with APTMS (Figure 2-3) reveals 2-fold less particles per $cm^2$ are adsorbed on the $Al_2O_3$-coated surface.

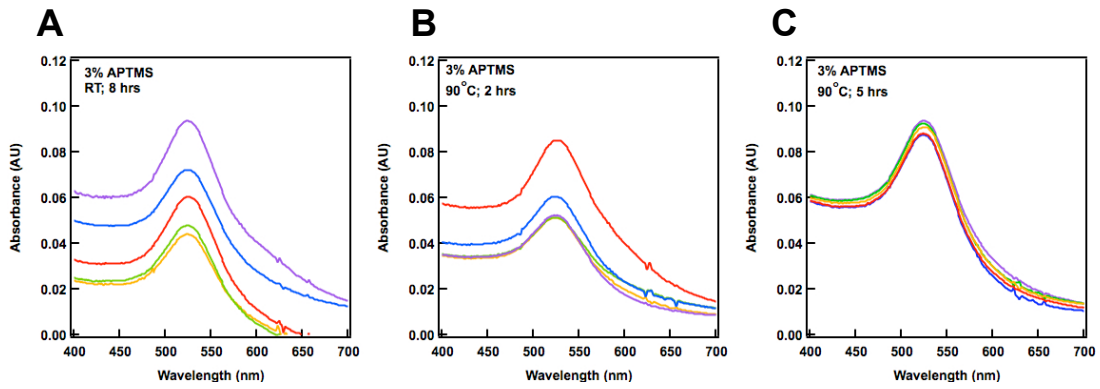


**Figure 2-4** Absorbance spectrum of AuNPs adsorbed to APTMS modified $Al_2O_3$ after reaction in APTMS at room temperature for 8 hours with a 1 hour post-deposition cure at 120°C (A), 90°C for 2 hours (B), or 90°C for 5 hours (C).

### 2.3.2 Surface Functionalization of $Al_2O_3$ with APPA

While silanes have provided an excellent route to functionalize $SiO_2$, use with other oxides, in particular for solution-based applications, may be less desirable. Phosphonic acids are known to form stable, ordered monolayers on a variety of metal oxides.[17,36] We

chose to begin with a phosphonic acid molecule analogous in structure to APTMS, 3-aminopropylphosphonic acid (APPA). $Al_2O_3$ was reacted with aqueous solutions of APPA under a variety of reaction conditions in order to achieve uniform and high surface coverage of adsorbed AuNPs. Despite changes in reaction time, reaction temperature, or solution concentration, the resulting absorbance spectra demonstrated mostly non-uniform or low AuNP coverage ~ 4 x $10^{10}$ particles/$cm^2$ (Figure 2-5). A post-deposition cure step for phosphonic acids was also attempted but resulted in no improvement (data not shown). Despite lower AuNP surface coverages, the stability of APPA covalent attachment to $Al_2O_3$ and the availability of terminal functional groups for subsequent reaction remained an interest. Further surface chemistry characterization to directly probe the nature of monolayer formation on $Al_2O_3$ was desired.

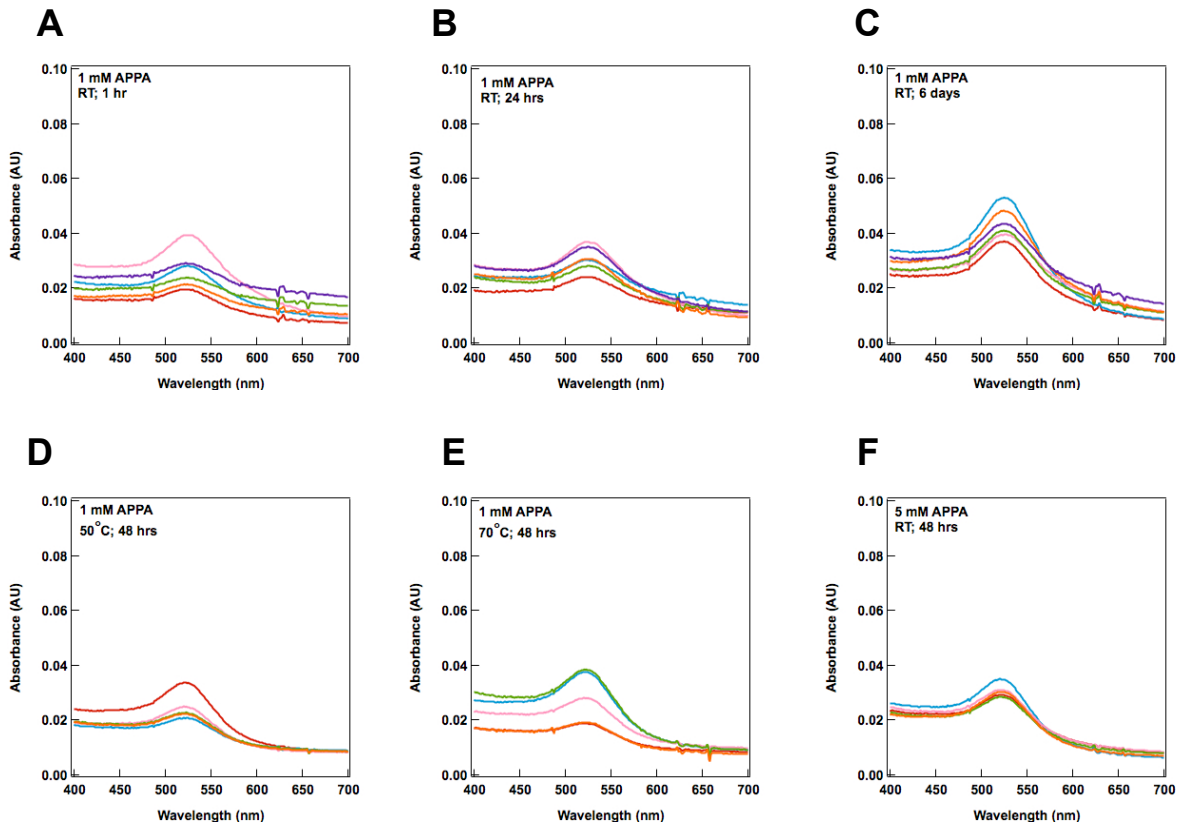


**Figure 2-5.** Absorbance spectrum of AuNPs adsorbed to APPA on $Al_2O_3$ has a maximum absorbance peak near 528 nm. Reaction conditions were varied to determine optimal procedure. As shown, $Al_2O_3$-coated slides were reacted in 1 mM APPA at room temperature for 1 hour (A), 24 hours (B) and 6 days (C); or at elevated temperatures of 50ºC (D) or 70ºC (E) for 2 days. Samples were also reacted in 5 mM APPA for 2 days (F). Replicate samples for each set of conditions are shown as separate spectra.

### 2.3.3 Characterization of Surface Functionalization of $Al_2O_3$ with Phosphonic Acids

For biosensing purposes, a reduction in linker surface coverage is not necessarily problematic due to the size and thus steric hindrance of future biomolecule attachment. However, AuNP studies were an indirect method to assess phosphonic acid monolayer formation and it was important to demonstrate uniform surface coverage and covalent

attachment of the linker chemistry. This was accomplished using contact angle (CA), infrared spectroscopy (IR), and x-ray photoelectron spectroscopy (XPS).

As previously discussed, less quantitative literature was available about short chain phosphonic acids or those with functional terminal groups, so we took a step back and looked at assembly of a variety of phosphonic acids (Figure 2-6, A) in an attempt to repeat published work. Figure 2-6, B shows the resulting static contact angles obtained from different phosphonic acids reacted with $Al_2O_3$. The successful functionalization of $Al_2O_3$ with phosphonic acids can be seen by the dramatic change in surface wetting properties based on the surface chemistry. DPA, a long chain alkyl phosphonic acid, was very hydrophobic with a contact angle of 93.29°. Long chain phosphonic acid with a terminal thiol group, MPA, had an intermediate contact angle of 79.27° and short chain amine-terminal phosphonic acid, APPA, was very hydrophilic contact. In fact, it wet the surface so well that an angle could not be determined. For comparison, an oxide sample was stored in EtOH without any linker and the resulting contact angle was 57.39°.

**A**

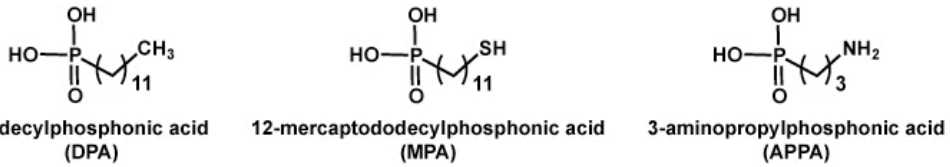


**B**

| Surface Chemistry | Contact Angle (degrees) |
|---|---|
| DPA | 93.29 ± 0.25 |
| MPA | 79.27 ± 0.33 |
| APPA | * |
| Bare oxide | 57.39 ± 0.63 |

**Figure 2-6** (A) Structure, chemical name, and abbreviation of phosphonic acids reacted with $Al_2O_3$ for static, sessile drop, contact angle measurements. (B) Table of phosphonic acid SAMs collected on Si wafer coated with ALD $Al_2O_3$. * indicates the surface was completely wetted and a contact angle could not be determined. Bare oxide sample was stored in EtOH prior to measurement.

To verify covalent attachment of the phosphonic acids to $Al_2O_3$, infrared spectroscopy (IR) was used to probe the P-O stretching region. Aluminum metal was deposited onto microscope slides, which were then immersed in solutions of carboxy (CEPA)- and amine (APPA)-terminated phosphonic acids. The resulting coatings were analyzed with infrared spectroscopy (Figure 2-8).

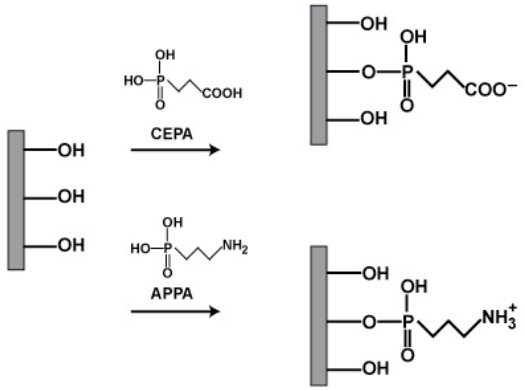


**Figure 2-7.** Cartoon of reaction between oxide surface of $Al_2O_3$ with CEPA or APPA molecules.

Comparison of spectra showed a strong peak for all samples at 950 $cm^{-1}$ from the Al-O bond and a small peak at 1125 $cm^{-1}$ from the P-O stretch in CEPA and APPA modified surfaces compared to the bare oxide (Figure 2-8).[23,37] Unfortunately, the large Al-O bond made peak assignment more difficult because it obscures most P-O and P=O stretches that support evidence of covalent attachment. However, the broad peak ~1100 $cm^{-1}$ is characteristic of covalently bound phosphonate which indicated the phosphonate is attached to the surface, not physisorbed.[37] Since APPA and CEPA molecules appeared to react similarly with $Al_2O_3$, we proceeded forward with APPA in future experiments due to the ease of later functionalization steps for amine-terminated surfaces.

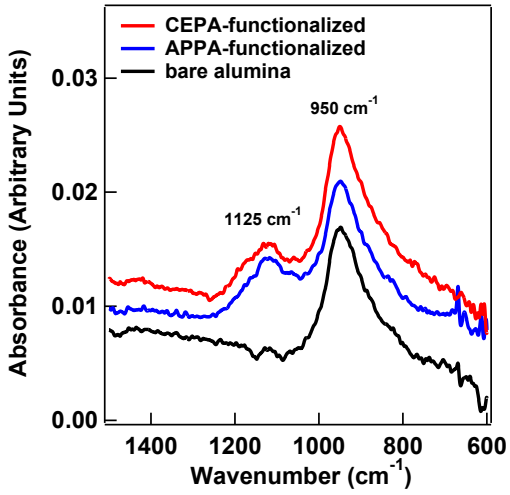


**Figure 2-8.** Infrared spectra show a strong peak due to the Al-O bond at 950 $cm^{-1}$ in all samples and a small peak at 1125 $cm^{-1}$ from P-O stretch in CEPA (red) and APPA (blue) modified surfaces compared to the bare oxide (black).

### 2.3.4 Effect of Optimized Reaction Conditions on Surface Functionalization of $Al_2O_3$ with APPA

For optimization of reaction conditions, $Al_2O_3$ was deposited on bare silicon wafer instead of Al metal deposition on glass slides to obtain higher quality spectra. Upon reaction in aqueous solution of 5 mM APPA, the infrared peak due to P-O stretching[23,37] at 1125 $cm^{-1}$ increased from 1 day to 3 days (Figure 2-9), which indicated an increase in the surface coverage of covalently bound molecules. This demonstrates the functionalization process in indeed much slower than for APMTS on silica which can be completed in minutes.[35]

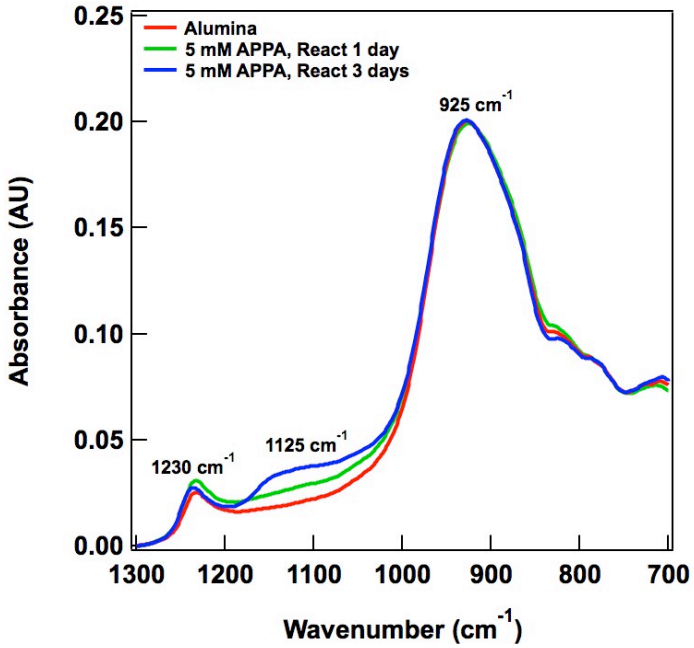


**Figure 2-9** IR spectrum of $Al_2O_3$-coated silicon wafer with bare alumina (red) or after reaction in 5 mM APPA for 1 day (green) or 3 days (blue). Peaks at 1230 $cm^{-1}$, 1125 $cm^{-1}$, and 925 $cm^{-1}$ are due to Si, P-O, and Al-O, respectively.

X-ray photoelectron spectroscopy (XPS) was used to monitor surface coverage with changes in reaction conditions. This method was advantageous as it enabled smaller sample sizes and resulted in well-defined, high-resolution peaks for easy comparison. In Figures 2-10, A and B; the surface content of phosphorus and nitrogen after reaction with APPA was determined for samples reacted with 5 mM APPA for varying times. In agreement with IR, increasing reaction times also increased the surface coverage of APPA, which continued even out to seven days. This is non-ideal because long reaction times are not amenable to high-throughput processing.

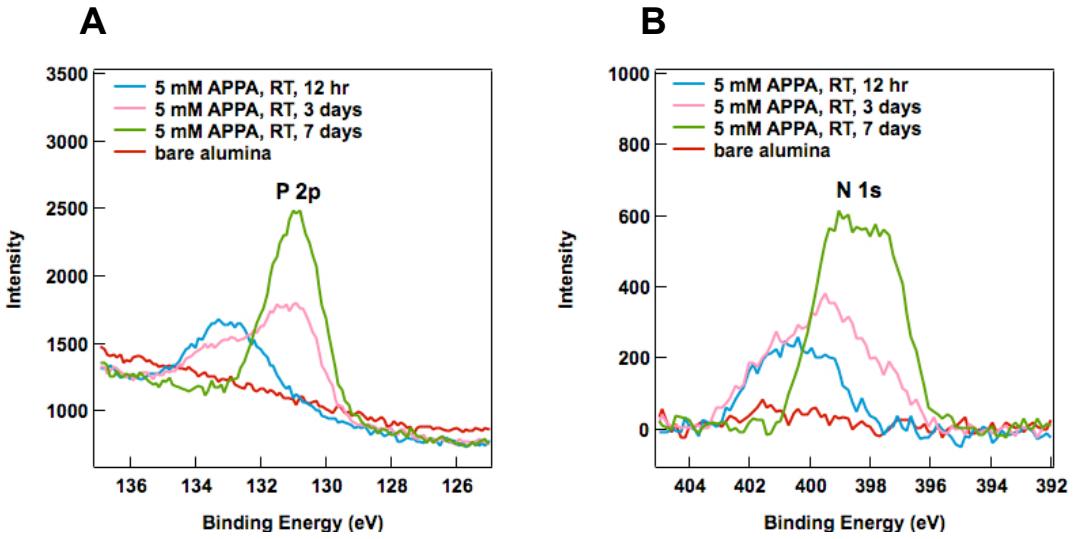


**Figure 2-10** High-resolution XPS spectra of (A) P 2p or (B) N 1s orbitals of $Al_2O_3$-coated silicon wafer without phosphonate SAM (red) or after reaction in 5 mM APPA for 12 hours (blue), 3 days (pink), or 7 days (green).

A series of XPS experiments were performed on $Al_2O_3$-coated Si wafers to determine optimal reaction conditions to minimize reaction time and maximize surface coverage. The effect of solution temperature or pH with an APPA reaction time of either 1 day or 2 days was examined. In Figure 2-11, solid lines correspond to samples that were reacted for 1 day where dotted lines are samples that were reacted for 2 days. All 2 day samples had higher phosphorus and nitrogen content compared to their respective 1 day samples with the exception of a reaction temperature at 90°C where the difference was negligible. However, both 60°C reaction temperature samples were significantly higher than all other samples, including other 2 day samples. This lead us to believe that a higher reaction temperature of 60°C facilitates SAM formation. Aqueous solutions of 5 mM APPA have a pH near 4. Adjustment of solution to pH 7 resulted in the lowest content of phosphorus and nitrogen.

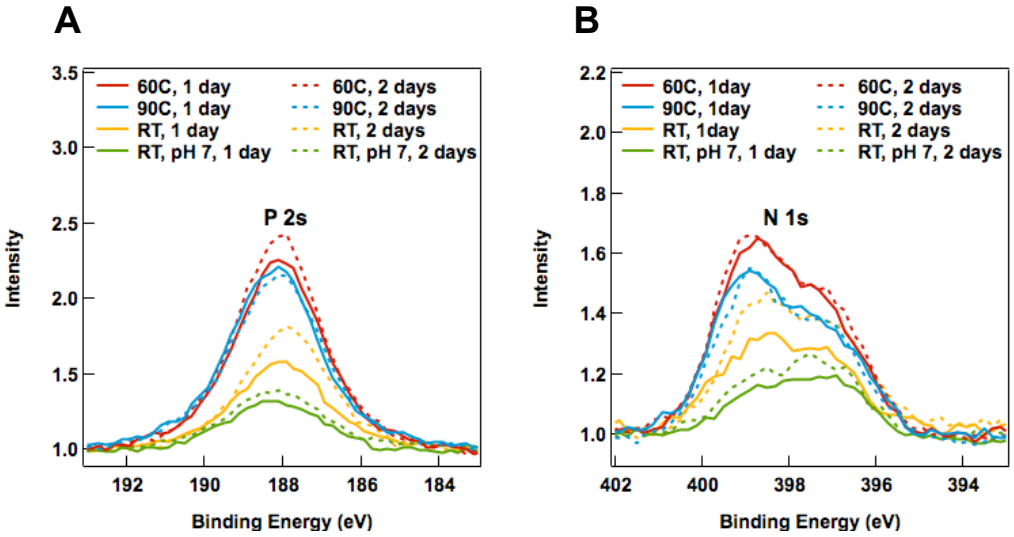


**Figure 2-11** High-resolution XPS spectra of (A) P 2s (B) N 1s orbitals of $Al_2O_3$-coated silicon wafer after reaction in 5 mM APPA at 60°C (red), 90°C (blue), room temperature (yellow) or at room temperature with solution pH adjustment to 7.0 (green). Samples remained in solution for either 1 day (solid lines) or 2 days (dotted lines).

### 2.3.5 Fabrication and Functionalization of Al Tiles with Biotin/Streptavidin

Following determination of optimized reaction conditions for APPA on $Al_2O_3$, 60ºC for 24 hours, a bioassay was performed to demonstrate the ability immobilize receptor molecules for the capture of analyte. Aluminum tiles, fabricated by standard lithographic processes (Figure 2-12), were used to demonstrate the use of APPA to couple biotin-streptavidin to $Al_2O_3$-coated surfaces.

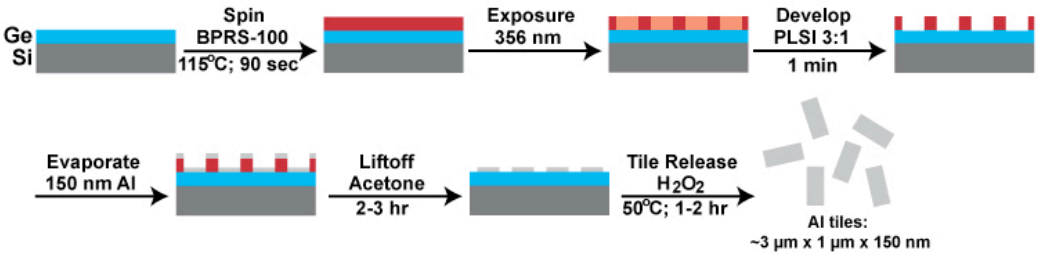


**Figure 2-12** Cartoon of process used to lithographically fabricate Al tiles.

Biotin-streptavidin chemistry is commonly used for proof-of-concept biosensor applications. It is well known for its noncovalent, high affinity, binding interaction that is stable under a variety of reaction conditions including DI water or buffer regardless of salt concentration, extreme pH, or temperature.[38] Successful attachment of biotin and specific detection of Alexa Fluor® 488-streptavidin is demonstrated on Al tiles in Figure 2-13. Biotinylated tiles demonstrate excellent specificity with a mean fluorescence intensity of 20 compared to 2 for tiles that were functionalized with APPA only. The coverage and mean fluorescence intensity was low and appeared uneven across the surface of the tiles but could be further improved by optimization of the particle-based system.

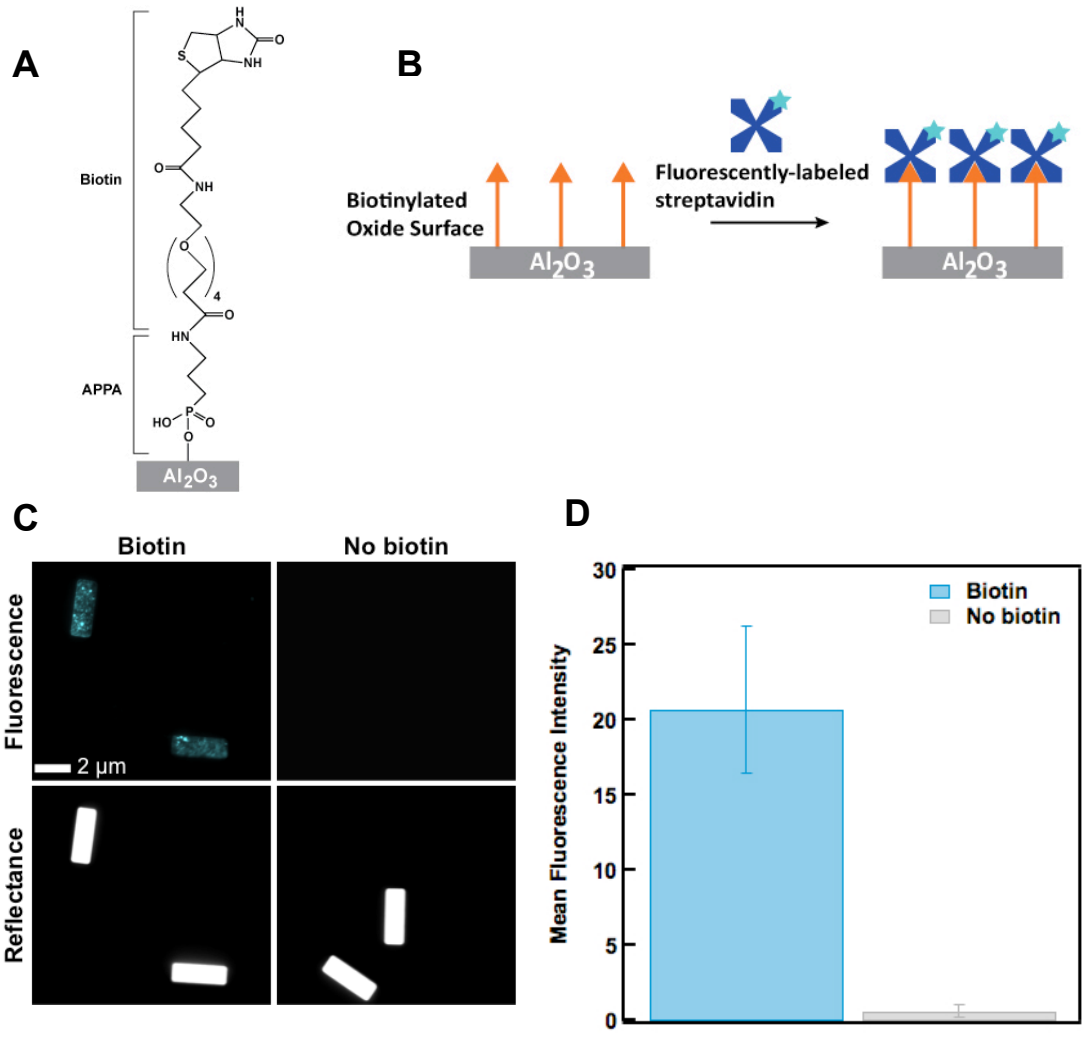


**Figure 2-13** (A) Al tiles reacted first with APPA; biotinylated samples reacted with NHS-PEG4-Biotin. (B) Aqueous solution of fluorescent streptavidin was reacted with samples and bound to biotin. (C) Mean fluorescence intensity of fluorescence images (D) from biotinylated and no biotin samples demonstrated a 10-fold increase.

### 2.3.4 Microarray Printing for Oxide Surface Functionalization Analysis

Demonstration of surface functionalization of oxides was evaluated next on planar surfaces using microarray printing. This technique enabled a high capacity of data (spots) with automated fluorescence detection using a fluorescence scanner and software.

First, method validation was demonstrated with $SiO_2$ and APTMS. Given the general cartoon in Figure 2-14, A; Flu A or Flu B probes were spotted onto the surface after attachment of linker chemistries followed by hybridization in fluorescently-labeled Flu A target DNA. Comparison of fluorescence from a sample that was (Figure 2-14, B) functionalized with linker chemistries (APTMS and bifunctional crosslinker, Sulfo-SMCC) followed by DNA probe and target or (Figure 2-14, C) DNA probe and target alone, demonstrate highly selective DNA target hybridization is observed with the use of linker chemistries. Comparison of replicate samples (shown as individual bars) and replicate spots within the same sample (shown by error bars) indicated reasonable uniformity within the same sample and between different samples (Figure 2-14, D). This process was successful; however, lower target DNA concentration was desired because many spots reached the maximum limit of the detector.

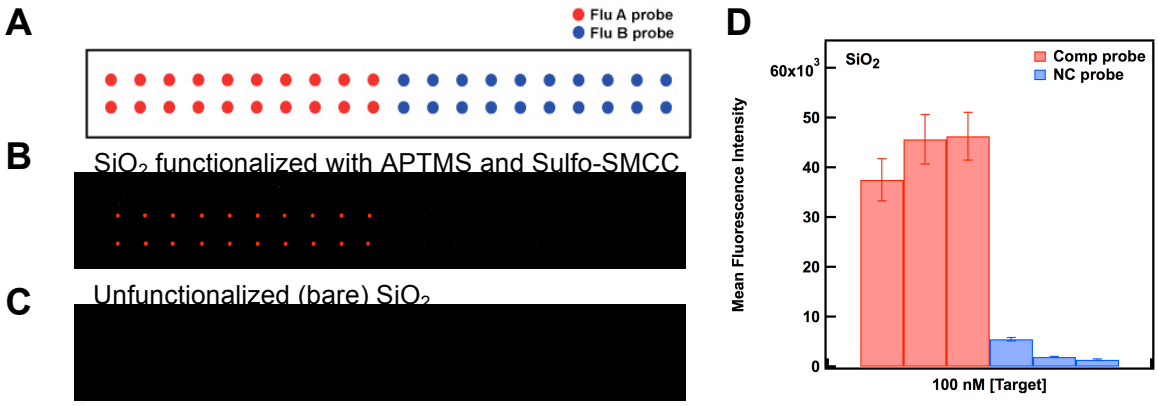


**Figure 2-14** (A) Cartoon of microarray printing pattern of complementary (Flu A, red) and non-complementary (Flu B, blue) probe DNA. Fluorescence images obtained with a microarray scanner show selective fluorescence at locations spotted with Comp probe DNA when $SiO_2$ is functionalized (B) with APTMS and Sulfo-SMCC compared to (C) the bare oxide alone. (D) Replicate samples from functionalized slides (shown as individual bars) are displayed by averaging fluorescence counts from twenty spots (shown by error bars).

Next, the experiment was repeated using lower DNA target concentration, $SiO_2$, $Al_2O_3$, or $HfO_2$ surfaces, and APTMS. As shown in Figure 2-15, selectivity of this assay remained very high as no appreciable fluorescence was observed for any non-complementary target DNA samples. Upon comparison of the different oxides, $HfO_2$ had the highest mean fluorescence intensity and most uniformity among the twenty spots; $SiO_2$ and $Al_2O_3$ had similar fluorescence intensity, although $Al_2O_3$ had much larger variability. Despite concerns about long-term stability of APTMS-functionalized metal oxides in aqueous solution[19,21], these data demonstrate that APTMS-functionalized $Al_2O_3$ and $HfO_2$ surfaces enabled successful DNA detection, which involved a 24 hour incubation step in reaction buffer (10 mM sodium phosphate and 300 mM sodium chloride, pH 7.4).

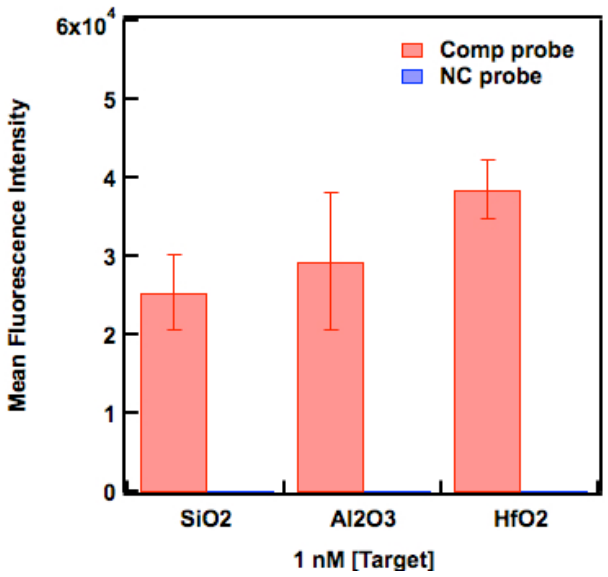


**Figure 2-15** Average fluorescence counts from twenty spots (shown by error bars) after incubation in 1 nM fluorescently labeled target DNA on APTMS functionalized $SiO_2$, $Al_2O_3$, or $HfO_2$.

While this was successful at demonstrating the functionalization of different oxides, albeit with APTMS, variability in complementary samples was a concern and the optimal target concentration was questioned. In a series of two experiments, a range of target concentrations was examined to determine the optimum concentration of target DNA using $SiO_2$ and APTMS. In Figure 2-16, the mean fluorescence intensity from spots with complementary probe DNA is shown as a function of DNA target concentration where error bars indicate the average fluorescence from twenty spots. Initially target concentration was probed from 10 pM to 3 nM, but large error at lower target concentrations and limited data points made analysis difficult (Figure 2-16, A). The experiment was repeated with a several target more target concentrations ranging from 1 pM to 0.3 nM (Figure 2-16, B). This binding assay demonstrates at higher target concentration, small difference in DNA target can result in large changes in mean fluorescence intensity therefore, to minimize small variations between experiments, it is best to use 10-100 pM target.

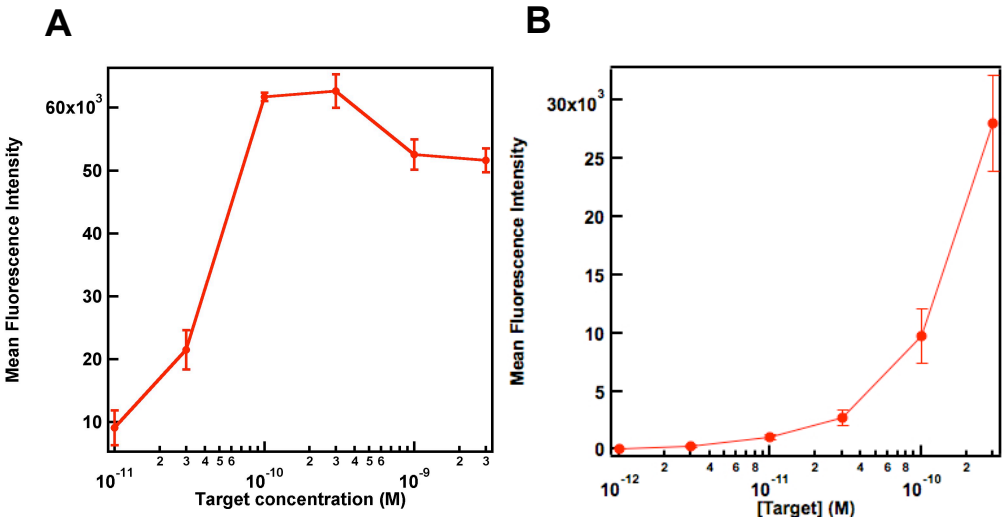


**Figure 2-16** (A) Mean fluorescence intensity resulting from incubation of probe-functionalized $SiO_2$ with a range of different target concentrations. Experiment was repeated, (B), with lower concentrations of target concentrations. Error bars indicate average fluorescence from twenty spots.

After validating the chemistry and microarray setups, the experiment was repeated with $SiO_2$, $Al_2O_3$, and $HfO_2$ surfaces and APTMS, APPA, and MPA linkers however several problems were encountered. As previously shown, APPA had a highly hydrophilic surface, which caused probe spots to spread and combine on the surface. Additionally, MPA gave higher fluorescence for thiolated probe than amminated probe, which indicated the chemistry had not functionalized as anticipated. Selectivity was maintained since the probe that did attach was selective for the correct target, hence the chemistry could be used going forward, but further evaluation of the MPA chemistry would be needed to understand what happened. Still, this technique demonstrated excellent sensitivity and selectivity for bioassays on $SiO_2$ surfaces with APTMS and MPA.

## 2.4 Conclusions

This work examined several functionalization strategies on dielectric materials. Traditional silane chemistry, which has been exhaustively studied on $SiO_2$, has had less attention on other materials, such as $Al_2O_3$ and $HfO_2$. Upon comparison of a microarray bioassay, similar mean fluorescent intensity was found on all three surfaces after functionalization with APTMS and probe DNA and hybridization with fluorescently-labeled target DNA. Characterization of alternative functionalization chemistries using phosphonic acids was explored with $Al_2O_3$. Elevated reaction temperatures, at 60ºC, were optimal for high surface coverage in minimal time; however, in comparison to APTMS, phosphonates required much longer reaction times. A goal of this work, to establish a stable, covalent, immobilization strategy on high-*k* dielectrics, was successfully accomplished as shown by a bioassay that exhibited excellent selectivity to a solution of streptavidin protein using APPA-functionalized Al tiles.

## 2.5 References

1. Wink, T.; van Zuilen, S. J.; Bult, A.; van Bennekom, W. P. Self-Assembled Monolayers for Biosensors. *Analyst* **1997**, *122*, 43R-50R.

2. Aswal, D. K.; Lenfant, S.; Guerin, D.; Yakhmi, J. V.; Vuillaume, D. Self Assembled Monolayers on Silicon for Molecular Electronics. *Anal. Chim. Acta* **2006**, *568,*84-108.

3. Wirth, M. J.; Fairbank, R. W. P.; Fatunmbi, H. O. Mixed Self-Assembled Monolayers in Chemical Separations. *Science* **1997**, *44*, 44-47.

4. Curreli, M.; Zhang, R.; Ishikawa, F. N.; Chang, H.-K.; Cote, R. J.; Zhou, C.; Thompson, M. E. Real-Time, Label-Free Detection of Biological Entities Using Nanowire-Based FETs, *IEEE Trans. on Nanotech.* **2008**, *7*, 651-666.

5. Patolsky, F.; Timko, B. P.; Zheng, G.; Lieber, C. M. Nanowire-Based Nanoelectronic Devices in the Life Sciences. *MRS Bull.* **2007**, *32*, 142-149.

6. Makowski, M. S.; Ivanisevic, A. Molecular Analysis of Blood with Micro-/Nanoscale Field-Effect-Transistor Biosensors. *Small* **2011**, *7*, 1863-1875.

7. Wilk, G. D.; Wallace, R. M.; Anthony, J. M. High-K Gate Dielectrics: Current Status and Materials Properties Considerations. *J. Appl. Phys.* **2001**, *89*, 5243-5275.

8. Robertson, J. High Dielectric Constant Gate Oxides for Metal Oxide Si. *Rep. Prog. Phys.* **2006**, *69*, 327-396.

9. Zhang, F.; Srinivasan, M. P. Self-Assembled Molecular Films of Aminosilanes and Their Immobilization Capacities. *Langmuir* **2004**, *20*, 2309-2314.

10. Moore, G. E. Cramming More Components onto Integrated Circuits. *Electronics* **1965,** *38*, 114-117.

11. Nikolaides, M. G.; Rauschenbach, S.; Luber, S.; Buchholtz, K.; Tornow, M.; Abstreiter, C.; Bausch, A. R. "Silicon-on-insulator based thin-film resistor for chemical and biological sensor applications," *Chemphyschem*, **2003**, *4*, 1104-1106.

12. Zhou, W.; Dai, X.; Fu, T.-M.; Xie, C.; Liu, J.; Lieber, C. M. Long Term Stability of Nanowire Nanoelectronics in Physiological Environments. *Nano Lett.* **2014**, *ASAP*.

13. Kharitonov, A. B.; Zyakts, M.; Lichtenstein, A.; Katz, E.; Willner, I. Enzyme monolayer-functionalizaed field-effect transistors for biosensor applications. *Sens. Actu. B*, **2000**, *70*, 222-231.

14. Wang, X.; Chen, Y.; Gibney, K. A.; Erramilli, S.; Mohanty, P. Silicon-based nanochannel glucose sensor. *Appl. Phys. Lett.* **2008**, *92*, 013903.

15. Ma, H.; Acton, O.; Hutchins, D.; Cernetic, N.; Jen, A. K.-Y. Multifunctional phosphonic acid self-assembled monolayers on metal oxides as dielectrics, interface modification layers and semiconductors for low-voltage high-performance organic field-effect transistors. *Phys. Chem. Chem. Phys.* **2012**, *14*, 14110-14126.

16. George, S. M. Atomic Layer Deposition: An Overview, *Chem. Rev.* **2010**, *110*, 111-131.

17. Mutin, P. H.; Guerrero, G.; Vioux, A. Hybrid materials from organophosphorus couling molecules. *J. Mater. Chem.* **2005**, *15*, 3761-3768.

18. Pasternack, R.; M.; Amy, S. R.; Chabal, Y. J. Attachment of 3-(Aminopropyl) triethoxysilane on Silicon Oxide Surfaces: Dependence on Solution Temperature. *Langmuir* **2008**, *24*, 12963-12971.

19. Anderson, A.; Ashurst, W. R. Investigation of the ability of a silica "seed" layer to improve the thermal and aqueous immersion stability of alkylsilane monolayers. *Thin Solid Films*, **2008**, *516*, 7538-7546.

20. Wang, A.; Tang, H.; Cao, T.; Salley, S.; Ng, K. "In vitro stability of organosilane self-assemble monolayers and multilayers," *J. Colloid. Interface Sci,* **2005**, *291*, 438-447.

21. Szczepanski, V.; Vlassiouk, I.; Smirnov, S. Stability of Silane Modifiers on Alumina Nanoporous Membranes. *J. Membr. Sci.* **2006**, *281*, 587-591.

22. Hofer, R.; Textor, M.; Spencer, N. D. Alkyl Phosphate Monolayers, Self-Assembled from Aqueous Solution on Metal Oxide Surfaces. *Langmuir* **2001**, *17*, 4014-4020.

23. Thissen, P.; Valtiner, M.; Grundmeier, G. Stability of Phosphonic Acid Self-Assembled Monolayers on Amorphous and Single-Crystalline Aluminum Oxide Surfaces in Aqueous Solution. *Langmuir* **2009**, *26*, 156-164.

24. Branch, B.; Dubey, M.; Anderson, A. S.; Artyushkova, K.; Baldwin, J. K.; Petsev, D.; Dattelbaum, A. M. Investigating phosphonate monolayer stability on ALD oxide surfaces. *Appl. Surf. Sci.* **2014**, *288*, 98-108.

25. Spori, D.; Venkataraman, N.; Tosatti, S.; Durmaz, F.; Spencer, N.; Zurcher, S. Influence of alkyl chain length on phosphonate self-assembled monolayers. *Langmuir* **2007**, *23*, 8053-8060.

26. Adolphi, B.; Jahne, E.; Busch, G.; Cai, X. Characterization of the Adsorption of ω-(thiophene-3-yl alkyl) Phosphonic Acid on Metal Oxides with AR-XPS. *Anal. Bioanal. Chem.* **2004**, *379*, 646-652.

27. Adden, N.; Gamble, L.; Castner, D.; Hoffmann, A.; Gross, G.; Menzel, H. Phosphonic Acid Monolayers for Binding Bioactive Molecules to Titanium Surfaces. *Langmuir* **2006**, *22*, 8197-8204.

28. Amalric, J.; Mutin, P.; Guerrero, G.; Ponche, A.; Sotto, A.; Lavigne, J. Phosphonate Monolayers Functionalized by Silver Thiolated Species as Antibacterial Nanocoatings on Titanium and Stainless Steel. *J. Mater. Chem.* **2009**, *19*, 141-149.

29. Grabar, K. C.; Freeman, R. G.; Hommer, M. B.; Natan, M. J. Precipitation and Characterization of Au Colloid Monolayers. *Anal. Chem.* **1995**, *67*, 735-743.

30. Keating, C. D.; Musick, M. D.; Keefe, M. H.; Natan, M. J. Kinetics and Thermodynamics of Au Colloid Monolayer Self-Assembly — Undergraduate Experiments in Surface and Nanomaterials Chemistry. *J. Chem. Ed.* **1999**, *76,* 949-955.

31. Sioss, J. A.; Stoermer, R. L.; Sha, M. Y.; Keating, C. D. Silica-Coated, Au/Ag Striped Nanowires for Bioanalysis. *Langmuir*, **2007**, *23*, 11334-11341.

32. DNA Microarry Facility <http://hils.psu.edu/stf/dnama/hybridization.html> Accessed 10/11/12.

33. Ariga, K.; Hill, J. P.; Ji, Q. Layer-by-layer Assembly as a Versatile Bottom-Up Nanofabrication Technique for Exploratory Research and Realistic Application. *Phys. Chem. Chem. Phys.* **2007**, *9*, 2319-2340.

34. Hong, H.-G.; Bohn, P. W.; Sliger, S. G. Optical Determination of Surface Density in Oriented Metalloprotein Nanostrucutres. *Anal. Chem.* **1993**, *65*, 1635-1638.

35. Graber, K. C.; Smith, P. C.; Musick, M. D.; Davis, J. A.; Walter, D. G.; Jackson, M. A.; Guthrie, A. P.; Natan, M. J. Kinetic Control of Interparticle Spacing in Au Colloid-Based Surfaces: Rational Nanometer-Scale Architecture. *J. Am. Chem. Soc.* **1996**, *118*, 1148-1153.

36. Queffélec, C.; Petit, M.; Janvier, P.; Knight, D. A.; Bujoli, B. Surface modification using phosphonic acids and esters. *Chem. Rev.* **2012**, *112*, 3777-3807.

37. Pellerite, M. J.; Dunbar, T. D.; Boardman, L. D.; Wood, E. J. Effects of Fluorination on Self-Assembled Monolayer Formation from Alkanephosphonic Acids on Aluminum: Kinetics and Structure. *J. Chem. Phys. B.* **2003**, *107*, 11726-11736.

38. Lapin, N. A.; Chabel, Y. J. Infrared Characterization of Biotinylated Silicon Oxide Surfaces, Surface Stability, and Specific Attachment of Streptavidin. *J. Phys. Chem. B.* **2009,** *113*, 8776-8783.

# Chapter 3

# Graphene Field Effect Transistor (GFET) Biosensors

<Portions of this material were reproduced in part from Wang, B.*; Liddell, K. L.*; Wang, J.; Koger, B.; Keating, C. D.; Zhu, J. "Oxide-on-graphene field effect biosensors." *Submitted 12/23/13 to Nano Research*>

*These authors contributed equally to this work

The author of this dissertation was responsible for the buffer preparation and surface functionalization and participated in discussions for the design of biosensing experiments in this chapter. Dr. Bei Wang of Dr. Jun Zhu's group from the Department of Physics at Pennsylvania State University was responsible for all device fabrication and execution of sensing experiments. The manuscript was written in collaboration with all authors.

## 3.1 Introduction

Sensors are essential to biomedical diagnosis. Compared to traditional methods such as fluorescence, surface plasmon resonance, and bioassays, sensors based on electrical detection schemes can potentially be faster, more cost effective, and require less specialized equipment. Ion-sensitive field effect transistors (ISFETs), for example, work by converting charge accumulation caused by the binding of biomolecules on a sensing surface into a potential signal, which is then detected by the conductance change of the FET transducer.[1] Such sensors can be readily integrated into a multiplexing system to deliver low-cost, on-chip biomedical diagnosis[2-4], or used to study the hybridization and binding kinetics of DNA and proteins.[5-10]

Until recently, ISFET technology primarily focused on silicon transistors.[1,7,8,11] More recent efforts explore field effect transistors (FETs) based on low-dimensional nanostructures, such as nanowires and carbon nanotubes, because of their size, large

surface-to-volume ratio, and potentially higher sensitivity. Although high performances have been demonstrated[12-15], much work needs to be done to address practical issues, such as uniformity, stability and scalability, before applications can be developed.[16,17] Graphene FETs (GFETs) may be a good candidate for biosensing because of their excellent carrier mobility and the availability of low-cost, large-scale synthetic methods.[18-21] Indeed, several recent studies report using GFETs as a pH sensor[22-25] and for the detection of protein and DNA[23.26,27].

Despite their popularity, the underlying sensing mechanism of GFETs is not clear. Fu et al. demonstrates that a pristine graphene sheet is insensitive to $H^+$ concentration change in solution.[28] This points to the role of uncontrolled extrinsic imperfections, such as defects and contaminations, in the sensing process. These complications require further studies to clarify. In contrast, $SiO_2$ has been widely used in ISFETs made from bulk silicon to nanowires as the dielectric layer and sensing surface because of the well-established silanization chemistry that enables the immobilization of specific bioprobes and targets.[29] The ion sensitivity of a $SiO_2$ surface is well understood by the site dissociation model, which describes the electrostatic potential at electrolyte oxide interfaces.[30,31]

This chapter describes characterization and biosensing experiments of a novel oxide-on-graphene biosensor. The graphene channel was passivated by a $SiO_2/HfO_2$ (25 nm/20 nm) double oxide layer, which used the top $SiO_2$ layer as the sensing/immobilization surface and the high-quality $HfO_2$ layer protected the channel from solution (Figure 3-1). Bare and 3-aminopropyltrimethoxysilane (APTMS)-functionalized devices were sensitive to the pH value of phosphate buffer saline (PBS) solution ranging from 4-9.

Furthermore, APTMS-functionalized devices provided a pathway to examine device response to immobilized biotin/avidin. These new devices represent an exciting new class of sensors that combines the biosensing capabilities of graphene with the well-known and controllable chemistries of silica.

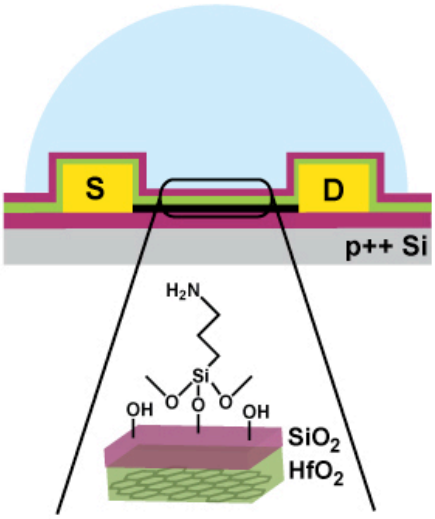


**Figure 3-1** Cartoon of oxide-on-graphene FET with APTMS-functionalized $SiO_2$.

## 3.2 Experimental Materials and Methods

### 3.2.1 Materials

APTMS was obtained from TCI America. Ethanol (EtOH, 200 proof) was supplied by Koptec. EZ-Link® NHS-LC-Biotin and avidin from hen egg white were purchased from Pierce Protein Research Products, Thermo Scientific. Buffers, salts, and general chemicals were purchased from Sigma-Aldrich. All water used was either 18.2 MΩ-cm Nanopure water from a Barnstead system or EMD Chemicals HPLC grade water. All reagents were used without further purification.

### 3.2.2 Buffer Preparation

The pH sensing study used 0.010 M PBS, denoted as sensing buffer (0.001 M sodium phosphate and 0.010 M potassium chloride, pH 4.1, 6.0, 6.9, or 8.8) prepared with HPLC grade water.

Surface functionalization with NHS-LC-Biotin used 0.010 M PBS, denoted as reaction PBS, (0.010 M sodium phosphate and 0.3 M sodium chloride, pH 7.4) prepared with HPLC grade water.

### 3.2.3 GFET Fabrication

Graphene sheets were synthesized by low-pressure chemical vapor deposition (CVD) on copper foil and transferred to 290 nm $SiO_2$/highly doped Si substrates using a polymer-assisted wet transfer method.[18] The transferred sheet was annealed in $Ar/H_2$ at 450°C for 2 hours.

Two-terminal graphene FETs of dimensions 2 μm (width) × 4 μm (length) were fabricated using optical lithography, reactive ion etching, and metal deposition. $HfO_2$ (20 nm) was deposited on the whole wafer using atomic layer deposition and recipes previously established by Dr. Zhu's group[24] followed by the electron beam evaporation of 25 nm of $SiO_2$.

### 3.2.4 XPS Characterization of APTMS and Biotin Modified $SiO_2$

$SiO_2$-coated wafer pieces (from regions on the GFET wafer where devices were not located) roughly 2 cm × 2 cm were functionalized in 20 mL glass vials containing 3%

APTMS in 200 proof ethanol for 1 hour. Excess APTMS was removed with an ethanol rinse followed by a 10 minute cure at 110°C.

Some samples were subsequently modified with biotin in 20 mL glass vials containing reaction PBS and 2 mg/mL NHS-LC-Biotin for 1 hour. Chips were rinsed thoroughly with DI water and dried with $N_2$ prior to measurement.

X-ray photoelectron spectra were acquired with a Kratos Analytical Axis Ultra spectrometer using a monochromatic Al K$\alpha$ X-ray source. High-resolution scans were acquired at a pass energy of 20 eV, with a 0.1 eV scan step size and analyzed with CasaXPS software.

### 3.2.5 pH Detection with Bare and APTMS-Modified GFETs

Prior to measurement, some GFETs were functionalized with APTMS by a similar procedure as described for XPS samples. pH sensing measurements of bare or APTMS-modified GFETs were performed by covering the device channel area with a droplet of sensing buffer of the desired pH, avoiding contact between the liquid and the electrodes. A silicone ring was sometimes used to confine the droplet. Transfer curves were obtained at each pH value over the course of ~ 20 minutes. After each pH measurement, the chip was thoroughly rinsed in DI water followed by the sensing buffer of the next desired pH value before the next set of measurements began.

### 3.2.6 GFET Detection of Biotin/Avidin Chemistry

GFET devices were functionalized and measured with the same procedure as described previously except pH ~ 7 sensing buffer was used exclusively. Transfer curves were

obtained before functionalized (bare) and after each functionalization step (APTMS, biotinylation, avidin). For reaction with avidin, the chip was rinsed thoroughly in water then added to a solution of 1 mg/mL avidin in sensing buffer for 1 hour. The chip was thoroughly rinsed with water and final transfer curve was measured.

## 3.3 Results and Discussion

### 3.3.1 Oxide-on-Graphene FET Operation in Solution

Figure 3-2 shows a schematic of the oxide-on-graphene sensor operation in solution, with both the doped silicon back gate and the solution top gate. A small droplet of deionized water or PBS solution formed the solution gate above the channel area. Care was taken to ensure that the droplet did not cover the contact pads of the device being measured. A tungsten electrode and an Ag/AgCl reference electrode were inserted into the droplet to apply $V_{app}$ and read the potential of the solution, $V_{sg}$, respectively. The use of the reference electrode was necessary to eliminate spurious changes in the characteristics of the sensor due to the variation of the potential drop at the tungsten/solution interface. Because of the conformal growth of the $HfO_2$ film, the channel was well protected from the solution and the solution gate operated with a small leakage current of less than 100 pA.

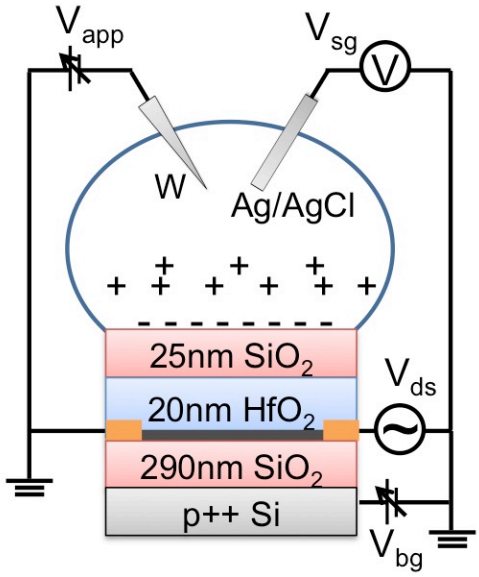


**Figure 3-2** Schematic drawing of the oxide-on-graphene FET operating in solution. The solution gate voltage is applied through a tungsten electrode and read by an Ag/AgCl reference electrode.

A common problem in field effect devices made from nanomaterials, such as nanotubes, nanowires, and graphene, is hysteretic transfer curves caused by interfacial changes and adsorbates.[13,23,32] Adoption of pulsed gate sweep techniques (Figure 3-3, B) applied to carbon nanotube FETs[33,34], enabled suppression of hysteresis in our graphene FETs completely. Examples of hysteretic and hysteresis-free $G(V_{sg})$ traces of the same device are shown in Figure 3-3, A. The elimination of hysteresis eliminated a source of uncertainty in the operation of nanostructured sensors and greatly improved their long-term stability.

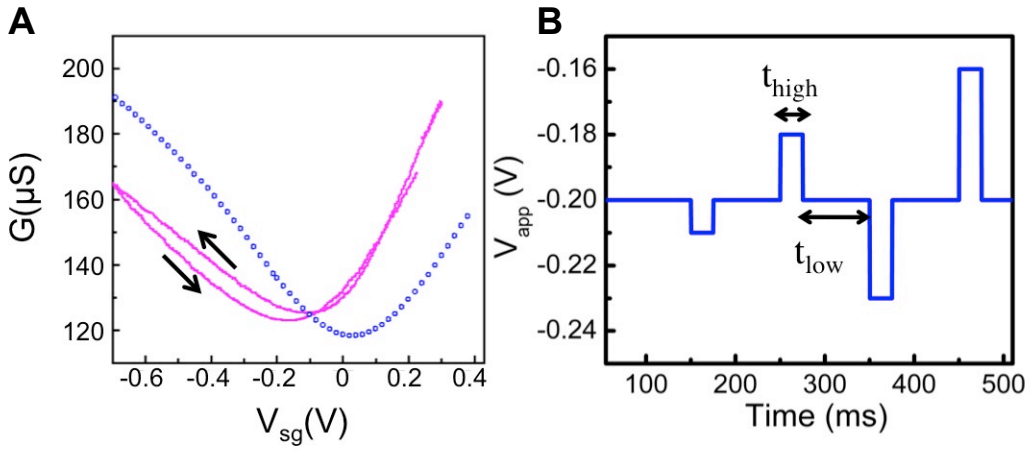


**Figure 3-3** (A) The conductance of a graphene channel vs. the solution gate voltage $V_{sg}$ with $V_{sg}$ changed continuously (solid magenta traces) and in pulse (blue hollow circles). The arrows indicate the sweeping directions of the magenta traces. The time-varying pattern of the $V_{app}$ pulse is shown in (B) $t_{high}$ = 25 ms, $t_{low}$ = 75 ms

### 3.3.2 pH Sensing Measurements

Next we demonstrated the proof-of-principle operation of the oxide-on-graphene sensor by measuring its response to the pH of PBS solutions. Both bare $SiO_2$ and APTMS-functionalized devices were tested and their sensing performance evaluated in Figures 3-4 and 3-5. The pH response of a bare FET is shown in Figure 3-4, A. As the pH value of the PBS solution increased, the $G(V_{sg})$ curve retained its shape but shifted toward positive $V_{sg}$. In Figure 3-4, B the bottom of the "V" shape where the channel current reaches its minimum is the measured Dirac point, $V_D$, which is plotted versus pH. The error bars represent the spread of $V_D$ from repeated measurements over the course of 6 hours. Measurements were reproducible after weeks, which demonstrated excellent stability of the sensors. In the range of pH = 4.1 to 8.8, $V_D$ (pH) is well described by a linear fit, with a slope of 43 mV/pH. Upon averaging many devices, we obtained a voltage sensitivity of (46 ± 8) mV/pH. These results were in good agreement with

literature results and are well understood by the site-dissociation model developed for oxides as described previously.[1,30,31] Briefly, the pH of the solution affects the protonation and deprotonation of hydroxyl groups on the oxide surface, leading to a change in the potential drop $\psi_0$ at the solution/oxide interface, which causes the $G(V_{sg})$ curve to shift. In the case of $SiO_2$, increasing pH increases the presence of negative charges on the $SiO_2$ surface, which results in a larger $\psi_0$, and a shift in $G(V_{sg})$ towards positive $V_{sg}$. This is exactly what we observed. In the linear regime of $G(V_{sg})$ in Figure 3-4, B, the conductance changes by 4.2 μS/pH. This is a large change and can be further increased by reducing the oxide thickness (presently 45 nm) and increasing carrier mobility (presently 5000 $cm^2/Vs$).

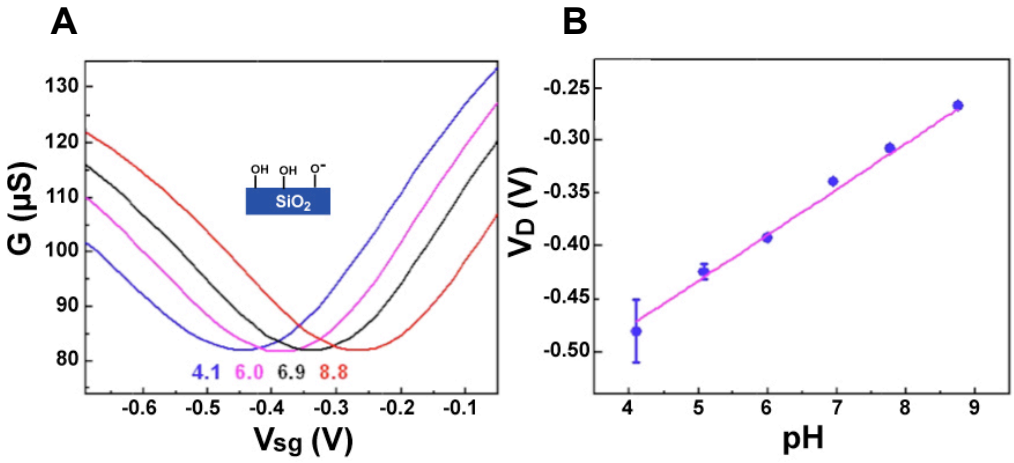


**Figure 3-4** (A) Conductance (G) versus solution gate ($V_{sg}$) of bare oxide-on-graphene FET in response to solutions of PBS at different pH values. From left to right: pH = 4.1 (blue), 6.0 (pink), 6.9 (black), 8.8 (red). (B) Plot of Dirac point voltage ($V_D$) as a function of solution pH.

Similar to the bare oxide-on-graphene devices, $G(V_{sg})$ of APTMS-functionalized devices shifted towards positive $V_{sg}$ with increasing pH (Figure 3-5, A). The pH-dependent Dirac point ($V_D$) of this device is shown in Figure 3-5, B from which a slope of 28 mV/pH was extracted. Averaging many devices, we found the pH sensitivity of APTMS-functionalized GFETs to be (34 ± 8) mV/pH. These results agree well with previous studies.[35] The reduced pH sensitivity was expected, as the amine group is less amphoteric than the Si-OH group, and the coverage of the APTMS layer was also probably less dense than that of hydroxyl groups on $SiO_2$.

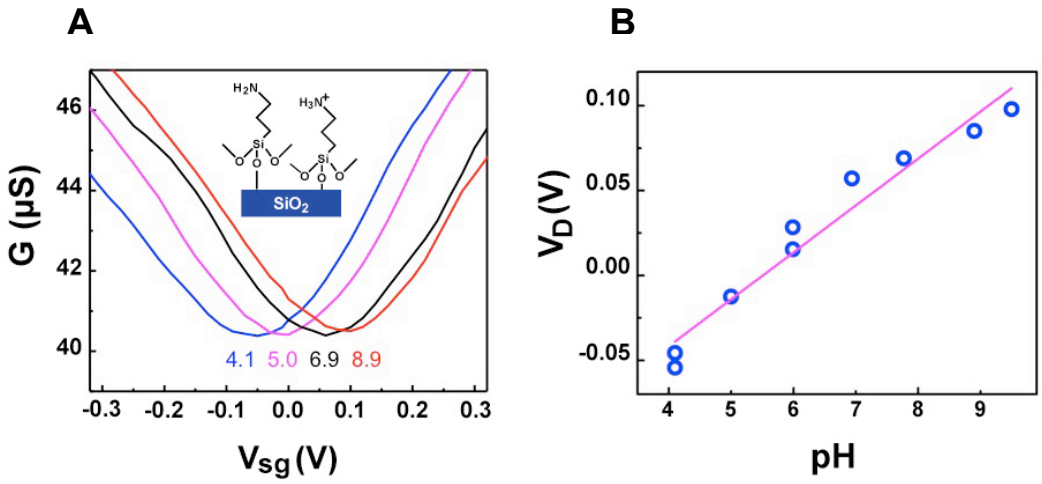


**Figure 3-5** (A) Conductance (G) versus solution gate ($V_{sg}$) of bare oxide-on-graphene FET in response to solutions of PBS at different pH values. From left to right: pH = 4.1 (blue), 6.0 (pink), 6.9 (black), 8.8 (red). (B) Plot of Dirac point voltage ($V_D$) as a function of solution pH.

### 3.3.3 Characterization of Surface Functionalization of $SiO_2$ with APTMS and Biotin

Prior to device measurements for biomolecule sensing, surface chemistry functionalization was validated with X-ray photoelectron spectroscopy (XPS). As

previously mentioned, silanization of $SiO_2$ provides a convenient pathway to covalently attach bioprobes. In this case, after modification with APTMS, surfaces were incubated with a sulfo-NHS-activated biotin, which readily reacts with primary amines to form stable, covalent amide bonds under mildly-basic conditions (Figure 3-6, A).[36] In Figures 3-6, B-D high-resolution XPS spectra of the N 1s, C 1s, and S 2p states on bare $SiO_2$ (black), or after APTMS (red) and biotin (blue) functionalization are shown. The N 1s spectrum for APTMS and biotinylated surfaces exhibited a prominent peak at 397 eV, whereas no such signal was detected on the bare $SiO_2$ surface. In addition, the APTMS surface has a secondary peak observed at 399 eV. These peaks correspond to $NH_2$ and $NH_3^+$ groups, respectively, with the latter due to the presence of water.[37] In the C 1s spectrum, all three surfaces had a signal near 282.5 eV due to $sp^3$-bonded carbon atoms. This can be expected to a small extent on all surfaces due to adventitious carbon contamination[38]; however, significantly higher amounts were found on APTMS and biotinylated surfaces, a phenomenon that indicated our intended molecules were present. To further support this, a secondary peak at 285.5 eV was present due to $sp^2$-bonded carbon, and a small sulfur peak at 161 eV was observed in the S 2p spectrum only on biotinylated surfaces.[38]

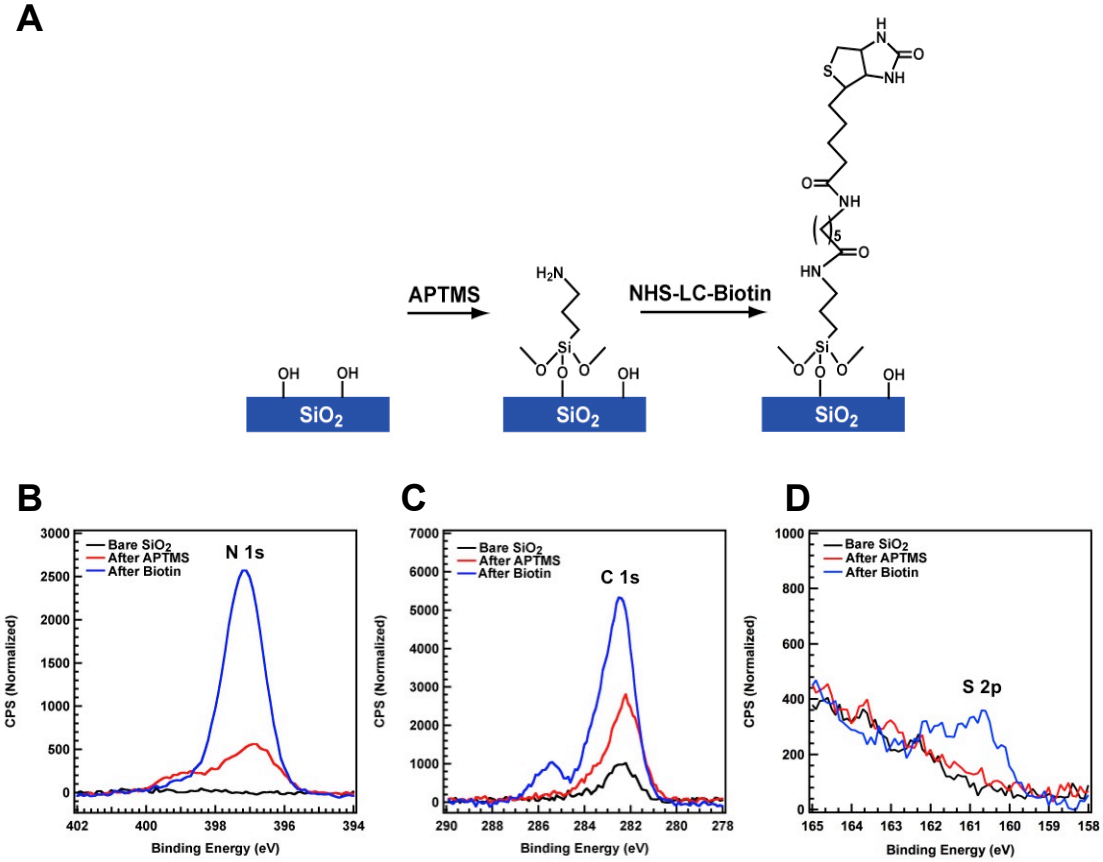


**Figure 3-6** (A) Cartoon of surface chemistry on $SiO_2$-coated Si wafer after reaction with APTMS and NHS-LC-Biotin. High resolution XPS spectra of (B) N 1s, (C) C 1s, and (D) S 2p orbitals were measured from surfaces of bare $SiO_2$ (red), and after APTMS (green) and NHS-LC-Biotin (blue) functionalization.

Biotin is a neutral, small molecule often used as an immobilized probe for biomolecule detection with charge-based sensors. It has a high binding constant, ~ $10^{-13}$-$10^{-15}$ $M^{-1}$, which results in tight binding affinity for a class of avidin-based proteins that have different net charges at neutral pH.[39] We chose to use avidin for biosensing studies as opposed to neutravidin or streptavidin because it has an isoelectric point of 10.5 and is

thus negatively charged at neutral pH.[40] This would provide a stark contrast to the positively charged surface created by APTMS. After functionalization of devices, conductance (G) versus gate voltage ($V_{sg}$) was measured with bare $SiO_2$ and after reaction with APTMS, biotin, and avidin. A left shift in Dirac point was expected for positively charged APTMS surfaces and indeed was observed. Reaction with biotin was expected to remove a large percentage of the surface charge and thus shift the Dirac point closer to the bare oxide, and bound avidin should have shifted the Dirac point to the right due to negatively charged residues on the protein surface. Significant hysteresis in the measurement due to pulse-gate techniques not used during this experiment complicated interpretation. It was clear the device was responding to something on the surface; however, further work is required to realize biomolecule detection.

### 3.4 Conclusions

We have designed, fabricated and demonstrated the operation of a novel high-quality, oxide-on-graphene field effect biosensor array in solution. A thin oxide film as the sensing layer preserved the high mobility of the graphene transducer and enabled sensing specificity. The GFETs functioned stably and reproducibly. As a proof of principle, we have shown that bare and APTMS-functionalized $SiO_2$ surfaces responded to the pH of PBS solutions, with the sensitivity of 46 mV/pH and 34 mV/pH respectively. This work opens the door to using graphene-based electrical devices to selectively detect the presence and binding events of molecules of interest.

### 3.5 References


1. Bergveld, P. Thirty Years of ISFETOLOGY: What Happened in the Past 30 Years and What May Happen in the Next 30 Years. *Sens. Actu. B: Chem.* **2003**, *88*, 1-20.
2. Johannessen, E. A.; Wang, L.; Cui, L.; Tang, T. B.; Ahmadian, M.; Astaras, A.; Reid, S. W. J.; Murray, A. F.; Flynn, B. W.; Beaumont, S. P.; Cumming, D. R. S.; Cooper, J. M. Implementation of Multichannel Sensors for Remote Biomedical Measurements in a Microsystems Format. *IEEE Trans. Biomed. Eng*. **2004**, *51*, 525-535.
3. Zhang, G. J.; Ning, Y. Silicon Nanowire Biosensor and its Applications in Disease Diagnostics: A Review. *Anal. Chim. Acta* **2012**, *749*, 1-15.
4. Patolsky, F.;Zheng, G.; Lieber, C. Nanowire-Based Biosensors. *Anal. Chem.* **2006**, *78*, 4260-4269.
5. Poghossian, A.; Cherstvy, A.; Ingebrandt, S.; Offenhausser, A.; Schoning, M. J. Possibilities and Limitations of Label-Free Detection of DNA Hybridization with Field-Effect-Based Devices. *Sens. Actu. B: Chem.* **2005**, *111*, 470-480.
6. Bunimovich, Y. L.; Shin, Y. S.; Yeo, W. S.; Amori, M.; Kwong, G.; Heath, J. R. Quantitative Real-Time Measurements of DNA Hybridization with Alkylated Nonoxidized Silicon Nanowires in Electrolyte Solution. *J. Amer. Chem. Soc.* **2006**, *128*, 16323-16331.
7. Gonçalves, D.; Prazeres, D.; Chu, V.; Conde, J. Detection of DNA and Proteins Using Amorphous Silicon Ion-Sensitive Thin-Film Field Effect Transistors. *Biosens. Bioelectron.* **2008**, *24*, 545-551.

8. Rothberg, J. M.; Hinz, W.; Rearick, T. M.; Schultz, J.; Mileski, W.; Davey, M.; Leamon, J. H.; Johnson, K.; Milgrew, M. J.; Edwards, M.; Hoon, J.; Simons, J. F.; Marran, D.; Myers, J. W.; Davidson, J. F.; Branting, A.; Nobile, J. R.; Puc, B. P.; Light, D.; Clark, T. A.; Huber, M.; Branciforte, J. T.; Stoner, I. B.; Cawley, S. E.; Lyons, M.; Fu, Y. T.; Homer, N.; Sedova, M.; Miao, X.; Reed, B.; Sabina, J.; Feierstein, E.; Schorn, M.; Alanjary, M.; Dimalanta, E.; Dressman, D.; Kasinskas, R.; Sokolsky, T.; Fidanza, J. A.; Namsaraev, E.; McKernan, K. J.; Williams, A.; Roth, G. T.; Bustillo, J. An Integrated Semiconductor Device Enabling Non-Optical Genome Sequencing. *Nature* **2011**, *475*, 348-352.
9. Sorgenfrei, S.; Chiu, C.; Gonzalez Jr, R. L.; Yu, Y. J.; Kim, P.; Nuckolls, C.; Shepard, K. L. Label-Free Single-Molecule Detection of DNA-Hybridization Kinetics with a Carbon Nanotube Field-Effect Transistor. *Nature Nanotech.* **2011**, *6*, 126.
10. Stern, E.; Klemic, J. F.; Routenberg, D. A.; Wyrembak, P. N.; Turner-Evans, D. B.; Hamilton, A. D.; LaVan, D. A.; Fahmy, T. M.; Reed, M. A. Label-Free Immunodetection with CMOS-Compatible Semiconducting Nanowires. *Nature* **2007**, *445*, 519-522.
11. Bausells, J.; Carrabina, J.; Errachid, A.; Merlos, A. Ion-Sensitive Field-Effect Transistors Fabricated in a Commercial CMOS Technology. *Sens. Actu. B: Chem.* **1999**, *57*, 56-62.
12. Cui, Y.; Wei, Q.; Park, H.; Lieber, C. M. Nanowire Nanosensors for Highly Sensitive and Selective Detection of Biological and Chemical Species. *Science* **2001**, *293*, 1289-1292.

13. Allen, B. L.; Kichambare, P. D.; Star, A. Carbon Nanotube Field-Effect-Transistor-Based Biosensors. *Adv. Mater*. **2007**, *19*, 1439-1451.

14. He, B.; Morrow, T.; Keating, C. Nanowire Sensors for Multiplexed Detection of Biomolecules. *Curr. Opin. Chem. Biol.* **2008**, *12*, 522-528.

15. Roy, S.; Gao, Z. Q. Nanostructure-Based Electrical Biosensors. Nano Today **2009**, *4*, 318-334.

16. Regonda, S.; Tian, R. H.; Gao, J. M.; Greene, S.; Ding, J. H.; Hu, W. Silicon Multi-Nanochannel FETs to Improve Device Uniformity/Stability and Femtomolar Detection of Insulin in Serum. *Biosens. Bioelectron.* **2013**, *45*, 245-251.

17. Tian, R. H.; Regonda, S.; Gao, J. M.; Liu, Y. L.; Hu, W. Ultrasensitive Protein Detection Using Lithographically Defined Si Multi-Nanowire Field Effect Transistors. *Lab on a Chip* **2011**, *11*, 1952-1961.

18. Li, X. S.; Cai, W. W.; An, J. H.; Kim, S.; Nah, J.; Yang, D. X.; Piner, R.; Velamakanni, A.; Jung, I.; Tutuc, E.; Banerjee, S. K.; Colombo, L.; Ruoff, R. S. Large-Area Synthesis of High-Quality and Uniform Graphene Films on Copper Foils. *Science* **2009**, *324*, 1312-1314.

19. Shao, Y. Y.; Wang, J.; Wu, H.; Liu, J.; Aksay, I. A.; Lin, Y. H. Graphene Based Electrochemical Sensors and Biosensors: A Review. *Electroanalysis* **2010**, *22*, 1027-1036.

20. Pumera, M.; Ambrosi, A.; Bonanni, A.; Chng, E. L. K.; Poh, H. L. Graphene for Electrochemical Sensing and Biosensing. *Trends Anal. Chem.* **2010**, *29*, 954-965.

21. Mattevi, C.; Kim, H.; Chhowalla, M. A Review of Chemical Vapour Deposition of Graphene on Copper. *J. Mater. Chem.* **2011**, *21*, 3324-3334.

22. Ang, P. K.; Chen, W.; Wee, A. T. S.; Loh, K. P. Solution-Gated Epitaxial Graphene as pH Sensor. *J. Amer. Chem. Soc.* **2008**, *130*, 14392-14393.

23. Ohno, Y.; Maehashi, K.; Yamashiro, Y.; Matsumoto, K. Electrolyte-Gated Graphene Field-Effect Transistors for Detecting pH Protein Adsorption. *Nano Lett.* **2009**, *9*, 3318-3322.

24. Cheng, Z. G.; Li, Q.; Li, Z. J.; Zhou, Q. Y.; Fang, Y. Suspended Graphene Sensors with Improved Signal and Reduced Noise. *Nano Lett*. **2010**, *10*, 1864-1868.

25. Giacchetti, B. M.; Hsu, A.; Wang, H.; Kim, K. K.; Kong, J.; Palacios, T. CVD-Grown Graphene Solution-Gated Field Effect Transistors for pH Sensing. *MRS Proc.* **2011**, *1283*, mrsf10-1283-b1203-1207.

26. Dong, X. C.; Shi, Y. M.; Huang, W.; Chen, P.; Li, L. J. Electrical Detection of DNA Hybridization with Single-Base Specificity Using Transistors Based on CVD-Grown Graphene Sheets. *Adv. Mater.* **2010**, *22*, 1649-1653.

27. Ang, P. K.; Jaiswal, M.; Lim, C.; Wang, Y.; Sankaran, J.; Li, A.; Lim, C. T.; Wohland, T.; Ozyilmaz, B.; Loh, K. P. A Bioelectronic Platform Using a Graphene-Lipid Bilayer Interface. *ACS Nano* **2010**, *4*, 7387-7394.

28. Fu, W.; Nef, C.; Knopfmacher, O.; Tarasov, A.; Weiss, M.; Calame, M.; Schonenberger, C. Graphene Transistors Are Insensitive to pH Changes in Solution. *Nano Lett.* **2012**, *11*, 3597-3600.

29. Pividori, M. I.;Merkoci, A.; Alegret, S. Electrochemical Genosensor Design: Immobilization of Oligonucleotides onto Transducer Surfaces and Detection Methods. *Biosens. Bioelectron.* **2000**, *15*, 291-303.

30. Akiyama, T.; Ujihira, Y.; Okabe, Y.; Sugano, T.; Niki, E. Ion-Sensitive Field-Effect Transistors with Inorganic Gate Oxide for pH Sensing. IEEE Trans. Elec. Dev. **1982**, *29*, 1936-1941.

31. Van Hal, R.; Eijkel, J.; Bergveld, P. A General Model to Describe the Electrostatic Potential at Electrolyte Oxide Interfaces. Adv. Coll. Interf. Sci. **1996**, *69*, 31-62.

32. Wang, H.; Wu, Y.; Cong, C.; Shang, J.; Yu, T. Hysteresis of Electronic Transport in Graphene Transistors. *ACS Nano* **2012**, *4*, 7221-7228.

33. Mattmann, M.; Roman, C.; Helbling, T.; Bechstein, D.; Durrer, L.; Pohle, R.; Fleischer, M.; Hierold, C. Pulsed Gate Sweep Strategies for Hysteresis Reduction in Carbon Nanotube Transistors for Low Concentration $NO_2$ Gas Detection. *Nanotechnology* **2010**, *21*, 185501.

34. Estrada, D.; Dutta, S.; Liao, A.; Pop, E. Reduction of Hysteresis for Carbon Nanotube Mobility Measurements Using Pulsed Characterization. *Nanotechnology* **2010**, *21*, 085702.

35. Khamaisi, B.; Vaknin, O.; Shaya, O.; Ashkenasy, N. Electrical Performance of Silicon-On-Insulator Field-Effect Transistors with Multiple Top-Gate Organic Layers in Electrolyte Solution. *ACS Nano* **2010**, *4*, 4601-4608.

36. *Bioconjugate Techniques*; Hermanson, G. T. 2nd Ed. Elsevier: London, 2008; pp 506-515.

37. Chauhan, A. K.; Aswal, D. K.; Koiry, S. P.; Gupta, S. K.; Yakhmi, J. V.; Surgers, C.; Guerin, D.; Lenfant, S.; Vuillaume, D. Self-Sssembly of the 3-Aminopropyltrimethoxysilane Multilayers on Si and Hysteretic Current-Voltage Characteristics. *Appl. Phys. A-Mater. Sci. Process*. **2008**, *90*, 581-589.

38. *Practical Surface Analysis*; Briggs, D.; Seah, M. P., Eds.; 2nd Ed. Wiley: New York, 1990.

39. Green, N. M. Avidin. I. The Use of Biotin-14C for Kinetic Studies and for Assay, *Biochem. J.* **1963**, *89*, 585-591.

40. Green, N. M. Avidin, *Adv. Protein Chem.* **1975**, *29*, 85-133.

# Chapter 4

# Investigations of Si Nanowire Field Effect Transistor Response to pH Changes and Biomolecules

The author of this dissertation was responsible for the low ionic strength buffer preparation and surface functionalization. Xiahua Zhong of Dr. Theresa Mayer's group from the Department of Electrical Engineering at Pennsylvania State University was responsible for all device fabrication and execution of pH sensing experiments. The author of this dissertation and Xiahua Zhong provided equal contribution to the experimental design, execution, and interpretation of biosensing experiments.

## 4.1 Introduction

For more than a decade, Si nanowire (NW) field effect transistors (FETs) have been used as sensors for a range of applications including pH-sensing[1,2], gas detection[3,4], and biosensing[5-7]. Tremendous success in the detection of nucleic acids and proteins has been achieved. For example, highly sensitive and selective detection of target DNA has been shown with Si NW FETs including a limit of detection (LOD) of 0.1 fM target and single nucleotide base discrimination with 10 nM target.[7] Furthermore, Lieber and coworkers demonstrated detection of prostate specific antigen (PSA), a protein cancer marker, at a level of ~2 fM in serum.[8] For comparison, a detection limit of 3 pM in serum has been reported by a leading commercial PSA assay (ADVIA Centaur, Siemens).[9]

Despite extensive work in this area, commercialization of such devices has been limited[10,11] and significant challenges remain due to variability in device performance and need for individual sensor calibration.[12,13] Furthermore, a lack of established optimal measurement conditions such as buffer/solution composition, analyte delivery method, and even use of a reference electrode complicate improvement in this field.[14]

The goal of this project was to address and understand many of the current challenges in the Si NW FET literature. Validation of surface chemistry, device performance, and measurement protocols was accomplished on the way to this goal. This chapter describes the validation of surface chemistry on model surfaces. After which electrical and pH response from Si NW FETs is shown. Lastly, devices were functionalized with biomolecule receptors and the device response to solutions of analyte was measured.

## 4.2 Experimental Materials and Methods

### 4.2.1 Materials

Anodisc™ aluminum oxide membranes with a nominal pore size of 0.2 μm were purchased from Whatman. Orotemp 24 and Ag Cyless R plating solutions were obtained from Technic Inc. Tetraethoxysilane (TEOS) was purchased from Gelest. 3-aminopropyltrimethoxysilane (APTMS) was obtained from TCI America. N-cyclohexyl-2-aminoethanesulfonic acid (CHES), buffers, salts, and general chemicals were purchased from Sigma-Aldrich. EZ-Link® NHS-LC-Biotin, Sulfosuccinimidyl 6-(3'-[2-pyridyldithio]-propionamido)hexanoate (Sulfo-LC-SPDP), succinimidyl 2-(biotinamido)-ethyl-1,3'–dithiopropionate (NHS-SS-Biotin), and avidin from hen egg white were purchased from Pierce Protein Research Products, Thermo Scientific. Alexa Fluor® 488 streptavidin was obtained from Molecular Probes®, Life Technologies. DNA oligonucleotides were purchased from Integrated DNA Technologies Inc. Peptide nucleic acid (PNA) oligonucleotides were obtained from Bio-Synthesis Inc. A “solubility enhancer” was added to PNA oligonucleotides on the N-terminus (Figure 4-1). Ethanol (EtOH, 200 proof) was supplied by Koptec. All water used was either 18.2 MΩ:cm

Nanopure water from a Barnstead system or EMD Chemicals HPLC grade water. Buffer used for surface functionalization, reaction PBS, was prepared with EMD Chemicals HPLC grade water and contained 10 mM sodium phosphate and 300 mM sodium chloride at pH 7.4. All reagents were purchased without further purification; TEOS was aliquoted out in a glove box under $N_2$ to prevent hydrolysis.

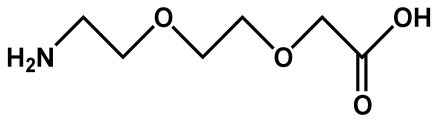


**Figure 4-1** Structure of a solubility enhancer, "O-linker", used to increase water solubility of PNA oligonucleotides.

**Table 4-1**: DNA and PNA probe and target sequences

| Name | Sequence 5′→ 3′<br>For PNA N-Terminus → C-Terminus | Description |
|---|---|---|
| Flu A DNA probe | Thiol-TTTTTTTTTTGACCAATCCTGTCAC | Influenza A DNA probe |
| Flu B DNA probe | Thiol-TTTTTTTTTTTTCTTTTTTGTTGCT | Influenza B DNA probe |
| Flu A PNA probe | Cys-OO-AATCCTGTCAC | Influenza A PNA probe |
| Flu B PNA probe | Cys-OO-TTTTTGTTGCT | Influenza B PNA probe |
| A647 Flu A DNA target | Alexa Fluor 647-GTGACAGGATT | Alexa647 Influenza A DNA target |
| A647 Flu B DNA target | Alexa Fluor 647-AGCAACAAAAA | Alexa647 Influenza B DNA target |
| Flu A DNA target | GTGACAGGATT | Influenza A DNA target |
| Flu B DNA target | AGCAACAAAAA | Influenza B DNA target |
| T3 | CTGTGATGACATGAGGCAGCTTTTTGAC GAGAAAATCTTGATGGC | Target sequence that is non-complementary to all probe sequences used |

O = Solubility enhancer

### 4.2.2 Nanowire Synthesis

Metal nanowires were synthesized by galvanostatic electrodeposition into aluminum oxide templates as described previously.[15-18] Briefly, silver (300 nm) was evaporated on one side of membrane to act as the working electrode. Nanowires were electrodeposited into the alumina template pores and subsequently released by dissolving the silver backing and template with 33% v/v nitric acid and 3 M NaOH, respectively. Wires were rinsed twice with water and twice with EtOH before suspension in 1 mL EtOH at a concentration of ~$10^9$ wires/mL.[19]

### 4.2.3 Silica Coating of Nanowires

Nanowires were coated with ~20-30 nm $SiO_2$ using TEOS as previously described.[20,21] Briefly, 300 μL nanowires at the batch concentration in EtOH are combined with 160 μL water, 10 μL $NH_4OH$, 490 μL EtOH, and 40 μL TEOS in a 1.7 mL microcentrifuge tube and sonicated for 1 hour. After sonication, $SiO_2$-coated nanowires were rinsed three times with EtOH and resuspended in 900 μL EtOH. Transmission electron microscopy (TEM) images of nanowires were obtained with a JEOL JEM 1200 EXII instrument.

### 4.2.4 DNA and PNA Preparation

DNA and PNA arrived as a lyophilized pellet from Integrated DNA Technologies, Inc. or Bio-Synthesis Inc., respectively. Prior to use, fluorescently-labeled DNA, amine-terminated DNA, unmodified DNA, or PNA oligonucleotides were rehydrated in 18.2 MΩ:cm Nanopure water. Thiol-terminated DNA was rehydrated in a 100 mM solution of DL-dithiothreitol in 10 mM sodium phosphate buffer at pH 8.3 to cleave any disulfide

bridges present. After 1 hour the solution was desalted with a Princeton Separations (Adelphia, NJ) Centrispin 10 column, resulting in a solution of individual thiol-terminated DNA oligonucleotides.[22]

The sequence concentration of DNA or PNA was determined by measuring the solution absorbance at 260 nm using a Hewlett-Packard 8453 diode-array UV/visible spectrometer with Agilent ChemStation software. Sequences were diluted to either 100 μM or 20 μM and stored at -80°C.

### 4.2.5 Biofunctionalization of $SiO_2$-Coated Nanowires

Silica-coated metal nanowires were reacted with APTMS and a bifunctional crosslinker to enable covalent attachment of probe molecules by similar methods described previously.[22] Briefly, 300 μL $SiO_2$-coated metal nanowires, at batch concentration, were transferred to a 1.7 mL non-stick microcentrifuge tube, and EtOH was removed by centrifugation. Wires were vortexed in 500 μL 3% APTMS in 200 proof EtOH for 30 minutes then rinsed by centrifugation and resuspension once with EtOH and twice with either reaction PBS or CHES buffer. Wires were vortexed for 1-2 hours in 2 mg/mL bifunctional crosslinker in 1 mL reaction PBS (NHS-LC-Biotin or Sulfo-LC-SPDP) or CHES buffer (Sulfo-SMCC). Biotinylated samples required 3 rinse steps in reaction PBS to complete surface functionalization. DNA or PNA samples were rinsed 3 times in reaction PBS; wires were evenly split between two, 0.5 mL non-stick centrifuge tubes to which 1 μM complementary or non-complementary probe DNA or PNA (diluted from 20 μM stock) was added. Wires were vortexed for 1 hour and DNA or PNA surface functionalization was completed after 3 rinse steps with reaction PBS.

### 4.2.6 Detection of Streptavidin with Biotinylated Nanowires

Biotinylated nanowires as described previously with NHS-LC-Biotin were transferred to a 0.5 mL non-stick centrifuge tube. An additional 0.5 mL non-stick centrifuge tube contained nanowires functionalized with APTMS only (No biotin). Both tubes were vortexed in 4 nM Alexa Fluor® 488 labeled streptavidin in 1 mL water for 2 hours. Wires were protected from light throughout the experiment by wrapping in Al foil.

### 4.2.7 Optical and Fluorescence Microscopy

Reflectance and fluorescence images of nanowires were obtained using Image-Pro Plus software with a Nikon TE-300 inverted microscope equipped with a Xe arc lamp and Photometrics Coolsnap HQ camera. A Plan Apo 60x oil or Nikon Plan Fluor 100x oil objective was used. Samples were prepared by placing a 10 μL DI suspension of nanowires onto a glass slide with a coverslip. NBSee software was used to quantify nanowire fluorescence.

### 4.2.8 Fabrication of Si NW FETs

Si NW FETs were synthesized by top-down lithographic methods as previously described in the literature.[23] Briefly, spatially doped silicon-on-insulator (SOI) wafer was used to fabricate n-p-n doped Si NWs with Ti metal contacts. A thermally grown $SiO_2$ gate dielectric passivated the chip surface (Figure 4-2).

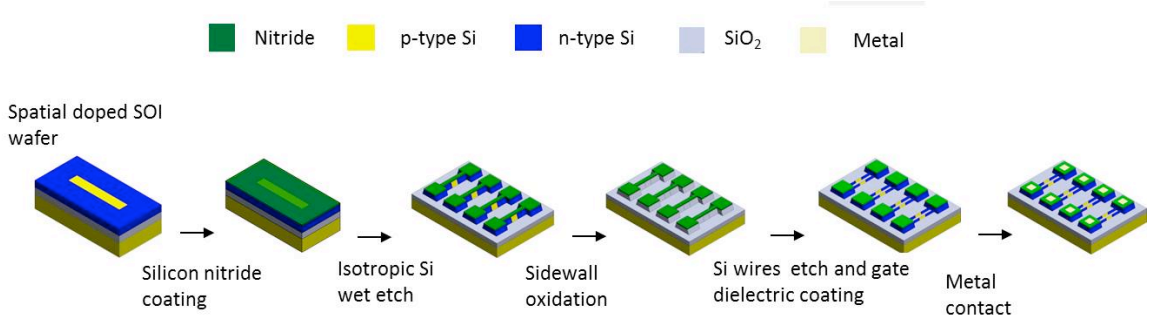


**Figure 4-2** Cartoon of fabrication process for top-down, Si NW FETs. Image courtesy of Xiahua Zhong.

### 4.2.9 Electronic Measurements of Si NW FETs

Si NW FET devices were fabricated and tested for electrical properties and passivation by Xiahua Zhong. Solution-gated electronic measurements were performed with an Agilent semiconductor parameter analyzer 4155C using Labview software. A cartoon of the measurement setup is shown in Figure 4-3. A silicone spacer was adhered to the chip surface and filled with solution (buffer or analyte) using a syringe or plastic tubing connected to a syringe pump. Gold electrodes were used to probe source and drain and apply a solution gate voltage. Measurement buffer was composed of 10 μM sodium phosphate and 50 μM potassium chloride at pH 7.4, which resulted in a solution ionic strength of 0.11 mM (Debye length of ~ 30 nm).

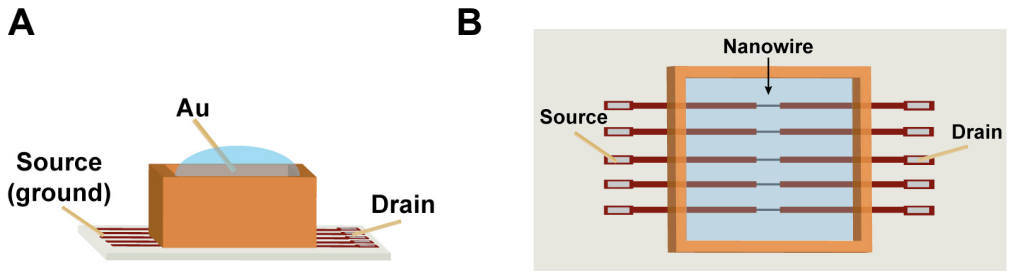


**Figure 4-3** Simplified cartoon of (A) side and (B) top view of chip and measurement setup using a silicone spacer.

For biomolecule attachment, devices were first functionalized in a solution of 3% APTMS in 200 proof ethanol for 1 hour. After this, they were rinsed with ethanol and DI water thoroughly and dried with $N_2$. For biotinylated devices: A solution of 5 mg NHS-SS-Biotin in 500 μL buffer (10 μM sodium phosphate and 10 μM potassium chloride, pH 7.4; ionic strength was 0.07 mM) was prepared and 100 μL was added to the silicon spacer for 2.5 hours. The device was rinsed thoroughly with DI and dried with $N_2$ and then a solution of avidin (2 mg in 100 uL buffer) was added to the silicone spacer for 2 hours. Rinse and dry steps were repeated and a final solution of DTT (50 mM, 100 μL) was added. Transfer curves were collected after each step during functionalization. For DNA or PNA functionalized devices: Devices were incubated in 100 μL of 5 mM sulfo-SMCC prepared in 10 mM CHES buffer at pH 9.5 for 1 hour. After rinse and dry steps, 100 μL of 1 μM probe DNA or probe PNA in reaction PBS was added to the spacer for 1 hour. Different concentrations of target DNA, prepared in measurement buffer described above, were used for biosensing measurements.

### 4.3 Results and Discussion

Due to a finite number of working FET devices to study, it was useful to optimize the surface chemistry of probe attachment and target capture off chip. For this purpose, metal nanowires (NWs) with a $SiO_2$ shell were used to mimic the reaction surface of the gate dielectric on the FETs. Then, device response to changes in solution pH and attempts to demonstrate biosensing are shown.

### 4.3.1 Surface Chemistry Validation

$SiO_2$-coated NWs were functionalized with APTMS and a crosslinker was chosen based on the desired target. For biotin/streptavidin chemistry, a biotinylated crosslinker was used, NHS-LC-Biotin (Figure 4-4, top). DNA hybridization required the use of a bifunctional crosslinker; one that reacted with both the amine from APTMS and the thiol on probe DNA (Figure 4-4, bottom).

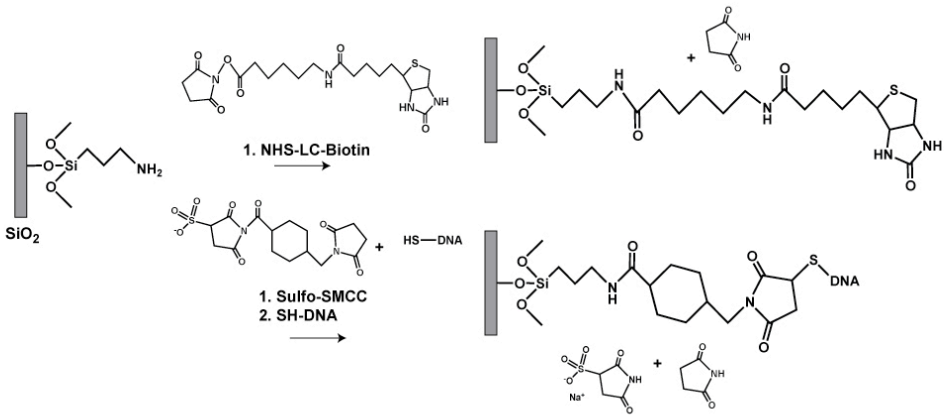


**Figure 4-4** Reaction of APTMS with water soluble, amine-reactive, crosslinking reagents used to functionalize surfaces with probe receptors for the capture of (top) streptavidin/avidin or (bottom) DNA target molecules.

The biotin/(strept)avidin interaction is commonly used in early demonstrations of biosensors and has been reported by multiple authors for nanoscale bioFET devices.[23-25] Streptavidin and avidin are both proteins that bind to biotin with exceptionally high affinity, as seen by its large binding constant ($K_d$) ~$10^{13}$-$10^{15}$ $M^{-1}$, regardless of solution ionic strength.[26] This affords the option to modulate salt conditions based on desired Debye length screening without compromising target capture efficiency. Prior to FET sensing, the chemistry attachment was validated off chip as shown in Figure 4-5, A. $SiO_2$-coated NWs were reacted with APTMS and half were subsequently biotinylated.

Upon incubation with fluorescently-labeled streptavidin, fluorescence and corresponding reflectance microscope images demonstrate successful, selective, capture of streptavidin to biotinylated NWs (Figure 4-5; B, C). As previously mentioned, this chemistry is important for biosensing to enable a variety of solution ionic strengths to be examined without concern of reduced target binding efficiency. Surface chemistry and detection of DNA target with $SiO_2$-functionalized with probe DNA was also performed. The resulting images and analysis is discussed in detail in Chapter 5.

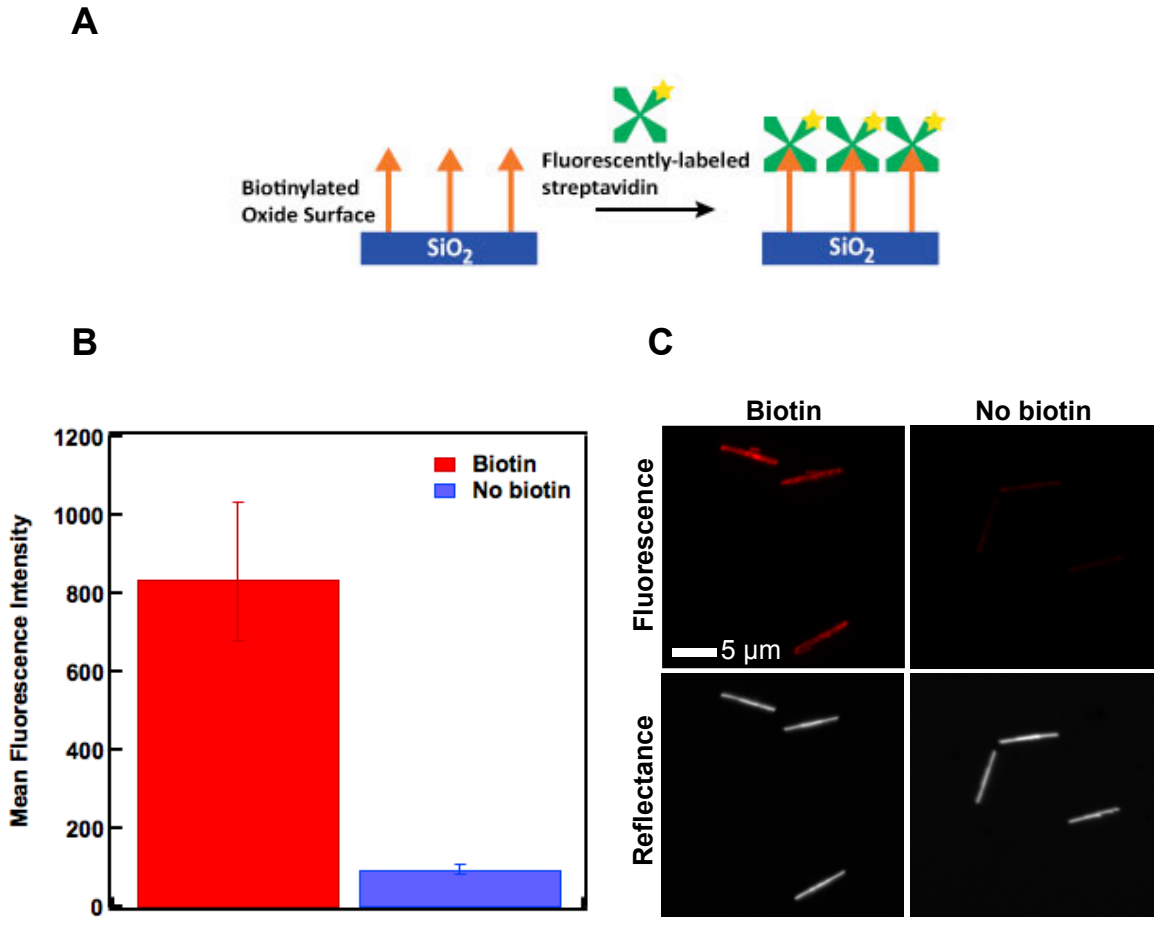


**Figure 4-5** (A) Cartoon of reaction between biotinylated-$SiO_2$ and fluorescently-labeled streptavidin protein (B) Mean fluorescence intensity of fluorescence images (C) from biotinylated and no biotin samples demonstrate a 8-fold increase.

### 4.3.2 pH Measurements with Si NW FETs

The detection of pH with Si NW FETs was useful to establish device performance because data can be directly compared to other devices. Based on the same mechanistic principle for traditional ion-sensitive field effect transistors (ISFETs) reported over 40 years ago, solution pH dictates the channel conductance based on protonation/deprotonation of surface hydroxyl groups on the gate dielectric.[27] In Figure 4-6, A and B, current between drain-source electrodes ($I_{DS}$) was held constant and the solution gate potential ($V_{SG}$) was measured as a function of time where a minimum baseline potential was applied to promote channel conductance or "turn on" the device. An increase in solution pH (more negative charge along the gate dielectric) resulted in higher resistance inside the channel. Thus, to maintain constant $I_{DS}$ in the channel, a higher $V_{SG}$ was required (supplied by a feed-back loop) (Figure 4-6; A). Upon reducing the solution pH, the opposite result was observed with slight hysteresis (disagreement in surface potential between forward and backward traces), which can be observed with $SiO_2$ due to the presence of a memory effect-a very slow pH response.[28] The same measurement was repeated after functionalization of the gate dielectric with amine groups via APTMS (Figure 4-6, B). The $pK_a$ of the amine group in bulk solution is ~9 so at pH less than 9 the amine group is protonated, as was the case for this measurement.[29] Hysteresis in this measurement was greatly improved, which has been observed upon surface modification, due to a reduction in adsorbed water molecules on the gate dielectric.[30] Comparison of the change in solution potential ($\Delta V_{SG}$) with pH showed a (mostly) linear relationship for both devices and pH sensitivity of ~25 mV/pH and ~36 mV/pH, respectively (Figure 4-6, C). Bare $SiO_2$ departed from linearity at low pH, as

previously shown[28], near the point of zero charge (pH ~2) and an increase in ionization sites is attributed to the better a linear fit for APTMS-modified devices.[1] An overall higher pH sensitivity for the APTMS-modified device was also shown, which compares well to a published value ~40 mV/pH.[1] Since the performance of the devices was good, further functionalization was completed for biosensing.

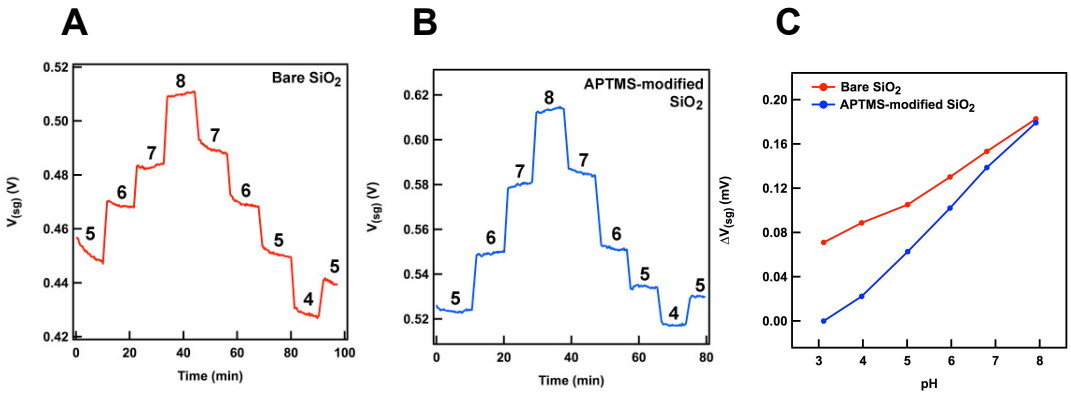


**Figure 4-6** Graph of $V_{SG}$ with time upon changes in solution pH is shown (A) without or (B) with an APTMS-functionalized $SiO_2$ gate dielectric where $I_{DS}$ was held constant. The resulting $\Delta V_{SG}$ compared to pH (C) demonstrates bare $SiO_2$ (black) and APTMS-modified (red) devices have an average pH sensitivity of ~25 mV/pH and ~36 mV/pH, respectively.

### 4.3.3 Si NW FET Response to Solutions of Avidin Protein

To verify device response after functionalization with probe molecules we began with a simplified detection scheme as shown in Figure 4-3 with n-type NW FET devices. A picture of the actual setup (Figure 4-7, A) and an example of the anticipated result from a transfer where $I_{DS}$ is measured as a function of sweeping $V_{SG}$ before and after introduction of target solution is shown (Figure 4-7, B). With n-type NW devices, positively charged target causes an increase of current through the Si channel and decrease in gate voltage is observed.[14]

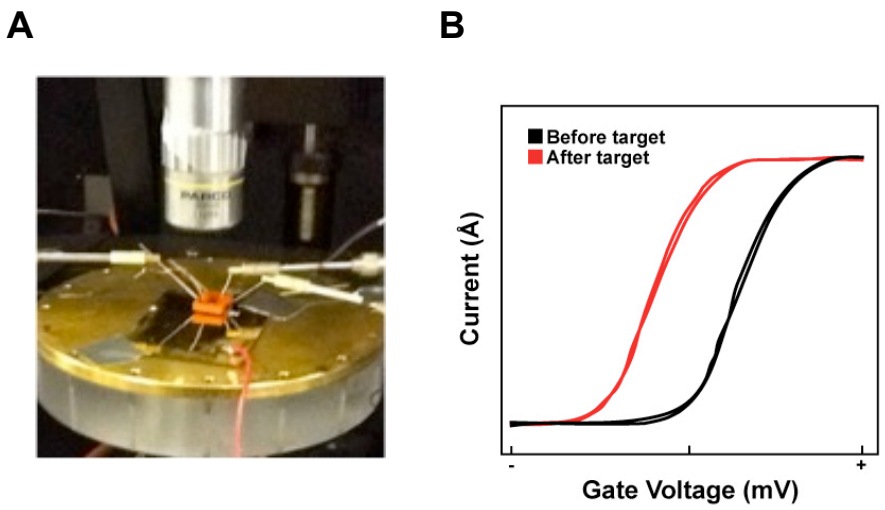


**Figure 4-7** (A) Photo of measurement setup and (B) anticipated results before and after capture of positively charged target.

A chip with several NW FET devices was functionalized with a cleavable, biotin linker, NHS-SS-biotin, and avidin (Figure 4-8, A). Avidin (pI ~ 10.5) has a large net positive charge near pH 7, as compared to streptavidin (pI ~5), which is weakly negative.[26] We took advantage of this difference to monitor changes in channel conductance upon target capture. The use of a cleavable linker was chosen to enable subsequent removal of avidin (positive charge) from the surface.

The working condition and electrical properties of each device on the chip were assessed prior to functionalization. The devices with good electrical properties were measured again after each functionalization step. A graph of one device during the process (Figure 4-8, A) is shown in Figure 4-8, B. As expected, positive charge introduced by amine groups on APTMS increased channel conductance and shifted $V_{SG}$ to the left. Uncharged biotin was expected to remove a portion of the positive charge along the surface due to reaction of amines with the linker and result in a right shift (decrease in $V_{SG}$). This did not occur and instead, a slight shift to the left was observed.

The addition of avidin and subsequent cleavage the di-thiol bond in the biotin linker with reducing agent dithiothreitol (DTT) resulted in a small right shift and large left shift, respectively.

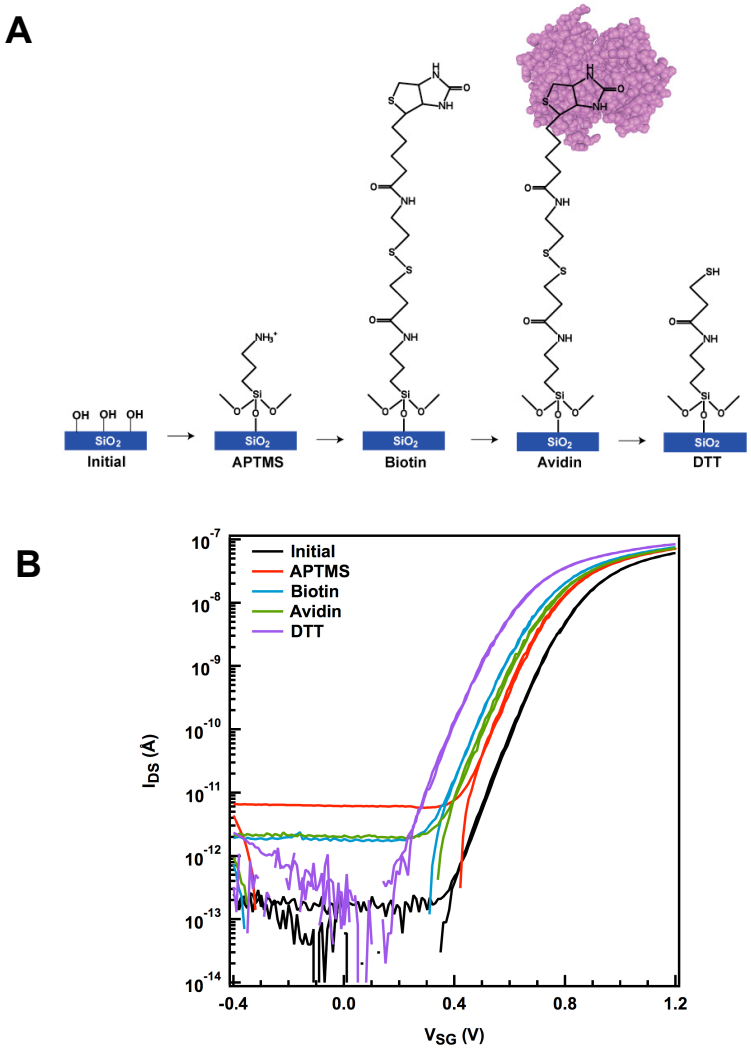


**Figure 4-8** (A) Expected surface reaction progress during Si nanowire FET electrical measurements of $SiO_2$-coated Si wafer with APTMS followed by NHS-SS-Biotin, avidin, and DTT. Not drawn to scale. (B) Transfer characteristic plot of $I_{DS}$ versus $V_{SG}$ after each step in the reaction was collected.

The results did not produce shifts in current as was expected based on changing surface chemistry. Photoresist was used on parts of the chip for passivation and it is possible

devices were damaged prior to measurement due to the dissolution and redeposition of photoresist onto devices. Subsequent experiments used a different photoresist that was not soluble in EtOH.

### 4.3.4 Si NW FET Response to Solutions of Target DNA

Electrical measurements of DNA surface functionalization were carried out in a similar process as described above for the detection of avidin with the anticipation that negatively charged DNA would provide a stark contrast to the positively-charged APTMS surface. A graph of the surface functionalization expected and resulting transfer characteristic plot is shown in Figure 4-9; A and B, respectively. Small hysteresis was observed in the initial measurement prior to functionalization. Subsequent traces measured after APTMS and DNA show negligible and small left shift in $V_{SG}$, respectively. For n-type FETs, negative charge from covalently attached DNA should result lower channel conductance and thus shift to the right with a higher $V_{SG}$.

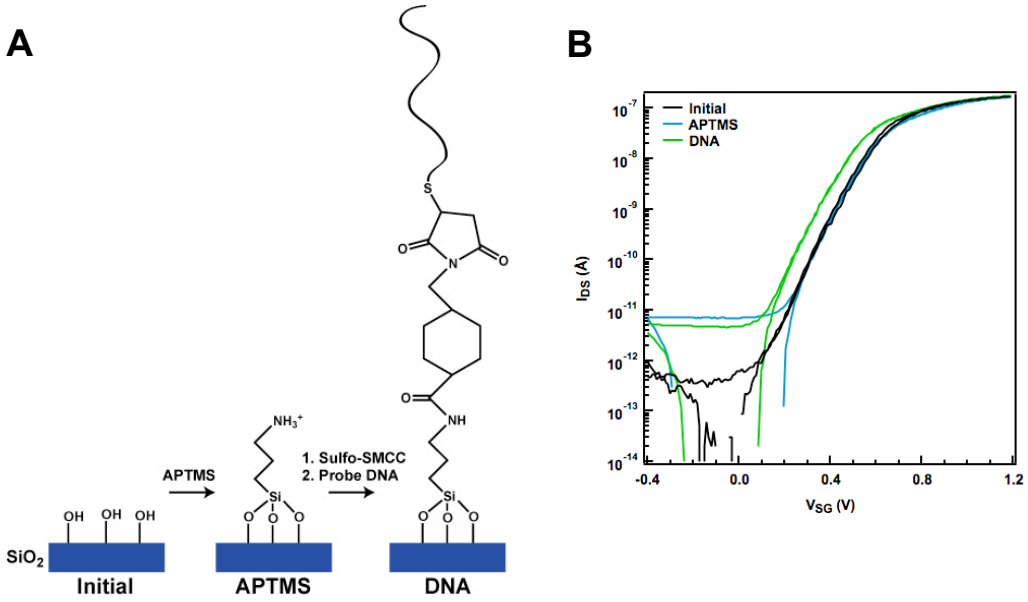


**Figure 4-9** (A) Expected surface reaction progress during Si NW FET electrical measurements of $SiO_2$-coated Si wafer with 3-aminopropyltrimethoxysilane (APTMS) followed by sulfo-SMCC (not shown), and DNA. $I_{DS}$ versus $V_{SG}$ after reaction with APTMS and DNA was collected. (B) A representative trace from one device measured is presented.

The data suggested the surface attachment chemistry was not present or did not have the anticipated charge, however based on the NW experiments and numerous published works with APTMS[22,31,32], we were inclined to believe this wasn't the case. This experiment may have been negatively impacted by partial dissolution of spacer adhesive in EtOH during the APTMS reaction step. This could have blocked surface reaction sites and reduced device sensitivity. Alternatively, $SiO_2$-based gate dielectrics are well known for solution instability and measurement drift can cause difficulty with data interpretation.[28] Furthermore, difficulty maintaining device performance for replicate measurements indicated a problem with device fabrication. Thus, ambiguous device response between measurements could be caused by dissolution and readsorption of EtOH-soluble molecules onto the sensor surface, poor electronic device properties, or

measurement drift due to $SiO_2$ gate dielectric. To more easily investigate the latter, chips were functionalized with peptide nucleic acid (PNA) probe and the device response to negatively charged DNA was measured in real-time. Complications with EtOH soluble molecules were avoided by using a different photoresist and not adhering the spacer until after APTMS functionalization step.

### 4.3.5 Real-time FET Response to Solutions of Target DNA

Transfer characteristic plots shown in the previous section enable comparison of "turn on" voltage. Real-time measurements, $I_{DS}$ versus time at a constant $V_{SG}$, enable small changes in device response to be observed. For n-type devices we would expect a linear current with time in buffer (Figure 4-10, black line), increased current upon addition of positively charged molecules (ex. APTMS) and decreased current with negatively charged molecules (ex. DNA, Figure 4-10, red line).

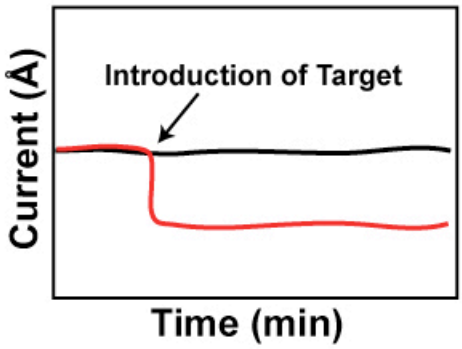


**Figure 4-10** Expected real-measurement results with n-type FET upon measurement in buffer alone (black) or buffer followed by negatively charged target (red).

Real-time measurements may be more useful to elicit changes in current due to molecular binding. The first real-time measurement examined drift in the device over

time (Figure 4-11). Using the same setup as shown previously, Figure 4-3, solutions were introduced to the silicone spacer via syringe. Measurement of $V_{SG}$ via an Ag/AgCl reference electrode was compared over time. Current steadily increased with time, which can be expected due to the gate dielectric employed. After a baseline was collected for over 90 minutes, the solution was changed. During this time, severe disruption of the baseline was observed. Eventually, 170 minutes through the measurement, a baseline was reestablished and upon introduction of complementary DNA drift in the baseline ceased. Further results could not be determined due to loss of signal when the solution in the silicone spacer dried.

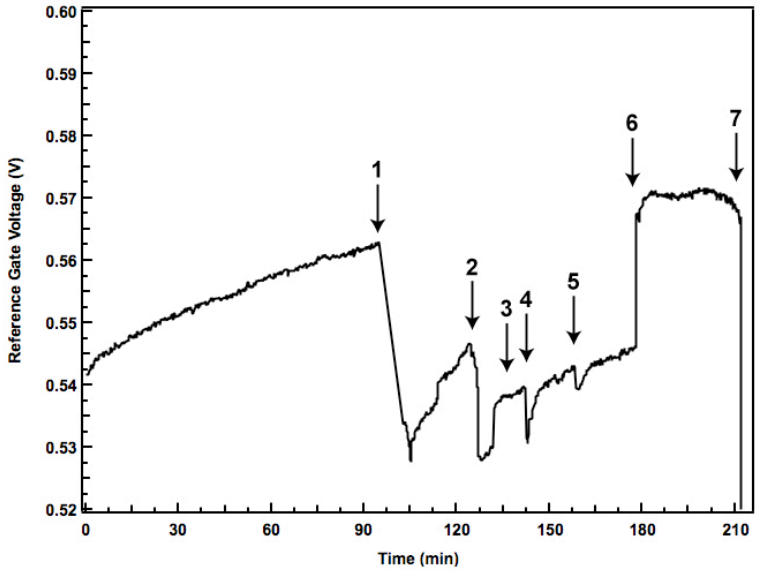


**Figure 4-11** Solution-gated real-time Si nanowire FET measurement of static DNA hybridization with PNA functionalized device. After a baseline was established solution volume was changed via syringe resulting in loss of the baseline (1). Addition of complementary target DNA caused a large voltage increase and eliminated drift (6). Remaining arrows indicate the point at which solution was removed from the spacer (2), or unexpected spikes occurred (3-5, 7).

The complexity of device fabrication, functionalization, and measurements complicated performance optimization. It was unclear if poor technique was used to deliver solution and measure device response or if there were intrinsic problems with device fabrication. For this reason, we directed our efforts to validate our device setup and measurement protocol modeling top-down device fabrication and detection methods.

Several changes were implemented to align our device fabrication and measurement execution strategy with those who have published in this field.[23] A mixing cell for solution delivery with syringe pumps was employed and a reference electrode was omitted due to concern for non-specific analyte adsorption[33] and lack of room in the spacer. Some groups have published lithographically defined reference electrodes[34] or designed electrode placement in microfluidic channels[35], but the majority of FET literature determines solution potential by the applied $V_{SG}$.

Real-time measurements of $I_{DS}$ versus time at constant $V_{SG}$ on a PNA-functionalized device is shown in Figure 4-12 where arrows indicate the starting point of flowing buffer (green), non-complementary (NC) target DNA (Flu A, red), and complementary (Comp) target DNA (Flu B, blue). During the experiment, we discovered the device was very sensitive to movement too close to the experimental setup and changes in solution flow as seen by many spikes in current not during solution changes. Several trials (not shown) were aborted prior to delivery of Comp target due to drastic spikes in current or a loss of baseline. The final measurement, shown in Figure 4-12, demonstrated a large, consistent response to DNA solutions.

Unfortunately, the device response to Comp target and NC target are indistinguishable and challenging to interpret based on the n-type channel doping. The negatively charged

DNA was expected to decrease current due to reduced channel conductance, however an increase in channel conductance indicated a positive surface potential was present. A low ionic strength buffer (0.1 mM) was used to maximize solution Debye length. Aqueous solutions of DNA have a pH < 5, so it was possible insufficient buffer capacity or improper buffer preparation resulted in an acidic solution that caused a positive surface potential (which was removed upon solution change to buffer-only).

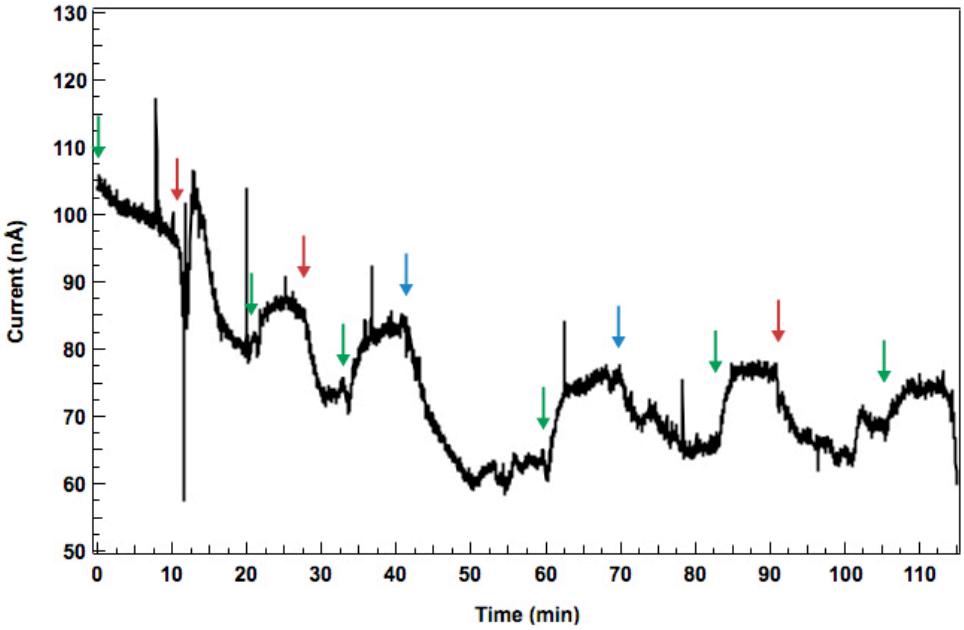


**Figure 4-12** Solution-gated real-time Si nanowire FET measurement of DNA hybridization with PNA functionalized device. Plot of $I_{DS}$ versus time demonstrates non-specific device response to Comp and NC target DNA. Arrows indicate the starting point of flowing buffer (green), NC DNA target, (Flu A, red), and Comp DNA target (Flu B, blue).

A revised fabrication process was developed in response to reports that nitrogen annealing Si NW FET improved device performance by reducing surface defects.[1] With the same measurement conditions used previously, another real-time experiment was

performed (Figure 4-13). First, the device response to repeated changes in buffer and NC DNA were measured (Figure 4-13, A). A second trial (not shown) ended after only 2 minutes of flowing buffer due to a spacer leak. After a new spacer was attached, a third trial (Figure 4-13, B) demonstrated inconsistent device response to all solution changes. Large decreases in current were observed upon introduction of NC DNA target, but this was not observed for Comp DNA. Because stabilization or baseline was achieved upon introduction of buffer after NC DNA, it was again implied that the solution was causing a change in conductance, not binding of target. Electrolytic solutions have been observed to modulate channel conductance[36], but if that was the case it is unclear why a similar response was not observed for Comp DNA.

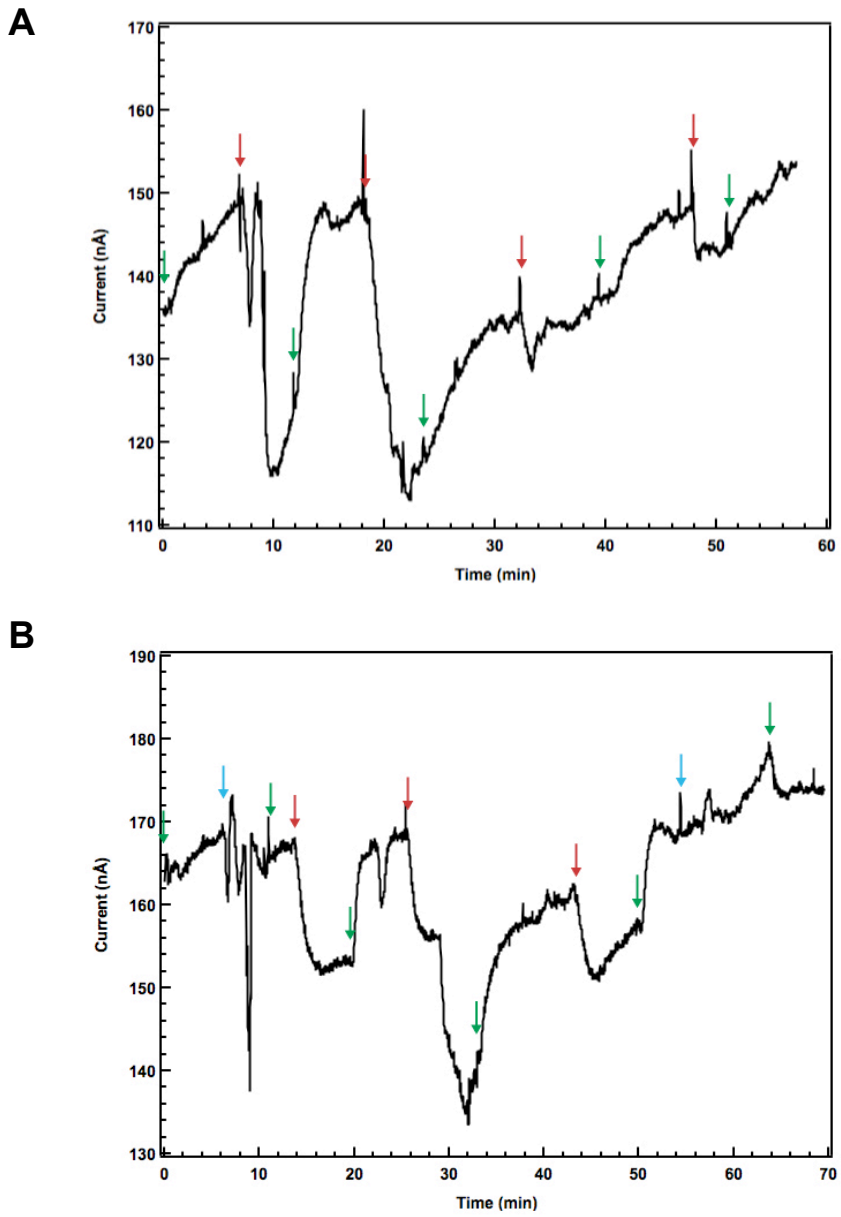


**Figure 4-13** Solution-gated real-time Si NW FET measurement of DNA hybridization with PNA functionalized device. Plot of $I_{DS}$ versus time after solution changes between (A) buffer and NC target DNA or (B) buffer, Comp, and NC target DNA. Arrows indicate the starting point of flowing buffer (green), NC DNA target, (Flu A, red), and Comp DNA target (Flu B, blue).

Based on our measurement results, we found it difficult to compare the effect of NC and Comp target solutions because of drift in the measurement, problems with solution

delivery, or syringe changes that disrupt the baseline. For this reason we moved onto a dual device setup where all devices were connected to a common ground via a silver epoxy and two devices were probed simultaneously during the measurement. In Figure 4-14, a topview (A) and sideview (B) cartoon of device functionalization and measurement setup for simultaneous, dual, real-time measurement is shown. Different probe functionalization across the chip enabled simultaneous Comp versus NC target signal. Thus, the effect of solution changes or baseline disruptions would occur for both devices and could be accounted for. Comparison of two devices in the transfer characteristic plot (Figure 4-14, C) was useful to find devices with similar sensitivity and "turn on" voltages. The real-time measurement (Figure 4-14, D) shows device response upon delivery of buffer (green), target DNA NC to either probe functionalization (brown), Flu B target (blue), and Flu A target (red). Overall, the net changes in current due to solution changes were very small compared to previous sensing experiments. Upon delivery of Flu B target a similar trace was observed for both devices despite probe complementarity to only one device and significant differences were not observed with Flu A target. It is unclear why the overall sensitivity of this device to solution changes was low and demonstrated no target specificity. However, it appears many factors can influence the device conductance and control experiments may be necessary to identify the cause.

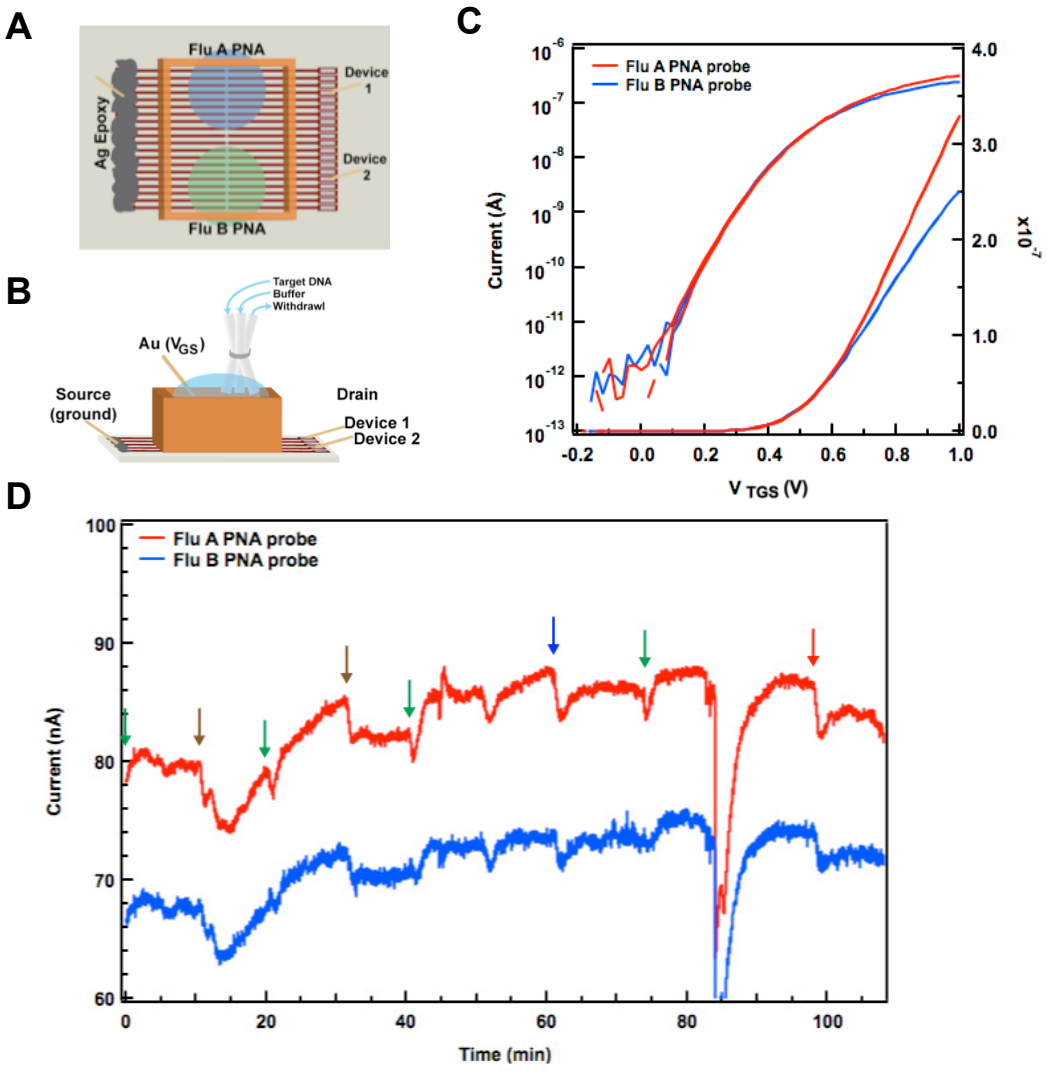


**Figure 4-14** Solution-gated real-time Si NW FET measurement of DNA hybridization with device functionalized with two distinct regions of PNA probe molecules. (A) Devices 1-8 were functionalized with Flu B PNA probe and devices 12-20 were functionalized with Flu A PNA probe. The transfer characteristic plot (B) displayed both log and linear regimes of each device for comparison of electronic properties. (C) The setup for dual device response with solution changes between buffer and DNA target solutions are shown. The sensing plot (D) displayed the real-time $I_{DS}$ measured during solution delivery with Flu A PNA probe (red trace) or Flu B PNA probe (blue trace) functionalized devices. Arrows indicate the starting point of flowing buffer (green), NC DNA (T3) to either PNA probe (brown), Flu A DNA target (red), and Flu B target DNA (blue)

Initial dual sensing measurements were performed with any pair of devices that turned on at similar voltages. Upon further examination of the chips after the real-time measurements by optical microscopy and FESEM, it was discovered that some devices chosen were not optimal due to fabrication abnormalities (missing wires or incomplete etching) or photoresist residue. This could explain some non-optimal measurement responses. Chips were then imaged by optical microscopy and FESEM to establish good devices however devices were no longer able to turn on. For this reason, FESEM (and other potentially damaging characterization methods) are recommended only for devices that are no longer desired for sensing measurements.

### 4.4 Conclusions

The experiments performed in this chapter were designed to study the Si NW FET response to solutions of analyte. Due to limited number of working devices, two methods of receptor attachment for the capture of target were validated, successfully, off chip on $SiO_2$-coated metal NWs. Si NW FETs were fabricated and the device performance was examined by its response to changes in solution pH for bare and APTMS-modified $SiO_2$ devices. Excellent $\Delta V_{SG}$ versus pH linearity was observed for APTMS-modified devices and resulted in a high pH sensitivity of 36 mv/pH. Si NW FETs were also functionalized with biomolecules to study device properties. A complex mechanism of detection was discovered with solution-based measurements. Device response was highly sensitive to perturbations in device setup and solution flow. Ultimately, low device yields and device-device variability limited our ability to characterize and optimize the measurement conditions. The integration of a reference electrode onto the biosensor platform in

addition to a controlled solution delivery method is needed to realize the full potential of Si NW FETs.

### 4.5 References

1. Chen, S.; Bomer, J. G.; Carlen, E. T.; Berg, A. V. D. Al2O3/Silicon NanoISFET with Near Ideal Nernstian Response. *Nano Lett.* **2011**, *11*, 2334-2341.

2. Reddy, B.; Dorvel, B. R.; Go, J.; Nair, P. R.; Elibol, O. H.; Credo, G. M.; Daniels, J. S.; Chow, E. K. C.; Su, X.; Varma, M.; Alam, M. A.; Bashir, R. High-k dielectric $Al_2O_3$ Nanowire and Nanoplate Field Effect Sensors for Improved pH Sensing. *Biomed. Microdevices* **2011**, *13*, 335-344.

3. Zhou, X. T.; Hu, J. Q.; Li, C. P.; Ma, D. D. D.; Lee, C. S.; Lee, S. T. Silicon Nanowires as Chemical Sensors. *Chem. Phys. Lett.* **2003**, *369*, 220-224.

4. Cuscunà, M.; Convertino, A.; Zampetti, E.; Macagnano, A.; Pecora, A.; Fortunato, G.; Felisari, L.; Nicotra, G.; Spinella, C.; Martelli, F. On-Chip Fabrication of Ultrasensitive $NO_2$ Sensors Based on Silicon Nanowires. *Appl. Phys. Lett.* **2012**, *101*, 103101.

5. Patolsky, F.; Zheng, G.; Hayden, O.; Lakadamyali, M.; Zhuang, X.; Lieber, C. M. Electrical Detection of Single Viruses. *Proc. Nat. Acad. Sci.* **2004**, *101*, 14017-14022.

6. Tian, R.; Regonda, S.; Gao, J.; Liu, Y.; Lu, W. Ultrasensitive Protein Detection Using Lithographically Defined Si Multi-Nanowire Field Effect Transistors. *Lab on a Chip* **2011**, *11*, 1952-1961.

7. Gao, A.; Lu, N.; Dai, P.; Li, T.; Pei, H.; Gao, X.; Gong, Y.; Wang, Y.; Fan, C. Silicon-Nanowire-Based CMOS-Compatible Field-Effect Transistor Nanosensors for Ultrasensitive Electrical Detection of Nucleic Acids. *Nano Lett.* **2011**, *11*, 3974-3978.

8. Zheng, G.; Patolsky, F.; Cui, Y.; Wang, W. U.; Lieber, C. M. Multiplexed Electrical Detection of Cancer Markers with Nanowire Sensor Arrays. *Nat. Biotech.* **2005**, *23*, 1294-1301.

9. Rissin, D. M.; Kan, C. W.; Campbell, T. G.; Howes, S. C.; Fournier, D. R.; Song, L.; Piech, T.; Patel, P. P.; Chang, L.; Rivnak, A. J.; Ferrell, E. P.; Randall, J. D.; Provuncher, G. K.; Walt, D. R.; Duffy, D. C. Single-Molecule Enzyme-Linked Immunosorbent Assay Detects Serum Proteins at Subfemptomolar Concentrations. *Nat. Biotech.* **2010**, *28*, 595-599.

10. Lee, T. M.-H. Over-the-Counter Biosensors: Past, Present, and Future. *Sensors*, **2008**, *8*, 5535-5559.

11. Hartman, M. R.; Ruiz, R. C. H.; Hamada, S.; Xu, C.; Yancey, K. G.; Yu, Y.; Han, W.; Luo, D. Point-of-Care Nucleic Acid Detection Using Nanotechnology. *Nanoscale*, **2013**, *5*, 10141-10154.

12. Vacic, A.; Reed, M. A. Quantitative Nanoscale Field Effect Sensors. *J. Exp. Nanosci.* **2014**, *9*, 41-50.

13. Vacic, A.; Criscione, J. M.; Stern, E.; Rajan, N. K.; Fahmy, T.; Reed, M. A. Multiplexed SOI BioFETs. *Biosens. Bioelectron.* **2011**, *28*, 239-242.

14. Curreli, M.; Zhang, R.; Ishikawa, F. N.; Chang, H.-K.; Cote, R. J.; Zhou, C.; Thompson, M. E. Real-Time, Label-Free Detection of Biological Entities Using Nanowire-Based FETs. *IEEE Trans. Nanotech.* **2008**, *7*, 651-666.

15. Nicewarner-Pena, S. R.; Freeman, R. G.; Reiss, B. D.; He, L.; Pena, D. J.; Walton, I. D.; Cromer, R.; Keating, C. D.; Natan, M. J. Submicrometer Metallic Barcodes. *Science* **2001**, *294*, 137-141.

16. Al-Mawlawi, D.; Liu, C. Z.; Moskovits, M. Nanowires Formed from Anodic Oxide Nanotemplates. *J. Mater. Res.* **1994**, *9*, 1014-1018.

17. Martin, C. R. Nanomaterials: A Membrane-Based Synthetic Approach. *Science* **1994**, *266*, 1961-1966.

18. Martin, B. R.; Dermody, D. J.; Reiss, B. D.; Fang, M.; Lyon, L. A.; Natan, M. J.; Mallouk, T. E. Orthogonal Self-Assembly on Colloidal Gold-Platinum Nanorods. *Adv. Mater.* **1999**, *11*, 1021-1025.

19. Kirby, D. J.; Smith, B. D.; Keating, C. D. Microwell-Directed Self-Assembly of Vertical Nanowire Arrays, *Part. Part. Syst. Charact.* **2013**, DOI: 10.1002/ ppsc.201300260.

20. Yin, Y.; Lu, Y.; Sun, Y.; Xia, Y. Silver Nanowires can be Directly Coated with Amorphous Silica to Generate Well-Controlled Coaxial Nanocables of Silver/Silica. *Nano Lett.* **2002**, *2*, 427-430.

21. Sioss, J. A.; Keating, C. D. Batch Preparation of Linear Au and Ag Nanoparticle Chains via Wet Chemistry. *Nano Lett.* **2005**, *5*, 1779-1783.

22. Sioss, J. A.; Stoermer, R. L.; Sha, M. Y.; Keating, C. D. Silica-Coated, Au/Ag Striped Nanowires for Bioanalysis. *Langmuir* **2007**, *23*, 11334-11341.

23. Stern, E.; Wagner, R.; Sigworth, F. J.; Breaker, R.; Fahmy, T. M.; Reed, M. A. Importance of the Debye Screening Length on Nanowire Field Effect Transistor Sensors. *Nano Lett*. **2007**, *7*, 3405-3409.

24. Gupta, S.; Elias, M.; Wen, X.; Shapiro, J.; Brillson, L.; Lu, W.; Lee, S. C. Detection of Clinically Relevant Levels of Protein Analyte Under Physiologic Buffer Using Planar Field Effect Transistors. *Biosens. Bioelectron.* **2008**, *24*, 505-511.

25. Chen, Y. W.; Liu, M.; Kaneko, T.; McIntyre, P. C. Atomic Layer Deposited Hafnium Oxide Gate Dielectrics for Charge-Based Biosensors. *Electrochem. Solid State Lett.* **2010**, *13*, G29-G32.

26. Green, N. M. Avidin. I. The Use of Biotin-14C for Kinetic Studies and for Assay. *Biochem. J.* **1963**, *89*, 585-591.

27. Bergveld, P. Thirty Years of ISFETOLOGY: What Happened in the Past 30 Years and What May Happen in the Next 30 years. *Sens. Actu. B: Chem.* **2003**, *88*, 1-20.

28. Bousse, L.; Bergveld, P. The Role of Buried OH Sites in the Response Mechanism of Inorganic-Gate pH-Sensitive ISFETs. *Sens. Actu.* **1984**, *6*, 65-78.

29. Santra, S.; Bagwe, R. P.; Dutta, D.; Stanley, J. T.; Walter, G. A.; Tan, W.; Moudgil, B. M.; Mericle, R. A. Synthesis and Characterization of Fluorescent, Ratio-Opaque, and Paramagnetic Silica Nanoparticles for Multimodal Bioimaging Applications. *Adv. Mater.* **2005**, *17*, 2165-2169.

30. Hu, P.; Zhang, C.; Fasoli, A.; Scardaci, V.; Pisana, S.; Hasan, T.; Robertson, J.; Milne, W. I.; Ferrari, A. C. Hysteresis Suppression in Self-Assembled Single-Wall Nanotube Field Effect Transistors. *Physica E* **2008**, *40*, 2278-2282.

31. Zhang, F.; Srinivasan, M. P. Self-Assmbled Molecular Films of Aminosilanes and their Immobilization Capacities. *Langmuir* **2004**, *20*, 2309-2314.

32. Allen, G. C.; Sorbello, F.; Altavilla, C.; Castorina, A.; Ciliberto, E. Macro-, Micro- and Nano-Investigations on 3-Aminopropyltrimethoxysilane Self-Assembly-Monolayers. *Thin Solid Films* **2005**, *483*, 306-311.

33. Bergveld, P. A Critical Evaluation of Direct Electrical Protein Detection Methods. *Biosens. Bioelectron.* **1991**, *6*, 55-72.

34. Chen, Y.-P.; Zhao, Y.; Chu, J.; Liu, S.-Y.; Li, W.-W.; Liu, G.; Tian, Y.-C.; Xiong, Y.; Yu, H.-Q. Fabrication and Characterization of an Innovative Integrated Solid-State Microelectrode. *Electrochimica Acta* **2010**, *55*, 5984-5989.

35. Subramani, B. G.; Selvaganapathy, P. R. Surface Micromachined PDMS Microfluidic Devices Fabricated Using a Sacrificial Photoresist, *J. Micromech. Microeng*. **2009**, *19*, 015013.

36. Kim, D. R.; Lee, C. H.; Zheng, X. Probing Flow Velocity with Silicon Nanowire Sensors. *Nano Lett*. **2009**, *9*, 1984-1988.

# Chapter 5

# Removal of DNA Target for Biosensor Regeneration

## 5.1 Introduction

Electronic biosensors are popular for detection of a variety of targets including DNA, proteins, antibodies, and small molecules.[1] New developments in sensor design and detection performance are routinely published, but the removal of analyte to regenerate surfaces for successive measurements is generally absent. Instead, some groups use UV ozone or oxygen plasma to strip the surface of all molecules and repeat the functionalization process.[2] However, this is not ideal because prolonged or repeated UV ozone processing has been shown to degrade surface passivation and reduce device performance.[2,3] For example, upon exposure to UV ozone for 15 minutes, Si NW FETs have been rendered nonfunctional due to the creation of surface states between the gate oxide and Si interface.[2] Furthermore, oxygen plasma treatment suffers from poor control which has resulted in non-uniformity.[3] So, an alternative method that can remove analyte quickly and efficiently without damage to device properties would benefit the field.

The reversible binding of biomolecules to surfaces has been widely explored for applications in separations[4], biochemical kinetics[5], and traditional affinity-based bioassays[6]. The success of such applications relies on the interaction between an immobilized receptor (probe) with a ligand (analyte, or target) as denoted by R and L, respectively, in Equation 5-1.

$$RL \rightleftharpoons R + L$$

Equation 5-1

The disassociation constant ($K_d$) is used to describe the propensity of a complex, RL, to dissociate, which is dependent upon the concentration of reactants and products in a given system as shown in Equation 5-2.

$$K_d = \frac{[R][L]}{[RL]} \qquad \text{Equation 5-2}$$

The most common procedure to disrupt receptor-ligand complexes involves the use of low pH and low ionic strength.[7] For proteins, this treatment results in the protonation of carboxylates and reduced screening of ionizable functional groups, which is often enough to cause misfolding. In the case of DNA hybridization, low pH can damage DNA chemical structure, and in the absence of salt, electrostatic repulsion of the negatively charged phosphate backbone will cause strand dehybridization. Alternatively, chaotropic reagents (molecules that disrupt or denature macromolecules) including urea or guanidine hydrochloride reduce the receptor-ligand interactions by interfering with hydrogen bonds.[8] Targeted removal can be accomplished when ligands or receptor-ligand complexes have specific chemical groups, like disulfide bonds that can be cleaved by molecules such as dithiotreitol[9] (DTT) or are attached by reversible affinity tags[10] such as nickel nitrilotriacetic acid (Ni NTA). The most important aspect for surface regeneration strategies is that receptor/probe chemistry remains active for subsequent use, but for electrical-based biosensors, a secondary condition, preservation of device performance, is

required. For example, treatments involving acids and bases must be avoided as they could damage the devices.

The detection of DNA hybridization with charge-based biosensors, such as field-effect transistors (FETs), is a convenient model because one negative charge on phosphate for every nucleotide along the target DNA backbone provides a large change in local surface potential. Furthermore, DNA targets can hybridize to DNA or PNA probes. The latter, an uncharged peptide analog of DNA, is of great interest in biosensing because it can selectively bind to DNA target without electrostatic repulsion between probe and target strands, even in low ionic strength buffer. The enhanced stability of the DNA-PNA duplexes can be observed by higher $T_m$ (melting temperature) of 10 base oligonucleotides of DNA-PNA in comparison to DNA-DNA duplexes (52.1°C and 19.5°C, respectively) in 10 mM sodium phosphate buffer without additional salt.[11] Consequently, due to their higher stability, PNA-DNA duplexes are more difficult to separate or dehybridize.[12]

In this chapter, several mild reaction conditions were tested for their ability to remove target DNA from probe DNA or PNA (peptide nucleic acid) –functionalized surfaces. Using glass-coated nanowires (NWs) to model a $SiO_2$ gate dielectric on a biosensor surface, we examined two scenarios that could be utilized to remove target DNA: 1. Complete removal of the probe and target chemistry via cleavage of linker chemistry, or 2. Dehybridization of target DNA using a chaotropic reagent capable of denaturing DNA-DNA and DNA-PNA duplexes without extreme temperatures or pH.

## 5.2 Experimental Materials and Methods

### 5.2.1 Materials

Anodisc™ aluminum oxide membranes with a nominal pore size of 0.2 μm were purchased from Whatman. Orotemp 24 and Ag Cyless R plating solutions were obtained from Technic Inc. Tetraethoxysilane (TEOS) was purchased from Gelest. 3-aminopropyltrimethoxysilane (APTMS) was obtained from TCI America. N-cyclohexyl-2-aminoethanesulfonic acid (CHES), buffers, salts, and general chemicals were purchased from Sigma-Aldrich. Sulfosuccinimidyl-4-(*N*-maleimidomethyl)cyclohexane-1-carboxylate (Sulfo-SMCC) and Sulfosuccinimidyl 6-(3'-[2-pyridyldithio]-propionamido)hexanoate (Sulfo-LC-SPDP) was purchased from Pierce Protein Research Products, Thermo Scientific. DNA oligonucleotides were purchased from Integrated DNA Technologies Inc. PNA oligonucleotides were obtained from Bio-Synthesis Inc. Ethanol (EtOH, 200 proof) was supplied by Koptec. All water used was either 18.2 MΩ:cm Nanopure water from a Barnstead system or EMD Chemicals HPLC grade water. Buffer used for surface functionalization, reaction PBS, was prepared with EMD Chemicals HPLC grade water and contained 10 mM sodium phosphate and 300 mM sodium chloride at pH 7.4. All reagents were used without further purification; TEOS was aliquoted out in a glove box under $N_2$ to prevent hydrolysis.

**Table 5-1**: DNA and PNA probe and target sequences

| Name | Sequence 5′→ 3′<br>For PNA N-Terminus → C-Terminus | Description |
|---|---|---|
| Flu A DNA probe | Thiol-<br>TTTTTTTTTTGACCAATCCTGTCAC | Influenza A DNA probe |
| Flu B DNA probe | Thiol-<br>TTTTTTTTTTTTCTTTTTTGTTGCT | Influenza B DNA probe |
| Flu A PNA probe | Cys-OO-AATCCTGTCAC | Influenza A PNA probe |
| Flu B PNA probe | Cys-OO-TTTTTGTTGCT | Influenza B PNA probe |
| A647 Flu A DNA target | Alexa Fluor 647-GTGACAGGATT | Alexa647 Influenza A DNA target |
| A647 Flu B DNA target | Alexa Fluor 647-AGCAACAAAAA | Alexa647 Influenza B DNA target |

O = Solubility enhancer

### 5.2.2 Nanowire Synthesis

Metal nanowires were synthesized by galvanostatic electrodeposition into aluminum oxide templates as described previously.[13-16] Briefly, silver (300 nm) was evaporated on one side of membrane to act as the working electrode. Nanowires were electrodeposited into the alumina template pores and subsequently released by dissolving the silver backing and template with 33% v/v nitric acid and 3 M NaOH, respectively. Wires were rinsed twice with water and twice with EtOH before suspension in 1 mL EtOH at a concentration of ~ $10^9$ wires/mL.[17]

### 5.2.3 Silica Coating of Nanowires

Nanowires were coated with ~ 20-30 nm $SiO_2$ using TEOS as previously described.[18,19] Briefly, 300 μL nanowires at the batch concentration in EtOH are combined with 160 μL water, 10 μL $NH_4OH$, 490 μL EtOH, and 40 μL TEOS in a 1.7 mL microcentrifuge tube

and sonicated for 1 hour. After sonication, $SiO_2$-coated nanowires were rinsed three times with EtOH and resuspended in 900 μL EtOH. Transmission electron microscopy (TEM) images of nanowires were obtained with a JEOL TEM 1200 EXII instrument.

### 5.2.4 DNA and PNA Preparation

DNA and PNA arrived as a lyophilized pellet from Integrated DNA Technologies, Inc. or Bio-Synthesis Inc., respectively. Prior to use, fluorescently-labeled DNA and PNA oligonucleotides were rehydrated in 18.2 MΩ:cm Nanopure water. Thiol-terminated DNA was rehydrated in a 100 mM solution of DL-dithiothreitol in 10 mM sodium phosphate buffer at pH 8.3 to cleave any disulfide bridges present. After 1 hour the solution was desalted with a Princeton Separations (Adelphia, NJ) Centrispin 10 column, resulting in a solution of individual thiol-terminated DNA oligonucleotides.[20]

The sequence concentration of DNA or PNA was determined by measuring the solution absorbance at 260 nm using a Hewlett-Packard 8453 diode-array UV/visible spectrometer with Agilent ChemStation software. Sequences were diluted to either 100 μM or 20 μM and stored at -80°C.

### 5.2.5 Biofunctionalization of $SiO_2$-Coated Nanowires

Silica-coated metal nanowires were reacted with APTMS and a bifunctional crosslinker to enable covalent attachment of probe molecules by similar methods described previously.[20] Briefly, 300 μL $SiO_2$-coated metal nanowires, at batch concentration, were transferred to a 1.7 mL non-stick microcentrifuge tube, and EtOH was removed after centrifugation. Wires were vortexed in 500 μL 3% APTMS in 200 proof EtOH for 30

minutes then rinsed by centrifugation and resuspension once with EtOH and twice with either reaction PBS or CHES buffer. Wires were vortexed for 1-2 hours in 2 mg/mL bifunctional crosslinker in 1 mL reaction PBS (NHS-LC-Biotin or Sulfo-LC-SPDP) or CHES buffer (Sulfo-SMCC). Biotinylated samples required 3 rinse steps in reaction PBS to complete surface functionalization. DNA or PNA samples were rinsed 3 times in reaction PBS; wires were evenly split between two, 0.5 mL non-stick centrifuge tubes into which 1 μM complementary or non-complementary probe DNA or PNA (diluted with DI from 20 μM stock) was added. Wires were vortexed for 1 hour and DNA or PNA surface functionalization was completed after 3 rinse steps with reaction PBS. Wires were then imaged as described in Section 5.2.8.

### 5.2.6 Removal of Hybridized DNA from Nanowires with Cleavable Crosslinker

Probe-functionalized nanowires covalently attached using Sulfo-LC-SPDP as described above were incubated with 1 μM fluorescently labeled target DNA (diluted from 100 μM stock). Both samples were vortexed for 1 hour. After rinsing the wires, an aliquot from each tube was removed for imaging (Section 5.2.8) and the remaining wires were vortexed in 500 μL of 100 mM dithiothreitol (DTT) in reaction PBS for 30 minutes. Wires were protected from light throughout the experiment by wrapping in Al foil.

### 5.2.7 Removal of Hybridized Target DNA from Nanowires with Urea

Probe-functionalized nanowires covalently attached using Sulfo-SMCC as described above were incubated with 1 μM fluorescently labeled target DNA (diluted from 100 μM stock). Both samples were vortexed for 1 hour. After rinsing the wires, an aliquot from

each tube was removed for imaging (Section 5.2.8) and the remaining wires were vortexed in 1 mL 6.4 M urea for 1 hour at room temperature or 2 hours at 45$^{o}$C. After rinsing the wires, an aliquot from each tube was removed for imaging and the remaining wires were vortexed for 1 hour with 1 μM fluorescently labeled target DNA (diluted from 100 μM stock).

Wires were protected from light throughout the experiment by wrapping in Al foil.

### 5.2.8 Optical and Fluorescence Microscopy

Reflectance and fluorescence images of nanowires were obtained using Image-Pro Plus software with a Nikon TE-300 inverted microscope equipped with a Xe arc lamp and Photometrics Coolsnap HQ camera. A Plan Apo 60x oil or Nikon Plan Fluor 100x oil objective were used. Samples were prepared by placing a 10 μL buffer suspension of nanowires onto a glass slide with a coverslip. Fluorescence was quantified using NBSee Software (Nanoplex Technologies).

## 5.3 Results and Discussion

The following work determined the optimal reaction conditions to remove hybridized target DNA from a sensor surface while maintaining device performance and probe/receptor function. Specific conditions avoided, which may damage the device or probe chemistry, were extreme pH (outside of a range of 4-8) and temperatures greater than 100°C. Initial studies examined a targeted method to facilitate complete removal of DNA target and probe from the surface using DTT to cleave the disulfide bond in the

crosslinker chemistry, Sulfo-LC-SPDP (Figure 5-1, A). A secondary approach used urea to dehybridize DNA target from DNA or PNA probes that remained covalently attached to the sensor surface via Sulfo-SMCC crosslinking chemistry (Figure 5-1, B).

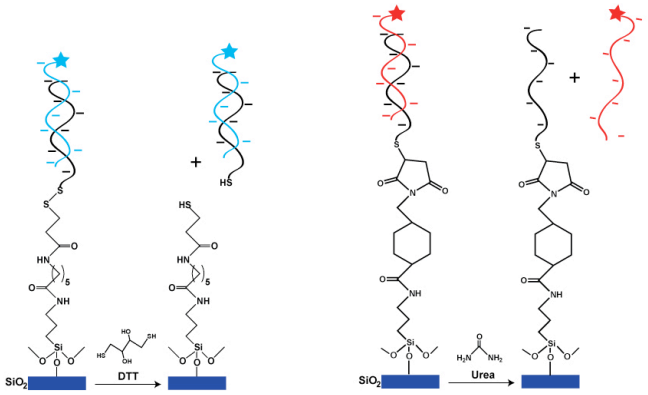


**Figure 5-1** Bifunctional crosslinkers, Sulfo-LC-SPDP (A) and Sulfo-SMCC (B) were used to covalently attach APTMS with thiolated DNA. After hybridization with target DNA, (A) DTT or (B) urea was used to remove probe/target DNA or just target DNA, respectively. Not drawn to scale.

### 5.3.1 Cleavage of Linker Chemistry for Target DNA Removal on $SiO_2$

Cleavage of the linker chemistry is a direct approach to remove biomolecules from the surface. Target and probe DNA was first attached to $SiO_2$-coated Au NWs using APTMS and a cleavable linker, sulfo-LC-SPDP. Removal was accomplished by cleaving the disulfide bond in the linker chemistry with DTT via thiol-disulfide interchange as described by Equation 5-3.[9]

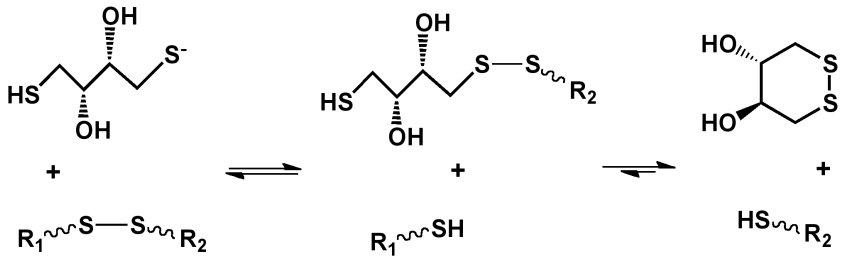

Equation 5-3

The images of fluorescently labeled target DNA hybridization with probe DNA before and after disulfide cleavage with DTT are shown in Figure 5-2. The graph (Figure 5-2, D) shows observed fluorescence was reduced by 98%, after reaction with DTT, which indicates the majority of target and probe DNA was removed from the surface. This chemistry was essentially non-reversible, as the cleaved portion was diluted and washed away. However, since a terminal thiol remains covalently attached to the surface, a subsequent crosslinking reaction could be performed in order to reuse the device, and this would enable the same or different probe molecules to be attached. A high cost due to crosslinking reagents and probe molecules may limit the benefits of this approach; therefore, a method to remove bound target while leaving the probe chemistry attached for later use was examined.

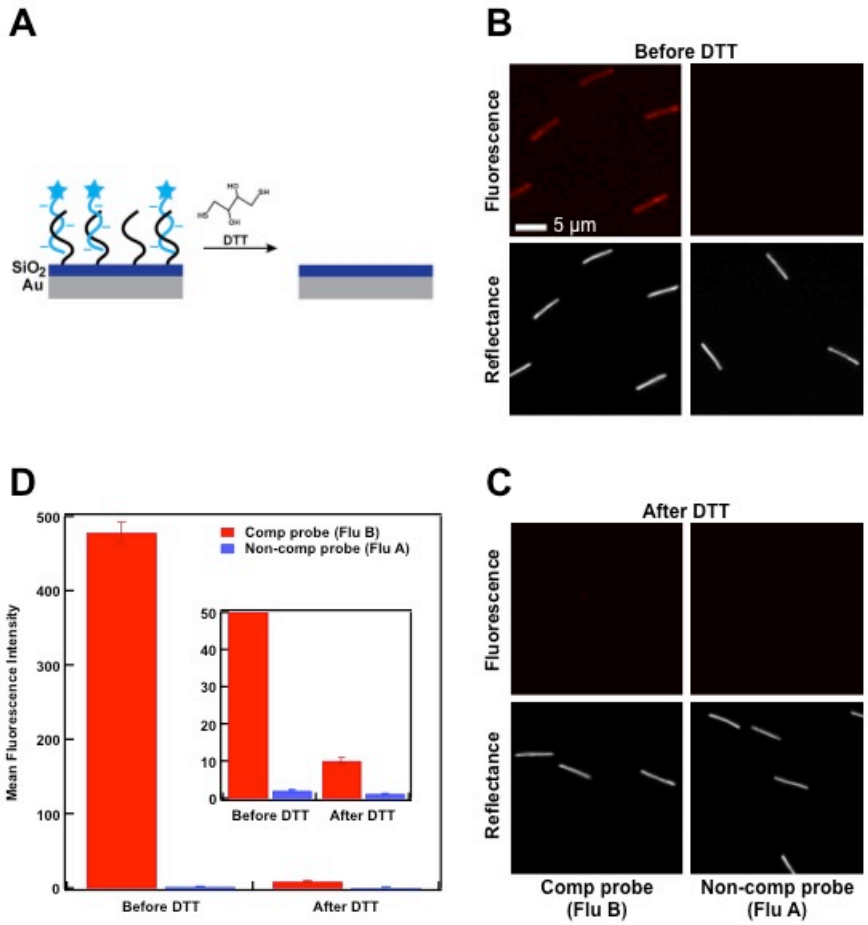


**Figure 5-2** (A) Cartoon of surface chemistry before and after cleavage of probe and target DNA with DTT. Fluorescence and reflectance microscope images of DNA-functionalized Au nanowires (B) before and (C) after reaction with DTT. (D) The graph demonstrates DNA hybridization with high specificity for the complementary probe. After cleavage of linker, (D, inset), no fluorescence is observed for either sample.

### 5.3.2 Reversible Hybridization of Target DNA with DNA or PNA-Functionalized $SiO_2$

One advantage of removing hybridized target DNA without cleaving the linker is the ability to reuse devices without additional crosslinker/probe chemistries. There are several methods to disrupt DNA-DNA or DNA-PNA hybridization, including changes in temperature[12,21], ionic strength[11,22], or the addition of a small-molecule reducing agent[23].

Urea has been used to dehybridize duplexes of DNA-DNA[8,24] or PNA-DNA[25,26] due to its ability to disrupt hydrogen bonding; however, in the case of PNA-DNA duplexes, acid was added (solution pH <3). Based on the strong affinity between DNA and PNA[8], it was unclear if complete target removal could be achieved with urea alone.

$SiO_2$-coated NWs were functionalized with APTMS, Sulfo-SMCC, DNA probe, and subsequently incubated with fluorescent DNA target. An aliquot of wires was removed for images collected before treatment with urea. Aliquots were removed again after incubation in urea and rehybridization of target, respectively. A schematic of this process is shown in Figure 5-3, A. Quantification of fluorescence images of NWs before urea and after urea show effective removal of target DNA in room temperature reducing conditions after 1 hour (Figure 5-3). Of equal importance, target was successfully rehybridized to the NWs (Figure 5-3, D) and comparison of the mean fluorescence intensity before and after urea treatment indicates hybridization efficiency was not compromised during the process (Figure 5-3, E).

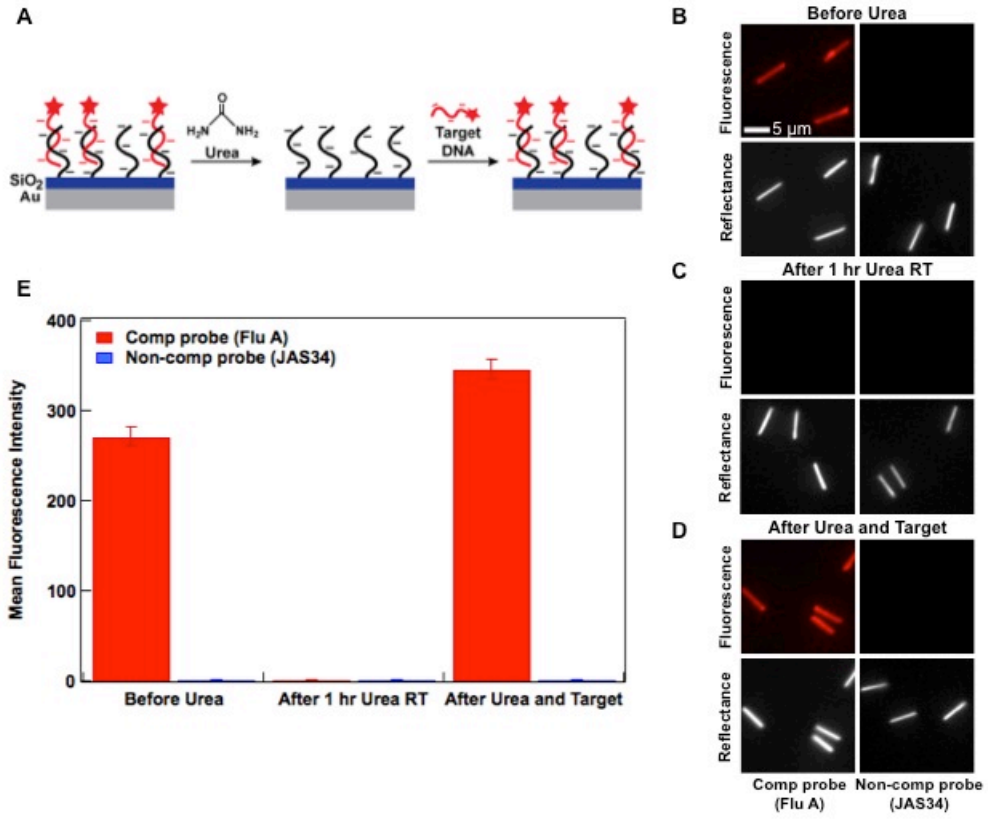


**Figure 5-3** (A) Reaction of urea with DNA-functionalized Au nanowires removes hybridized target DNA. Fluorescence and reflectance microscope images of DNA-functionalized Au nanowires (B) before urea, (C) after reaction in urea for 60 minutes, and (D) after rehybridization in target DNA. (E) The graph demonstrates detection of DNA with high specificity for the complementary probe. After reaction in urea for 60 minutes, no fluorescence was observed for either sample, indicating DNA target was efficiently removed from the surface. Fluorescence after urea demonstrates the probe DNA remains intact and specific.

Similarly, PNA-functionalized NWs were examined (Figure 5-4). Incubation of NWs with urea for 1 hour at room temperature resulted in only ~50% target removal, roughly 2-fold decrease in fluorescence (Figure 5-4; B, C). The following day, a different batch of NWs were functionalized with PNA and incubated in urea for 2 hours at 45°C (Figure 5-4; D, E) which resulted in 93% reduction in fluorescence.

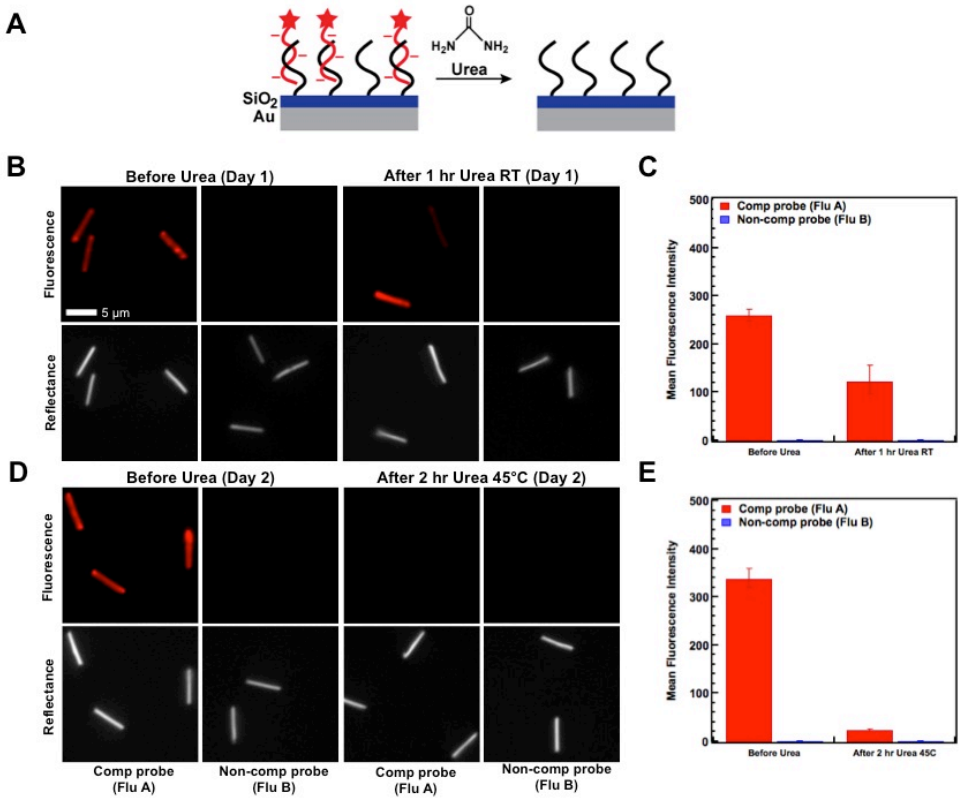


**Figure 5-4** (A) Reaction of urea with PNA-functionalized Au nanowires removes hybridized target DNA. Fluorescence and reflectance microscope images of PNA-functionalized Au nanowires before and after (B) 1 hour reaction in urea at room temperature and (D) 2 hour reaction in urea at 45°C. The graphs (C, E) both show a decrease in complementary target fluorescence after incubation in urea, but to a greater extent when temperature and time were increased.

Comparison of duplex stability at room temperature in the presence of urea indicates the PNA-DNA duplexes were more resistant to hydrogen bond disruption based on ~50% duplex retention compared to almost 0% with DNA-DNA duplexes. Elevated temperature was eventually necessary for complete duplex collapse. At this point, it is unclear what role urea played in the destabilization of PNA-DNA duplexes due to approach of the calculated[21,27] duplex $T_m$ near 45°C; however, the result still has significant implications for surface regeneration of biosensors.

## 5.4 Conclusions

These experiments demonstrate two strategies to remove DNA target after hybridization with DNA or PNA probe functionalized surfaces. The first method involved cleavage of linker chemistry, which released both probe and target from the surface. For charge-based sensors, such as field-effect transistors (FETs), this method is useful in device characterization, as the surface should return to a baseline achieved prior to probe functionalization. The second approach demonstrated a method to remove hybridized target DNA under mild reducing conditions, which enabled target to be rehybridized without further surface functionalization necessary. This chemistry could be particularly beneficial in the development stages of biosensors to offset high fabrication costs or low device yields and enable additional information about device properties, longevity, or storage capacity to be obtained. The author would like to acknowledge Dr. Philip Bevilacqua for helpful discussions about the use of urea to gently remove bound target strands.

## 5.5 References

1. Daniels, J. S.; Pourmand, N. Label-Free Impedance Biosensors: Opportunities and Challenges. *Electroanalysis* **2007**, *19*, 1239-1257.
2. Chen, S.; Bomer, J. G.; Carlen, E. T.; Berg, A. V. D. Al2O3/Silicon NanoISFET with Near Ideal Nernstian Response. *Nano Lett.* **2011**, *11*, 2334-2341.
3. Bhalla, V.; Carrara, S.; Stagni, C.; Samorì, B. Chip Cleaning and Regeneration for Clectrochemical Sensor Arrays. *Thin Solid Films* **2010**, *518*, 3360-3366.

4. *Handbook of Bioseparations*; Ahuja, S., Ed.; Academic Press: San Diego, 2000; Vol 2.

5. Gutfreund, H.; *Kinetics for the Life Sciences: Receptors, Transmitters, and Catalysts;* Cambridge University Press: London, 1995.

6. Andersson, K.; Areskoug, D.; Hardenborg, E. Exploring Buffer Space for Molecular Interactions. *J. Mol. Recognit.* **1999***, 12*, 310-315.

7. Andersson, K.; Hämäläinen, M.; Malmqvist, M. Identification and Optimization of Regeneration Conditions for Affinity-Based Biosensor Assays. A Multivariate Cocktail Approach. *Anal. Chem.* **1999**, *71*, 2475-2481.

8. Herskovits, T. T. Nonaqueous solutions of DNA; Denaturation by Urea and its Methyl-Derivatives. *Biochemistry* **1963**, *2*, 335-340.

9. Singh, R.; Whitesides, G. M.; Reagents for Rapid Reduction of Disulfide Bonds in Proteins. In *Techniques in Protein Chemistry*, Crab, J. W., Ed.; Academic Press: New York, 1995; Vol. 6, 259-266.

10. Waugh, D. S. Making the Most of Affinity Tags. *Trends in Biochemistry* **2005**, *23*, 316-320.

11. Tomac, S.; Sarkar, M.; Ratilainen, T.; Wittung, P.; Nielsen, P. E.; Nordén, B.; Gräslund, S. Ionic Effects on the Stability and Conformation of Peptide Nucleic Acid Complexes. *J. Amer. Chem. Soc.* **1996**, *118*, 5544-5552.

12. Uhlmann, E.; Peyman, A.; Breipohl, G.; Will, D. W. PNA: Synthetic Polyamide Nucleic Acids with Unusual Binding Properties. *Angew. Chem. Int. Ed.* **1998**, *37*, 2796-2823.

13. Nicewarner-Pena, S. R.; Freeman, R. G.; Reiss, B. D.; He, L.; Pena, D. J.; Walton, I. D.; Cromer, R.; Keating, C. D.; Natan, M. J. Submicrometer Metallic Barcodes. *Science* **2001**, *294*, 137-141.

14. Al-Mawlawi, D.; Liu, C. Z.; Moskovits, M. Nanowires Formed from Anodic Oxide Nanotemplates. *J. Mater. Res.* **1994**, *9*, 1014-1018.

15. Martin, C. R. Nanomaterials: A Membrane-Based Synthetic Approach. *Science* **1994**, *266*, 1961-1966.

16. Martin, B. R.; Dermody, D. J.; Reiss, B. D.; Fang, M.; Lyon, L. A.; Natan, M. J.; Mallouk, T. E. Orthogonal Self-Assembly on Colloidal Gold-Platinum Nanorods. *Adv. Mater.* **1999**, *11*, 1021-1025.

17. Kirby, D. J.; Smith, B. D.; Keating, C. D.; Microwell Directed Self-Assembly of Vertical Nanowire Arrays. *Part. Part. Syst. Charact.* **2013**, DOI: 10.1002/ppsc. 201300260.

18. Yin, Y.; Lu, Y.; Sun, Y.; Xia, Y. Silver Nanowires can be Directly Coated with Amorphous Silica to Generate Well-Controlled Coaxial Nanocables of Silver/Silica. *Nano Lett.* **2002**, *2*, 427-430.

19. Sioss, J. A.; Keating, C. D. Batch Preparation of Linear Au and Ag Nanoparticle Chains Via Wet Chemistry. *Nano Lett.* **2005**, *5*, 1779-1783.

20. Sioss, J. A.; Stoermer, R. L.; Sha, M. Y.; Keating, C. D. Silica-Coated, Au/Ag Striped Nanowires for Bioanalysis. *Langmuir* **2007**, *23*, 11334-11341.

21. Giesen, U.; Kleider, W.; Berding, C.; Geiger, A.; Ørum, H.; Nielsen, P. E. A Formula for Thermal Stability ($T_m$) Prediction of PNA/DNA Duplexes. *Nucleic Acids Res.* **1998**, *26*, 5004-5006.

22. Park, H.; Germini, A.; Sforza, S.; Corradini, R.; Marchelli, R.; Knoll, W. Effect of Ionic Strength on PNA-DNA Hybridization on Surfaces and in Solution, *Biointerfaces*, **2007**, *2*, 80-88.

23. Nordstrom, L. J.; Clark, C. A.; Andersen, B.; Champlin, S. M.; Schwinefus, J. J. Effect of Ethylene Glycol, Urea, and N-Methylated Glycines on DNA Thermal Stability: The Role of DNA Base Pair Composition and Hydration. *Biochemistry* **2006**, *45*, 9604-9614.

24. Yu, F.; Persson, B.; Löfås, S.; Knoll, W. Surface Plasmon Fluorescence Spectroscopy for Protein Binding Studies. In *Protein Microarray Technology*; Kambhampati, D., Ed.; Wiley-VCH: Germany, 2004.

25. Kröger, K.; Jung, A.; Reder, S.; Gauglitz, G. Versatile Biosensor Surface Based on Peptide Nucleic Acid with Label Free and Total Internal Reflection Fluorescence Detection for Quantification of Endocrine Disruptors, *Anal. Chim. Acta* **2002**, *469*, 37-48.

26. Dodd, D. W.; Hudson, R. H. E. Analysis and Purification of Peptide Nucleic Acids by Denaturing PAGE. *Electrophoresis* **2007**, *28*, 3884-3889.

27. Zuker, M. Mfold Web Server for Nucleic Acid Folding and Hybridization Prediction. *Nucleic Acids Res.* **2003**, *31*, 3406-3415.

# Appendix

## Synthesis and Investigation of Silver Nanoparticles: An Undergraduate General Chemistry Laboratory Experiment

**Abstract**

This laboratory experiment was developed as a make-up lab for use in general chemistry. Now it is used as a standard experiment in the second semester general chemistry laboratory that has a materials emphasis. It was designed as a more cost-effective alternative to a similar experiment, Gold Nanoparticle-Synthesis and Layering, developed by Dr. Sarah Brunker. In this experiment, students gain experience with nanotechnology by synthesizing ~12 nm nanoparticles and learn about the properties of nanoparticles compared to bulk samples. Furthermore, they are introduced to charge screening and use of surfactants to prevent particle aggregation.

Included in this section, are all the materials used for this experiment:

- List of Required Chemicals and Laboratory Equipment
- Laboratory Procedure-including background information, practice quiz, and experimental procedure
- Pre-Lab Quiz
- Laboratory Grade Sheet
- Laboratory Answer Key
- Pre-Lab Quiz Key

**List of Required Chemicals and Laboratory Equipment**

Materials needed for 6 students (3 groups of 2)

Chemicals:
150 mL  0.001M silver nitrate
20 mL 0.0388 M sodium citrate
Tween-20
DI water
Sodium chloride (couple grams)
Sucrose (several grams)

Lab Equipment (clean glassware and stir bar is imperative):

| | |
|---|---|
| 3 | 10 mL graduated cylinder |
| 3 | 25 mL graduated cylinder |
| 3 | 50 mL Erlenmeyer flask |
| 3 | stir bars |
| 3 | hot plate/stirrers |
| 15 | standard disposable plastic pipettes |
| 3 | 9 in or “extra long” disposable plastic pipettes |
| 3 | Spec-20 UV-Vis instruments |
| 6 | disposable cuvettes |
| 9 | 20 mL glass vials |
| 9 | 8 mL glass vials |
| 3 | permanent markers |

**Laboratory Manual**

Synthesis and Investigation of Silver Nanoparticles

Kristi L. Liddell

Background:

Silver metal has been used over the years for a variety of applications. It is most commonly known for its antimicrobial properties. Ancient Greeks in 1000 B.C. took advantage of this to keep the water supply safe. Silver vessels were commonly used for drinking water and other liquids. During the 19th century, silver salts were used for therapeutic treatment of skin lesions, burns, and ulcers. In recent years, silver nanoparticles have been of interest for their potential in biological and pharmaceutical applications[1].

Nanotechnology has become a prominent field in chemistry and material science. It involves the study of matter at the atomic or molecular level, which is on a scale of 1 to 100 nm. Metal nanoparticles exhibit unique properties compared to the bulk material. At room temperature, the mean free path of an electron in a metal is around 1 to 100 nm. The mean free path of an electron describes how far it can travel before it bumps into another atom or molecule and "scatters". Therefore, when a particle is equal or less than the size of the mean free path its electron, interesting effects can result[2].

A colloid or colloidal dispersion is a mixture containing very small particles that remain suspended in a dispersing medium[2]. Silver colloid can by synthesized in an aqueous solution of silver nitrate in the presence of sodium citrate (Equation 1).

Equation 1:

$$4AgNO_{3\ (aq)} + Na_3C_6H_5O_{7\ (aq)} + 2H_2O_{(l)} \rightarrow 4Ag^{0}{}_{(s)} + H_3C_6H_5O_{7\ (aq)} + 3NaNO_{3(aq)} + HNO_{3(aq)} + O_{2\ (g)}$$

Nanoparticles are formed when elemental silver atoms begin to "stick" to other silver atoms. Nanoparticle size is initially controlled by excess sodium citrate that adsorbs to the surface of the nanoparticles to impart a net negative charge (Figure 1)[3]. This helps stabilize the particles and prevent aggregation. Aggregation occurs when a nanoparticle reaches a critical mass that is too large to remain suspended in solution. When this occurs, it is said to have "crashed" out of solution. Aggregation can also be initiated by adding charged particles to the solution (dissolved salt, for example). These charges "screen" the particles from one another; their negative charges no longer repel each other, and they begin to clump together and fall out of solution.

Colloidal solutions scatter light, but also absorb certain wavelengths that depend on the size of the nanoparticle. The observed solution color is due to a phenomenon called plasmon absorbance. Plasmon absorbance occurs when incident light creates oscillations in conduction electrons on the surface of the nanoparticle and electromagnetic radiation is absorbed. The absorbance is unique for each metal and varies depending on the size, shape, and solution temperature. The synthetic procedure described typically yields 12 ± 2 nm silver nanoparticles, which produces a maximum wavelength peak around 400 nm (Figure 2)[3].

A Spec-20 spectrophotometer measures the amount of light absorbed by the sample by comparing the intensity of the light emitted from the light source, $I_0$, with the intensity of the light that emerges from the sample, I. The ratio of $I/I_0$ is known as the solution

transmittance. The percent transmittance is this ratio multiplied by 100. The solution absorbance is related to transmittance by the equations given below (Equation 2). Using

Equation 2:

$T = I/I_0$; $\%T = I/I_0 \times 100\%$; $A = -\log T$

this information, the approximate size of the nanoparticles can be determined by comparing the maximum wavelength obtained to known values of silver colloid with specified dimensions.

A flocculation assay will also be performed on these nanoparticles, which means that a substance will be added to purposefully aggregate the colloid. When the colloid is forced to aggregate, the distance between nanoparticles is reduced, the diameter of the particles increases, and the wavelength absorbed shifts. The aggregation is indicated by a change in solution color, which can be observed with your eyes[4]. Figure 3 demonstrates the various levels of aggregation in silver nanoparticles[3]. With 12 nm diameter, the colloid has a light yellow color but as the particles increase in size, the color of the solution shifts until the nanoparticles crash out of solution and large metallic grey clumps appear. Aggregation depends on the substance added to the colloidal solution, as well as how much of it is added. Two substances will be added to the colloid solution, which may or may not aggregate the nanoparticles; they are sodium chloride and sucrose.

It is possible to protect the nanoparticles from aggregating by coating them in compounds such as enzymes, proteins, or small molecules. In this experiment you will be coating your nanoparticles with a layer of surfactant, or a molecule with a hydrophillic

head group and a hydrophobic tail, which decreases surface tension. Surfactant molecule (a.k.a. detergent molecules) can group together to form layers (known as monolayers) or spheres, which are known as micelles. When a nanoparticle is exposed to a surfactant solution, Van der Waals forces physisorb (a type of adsorption –or sticking to the surface) the surfactant to the particle surface (Figure 4). When a nanoparticle is coated with a surfactant, steric or (physical) interactions prevent the silver nanoparticles from touching each other, therefore protecting them from aggregating with one another. This is a physical interaction; there is no charge interaction between the surfactant molecules (Tween 20). Even when ions are introduced to the system, and the nanoparticles are screened from one another, they will not aggregate because the surfactant molecules are in between them, preventing them from touching each other and crashing out of solution[4].

Included in the supplemental figures is a TEM, or transmission electron microscope, image which (instead of shinning light on the sample) "shines" electrons, allowing for much better resolution of the sample (Figure 5)[3]. The image allows one to see the silver nanoparticles obtained from this experiment are spherical and similar in size.

References:

1. Bhattacharya, R.; Mukherjee, P. "Biological properties of "naked" metal nanoparticles" *Adv. Drug Delivery Rev.* **2008**, *60,* p1289-1306.
2. Brown, T.; Lemay, H.; Bursten, B.; Murphy, C. *Chemistry: The Central Science*, 10th Ed, **2005**, Prentice Hall: New Jersey.
3. Solomon, S.; Bahadory, M.; Jeyarajasingam, A.; Rutkowshy, S.; Boritz, C. "Synthesis and study of silver nanoparticles" *J. Chem. Ed.* **2007**, *84,* p 322-325.
4. Brunker, S. "Gold nanoparticles: Synthesis and Multilayering" *Chem 113M Student Manual*, **2008,** Hayden-McNeil: New York. pg GN-1-GN-11

Quiz Outline:

What applications has silver been used for in the past?

What is nanotechnology?

Explain why nanoparticles have unique properties compared to the bulk material.

What is a colloidal solution?

What is aggregation? What causes it?

Draw a picture and describe how aggregation can be prevented.

How many grams of NaCl is needed to make a 20mL solution of 0.25 M NaCl? (Na=22.99 g/mol), Cl= 35.45 g/mol)

What can cause a solution of silver nanoparticles to change color?

How does a Spec-20 work?

How is the solution absorbance calculated from a %T measurement?

What is a physical change? What is a chemical change?

Sample Quiz:

1. How many grams of sucrose ($C_{12}H_{22}O_{11}$, or table sugar) would you need to make up 10 mL of 2.0 M sucrose solution? (C=12.01 g/mol, H= 1.008 g/mol, O= 16.00 g/mol)

2. What is a flocculation assay?

3. Define "crashing" out of solution.

4. Draw a picture and describe what compound would be good at protecting silver colloid from aggregation.

5. Name 2 uses for silver.

Supplemental Figures:

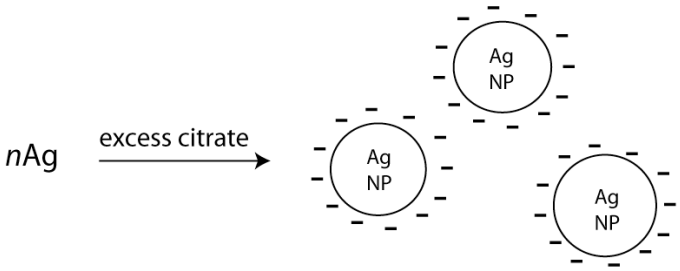


Figure 1: Silver nanoparticles (Ag NP) remain separated due to the repulsive forces created by the negative charge on citrate.

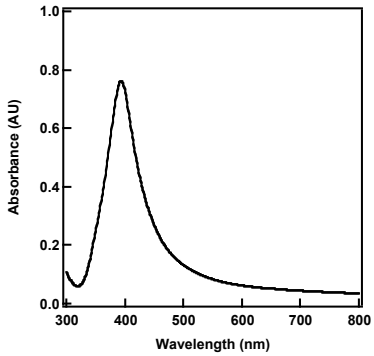


Figure 2: UV-Vis spectra of clear yellow solution of silver colloid.

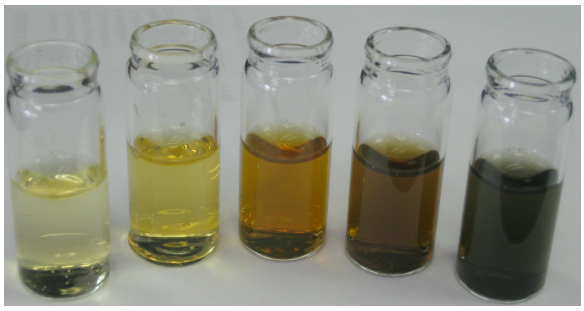

Figure 3: Silver colloid often has a pale yellow color. However, the solution color changes to an orange, brown, and grey color with increased particle aggregation.

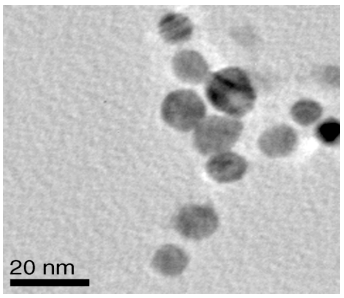


Figure 5[3]: TEM image of silver nanoparticles.

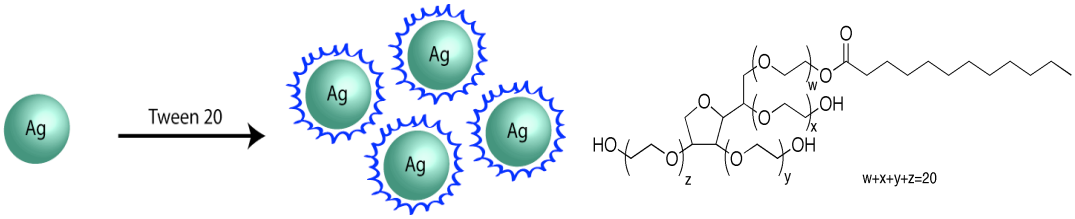


Figure 4: Left: Silver nanoparticles coated in surfactant (Tween 20) do not aggregate due to steric interference. Right: Structure of Tween 20 has a hydrophilic head group and hydrophobic tail group.

Laboratory Experiments

Flowchart of the Experiment

Section A: Synthesis of silver colloid

Section B: Determination of colloid size by UV-Vis spectrophotometry

Section C: Flocculation assay of silver colloid

Requires one four-hour class period to complete.

## Section A: Synthesis of silver colloid

***Goal:***

To synthesize silver nanoparticles.

***Experimental Steps:***

1. Obtain a 10mL graduated cylinder, 25mL graduated cylinder, 50 mL Erlenmeyer flask, and stir bar.

2. Pour 25 mL 0.001 M silver nitrate ($AgNO_3$) into the Erlenmeyer flask.

3. Add a stir bar and heat the solution with mild stirring to a gentle boil.

4. Measure 2 mL 0.0388 M sodium citrate ($Na_3C_6H_5O_7$ ) in a clean 10mL graduated cylinder.

5. Once a gentle boil is observed, add the sodium citrate.

6. Continue heating and stirring the solution until a pale yellow color is observed (~1-3 minutes).

7. **Important!** Turn off the stir plate and remove the flask from the heat as soon as a yellow color is observed. If your solution appears orange, brown, or gray ask your TA for further instructions.

***Questions:***

Q1. Name two uses for silver.

Q2. What is a colloidal solution?

Q3a. Describe the color change observed as sodium citrate was added to the silver nitrate.
b. Give a chemical explanation for why the solution changes color.

Q4. Did you just observe a chemical or physical change? Explain.

Q5a. Given the balanced equation for the reaction of silver nitrate with sodium citrate, write out the full ionic and net ionic equation.
b. What species is being oxidized? What is being reduced? Write out the each half reaction.
c. What reactant is in excess?

Q6. If the solution is stirred for long periods of time after the addition of sodium citrate the solution color changes from light yellow, dark yellow, orange, purple, and finally to grey. Explain what is happening on a molecular level and why.

## Section B: Determination of colloid size by UV-Vis spectrophotometry

***Goal:***

To determine the approximate diameter of silver colloid synthesized using a UV-Vis spectrophotometer.

***Experimental Steps:***

1. Obtain 2 disposable cuvettes from the front of the room. Fill 1 cuvette ¾ full with distilled water and the other ¾ full with your colloid solution.

2. Measure and record the % transmittance of the solution every 20 nm between 350 nm – 390 nm, every 5 nm between 390 nm – 410 nm, and every 30 nm between 410 nm – 590 nm.

***Questions:***

Q7a. Calculate absorbance from % transmittance. Make a table of the wavelength, %Transmittance, and absorbance. Show your work.

b. Make a graph of absorbance versus wavelength. Draw a smooth line through the points.

c. Where is your maximum peak absorbance? Compare the size of your nanoparticles to what was expected.

Q8. Name and describe another technique that can be used to determine the size of nanoparticles.

## Section C: Flocculation assay of silver colloid

***Goals:***

To understand the causes of nanoparticle aggregation and learn how surfactant molecules can prevent it from occurring.

***Experimental Steps:***

1. Prepare 10 mL solution of 1.0 M sodium chloride (NaCl) in a clean, 20 mL vial.

2. Prepare 10 mL solution of 1.0 M sucrose ($C_{12}H_{22}O_{11}$) in another, clean, 20 mL vial.

***Questions:***

Q9. In Steps 1 and 2, you have to prepare your own salt and sugar solutions. Describe the steps required to make these solutions. Make sure to include the mass or volume of reagents used and how they were measured. Show your work for the calculations of required sodium chloride and sucrose.

***Experimental Steps:***

3. Add 5 mL of colloid to two, 8 mL vials.

4. With a pipette, add 5-10 drops of the NaCl solution into the first vial of colloid. Be sure to observe the effects from above as well as from the side.
   Note: A white paper placed under the vial allows color changes to be easily visualized.

5. With a pipette, add 5-10 drops of the sucrose solution into the second vial of colloid.

6. Label the vials so you can remember what you added to each solution.

***Questions:***

Q10a. Record your observations of both solutions.
b. For each vial, did you observe a chemical change or a physical change? Explain.
c. Draw a picture for each vial of what you think is going on at the atomic level after adding salt or sucrose.

Q11a. What is keeping the particles in solution from aggregating before you add anything else to the solution?
b. Why does adding the salt solution have a different effect than adding the sugar solution?

***Experimental Steps:***

7. Dump out the 1.0 M sucrose solution you made and thoroughly wash the vial with distilled water. Keep both colloid solutions and the salt solution.

8. Add 5 mL of colloid solution, and 3 drops of the surfactant Tween-20 in the vial you just cleaned. Do not use a pipet for the Tween-20, add the drops directly into the dilute colloid.

9. Shake the solution gently and let it sit for 15 minutes.

***Questions:***

Q12. What is a surfactant? Give a general description of it molecular properties.

Q13. What is the purpose of adding Tween-20 to your silver colloid?

***Experimental Steps:***

10. Draw up some sodium chloride solution into a pipet and place the pipet into the solution *below* the level of bubbles. Dispel some of the NaCl solution into the colloid/Tween 20 solution.

***Questions:***

Q14a. Record your observations.
b. Compare your observations between this vial and the other two vials made previously.
c. Draw a picture, on the atomic level, of what occurred in this last experiment between colloid, Tween 20, and the salt solution.

***Experimental Steps:***

11. The 1.0 M salt solution can be dumped down the sink. The remaining colloidal solutions can be disposed of up front. **Do not forget to remove the stir bar!** The stir bar and cleaned glassware can be replaced up at the front of the room.

**Pre-Lab Quiz**

Name:
TA:
Section:

1. How many grams of potassium chloride would you need to make a 10 mL solution of 1.0 M KCl? (K= 39.10 g/mol, Cl=35.45 g/mol). Show your work!

2. How does a Spec-20 determine the absorbance of a solution?

3. What is a colloidal solution?

4. What is the purpose of a surfactant in this experiment?

5. What size scale is the term “nano” used for?

**Laboratory Grade Sheet**

Name:
TA:
Section:

| | Question | Points | |
|---|---|---|---|
| Section A | Q1 | 2 | |
| | Q2 | 3 | |
| | Q3 | 3 | |
| | Q4 | 4 | |
| | Q5a | 4 | |
| | Q5b | 2 | |
| | Q5c | 2 | |
| | Q6 | 3 | |
| Section B | Q7a | 4 | |
| | Q7b | 6 | |
| | Q7c | 3 | |
| | Q8 | 4 | |
| Section C | Q9 | 8 | |
| | Q10a | 4 | |
| | Q10b | 6 | |
| | Q10c | 6 | |
| | Q11a | 3 | |
| | Q11b | 3 | |
| | Q12 | 3 | |
| | Q13 | 3 | |
| | Q14a | 2 | |
| | Q14b | 3 | |
| | Q14c | 4 | |
| Notebook Pages | | 15 | |

-Date/Exp title on each page
-Goal
-Ref procedure
-Section headings
-Ans labeled
-Partner names
-Lab written in pen

-No white out/easers
-No blank pages/spaces
-TA signature
-Time management
-Illegible/sloppy
-Poor grammar/spelling
-Safety

TOTAL 100 _____

**Laboratory Answer Key**

Q1. (2 pts)
There are a variety of uses for silver nanoparticles. Answers will vary.

Q2. (3pts)
A colloid or colloidal dispersion is a mixture containing very small particles that remain suspended in a dispersing medium.

Q3. (3pts)
Colorless to yellow to dark yellow (and maybe to gray)

Q4. (4pts)
Chemical change is occurring because chemical reaction is occurring between silver nitrate and sodium borohydride to produce silver (solid) and hydrogen gas.
May describe as physical change (in addition to chemical) due to size of nanoparticles increasing.

Q5a (4pts)

$2AgNO_3$ (aq) + $2NaBH_4^-$ (aq) → 2Ag (s) + $H_2$ (g) + $B_2H_6$ (aq) (2 pts)

$2\ Ag^+$ (aq) + 2e- → 2 Ag (s) (1 pt)
$H_2$ (g) + 2e- → $2H^-$ (aq) (1 pt)

Q5b (2 pts)

$Ag^+$ is getting reduced
$H^-$ is getting oxidized.

Q5c (2 pts)

$NaBH_4$ is in excess

Q6 (3 pts)
Stirring causes collisions with nanoparticles. These collisions can cause particles to aggregate more. The color of the solution changes based on the size of the nanoparticle until finally they become too large to remain in solution and fall out (turn gray in color).
-be flexible with response

Q7a. (4 pts)
-Show 2 calculations: from %T to T and T to Abs (2 pts)
-Values in table from ~350 to 550nm (2 pts)

Q7b. (6 pts)
-axis labeled (2 pts)
-points plotted (1 pt)
-title (1 pt)
-smooth line through points (1 pt)
-graph at least ½ page / graph scale makes sense and correct (1 pt)

Q7c (3 pt)
-max wavelength ~ 410nm
-compare to 12nm colloid ~400nm

Q8 (4 pts)
A transmission electron microscope, "shines" electrons on the sample, allowing for much better resolution.

Q9 (8 pts)
Calculation for NaCl (3 pts)

1.0M NaCl * 0.010L* 58 $gmol^{-1}$ = 0.58g

Calculation for Glucose (3 pts)

1.0M Glucose * 0.010L * MW sugar = x g
Describe process of adding solid to 10mL water and stir (1 pt each)

Q10a (4 pts)
Salt solution turns gray (2 pt)
Glucose solution remains the same (2 pt)

Q10b (6 pts)
Salt soln is a physical change bc particles are getting larger in size (4 pt)

Glucose soln is not changing (2 pt)

Q10c (6 pts)
For NaCl picture… (3 pts)

For Glucose picture… (3 pts)

Q11a (3 pts)
Adsorbed $BH4^-$ ions are repulsive to one another and keep the particles separate

Q11b (3 pts)
The salt shields the electrostatic repulsion between the particles, allowing them to aggregate.

Q12 (3 pts)

It is possible to protect the nanoparticles from aggregating by coating them in compounds such as enzymes, proteins, or small molecules. In this experiment you will be coating your nanoparticles with a layer of surfactant, or a molecule with a hydrophillic head group and a hydrophobic tail, which decreases surface tension. Surfactant molecule (a.k.a. detergent molecules) can group together to form layers (known as monolayers) or spheres, which are known as micelles.

Q13 (3 pts)

Tween protects nanoparticles from aggregating

Q14a (2 pts)

When salt is added, nothing happens.

Q14b (3 pts)

Before, the salt solution crashed and glucose didn't.

Q14c (4 pts)

Draw a picture of Tween 20 protecting NPs from aggregating.

**Pre-Lab Quiz Answer Key**

1. How many grams of potassium chloride would you need to make a 10 mL solution of 1.0 M KCl? (K= 39.10 g/mol, Cl=35.45 g/mol). Show your work!

**M = mol/liter mol = g/mw**

**mw 1pt. work 1pt. answer 1 pt.**

2. How does a Spec-20 determine the absorbance of a solution?

**Measure intensity before and after 1 pt.**

**Abs = -log T 1pt.**

3. What is a colloidal solution?

**Particles suspended in medium**
**(1pt) (1pt)**

4. What is the purpose of a surfactant in this experiment?

**Prevent aggregation 2 pt.**

5. What size scale is the term "nano" used for?

**$10^{-9}$ 1-100 nm 1 pt.**

# VITA

## Kristi L. Liddell

**Education**

| | |
|---|---|
| Ph.D. Chemistry: Pennsylvania State University, University Park, PA | 2014 |
| B.S. Chemistry: St. John Fisher College, Rochester, NY | 2008 |

**Awards**

| | |
|---|---|
| Dow Travel Award | 2011 |
| Dan H. Waugh Memorial Teaching Award | 2010 |
| Roberts Fellowship | 2008 |

**Publications**

1. Wang, B.*; **Liddell, K. L.***; Wang, J.; Kroger, B.; Keating, C. D.; Zhu, J. Novel oxide-on-graphene biosensors. *Submitted to Nano Research*.
   *These authors contributed equally in this work
2. **Liddell, K. L.** Experiment 18: Synthesis and Investigation of Silver Nanoparticles. In *PSU Chemistry 113M Laboratory Manual*, Shoemaker, M. C., Keiser, J. T. Eds.; Hayden-McNeil: Englewood Cliffs, NJ, 2013; pp 18-1 - 18-12.

**Selected Presentations**

1. Zhong, X.; **Liddell, K. L.**; Boehm, S.; Mayer, T. S.; Keating, C. D. "Combining Biology with CMOS through Deterministic Nanowire Assembly" Poster presentation, 2012 MSD Annual Review Meeting; Cambridge, MA.
2. **Liddell, K. L.**; Zhong, X.; Wang, B.; Zhu, J.; Mayer, T.; Keating, C. D. "Surface Functionalization of Gate Dielectrics for Biosensing Applications" Oral presentation, Pittcon 2012; Orlando, FL.
3. Zhong, X.; **Liddell, K. L.**; Won, B.; Sun, K.; Dean, S.; Mayer, T. S.; Keating, C. D. "Combining Biology with CMOS through Deterministic Nanowire Assembly" Poster presentation, 2011 MSD Annual Review Meeting; Cambridge, MA.
4. **Liddell, K. L.**; Zhong, X.; Sun, K.; Dean, S. L.; Mayer, T. S.; Keating, C. D. "Fabrication and Characterization of Phosphonic Acid Monolayers for Use in Biosensing." Poster presentation, 241st ACS National Meeting Spring 2011; Anaheim, CA.